

Intrinsic and Extrinsic Reduction of SnX Tin
Chalcogenide (X=S, Se) Lattice Thermal Conductivity
Through Heterostructure Layering

by

Jordan Rundle

A Thesis Submitted in Partial Fulfilment of the Requirements for the
Degree of Doctor of Philosophy (PhD)

Cardiff University, School of Chemistry

January 2022



Contents

Contents.....	i
Abstract.....	v
Acknowledgements.....	vi
1 – Thermoelectric Materials.....	1
1.1 - Use of Thermoelectric Devices.....	1
1.2 - The Thermoelectric Effect.....	2
The Seebeck Effect.....	2
The Peltier Effect.....	2
The Thomson Effect.....	3
1.3 - Related Effects.....	3
The Hall Effect.....	3
The Nernst-Ettinghausen Effects.....	3
The Righi-Leduc Effect.....	4
1.4 - Thermoelectric Devices.....	4
The Thermoelectric Figure of Merit.....	5
1.5 - Thermoelectrics vs. Pyroelectrics vs. Piezoelectrics.....	7
1.6 - Thermoelectric Cooling vs. Mechanical Refrigeration.....	7
1.7 - Problems with Thermoelectrics.....	8
Electrical Conductivity vs. Thermal Conductivity.....	8
Weight vs. Efficiency (Moving Systems).....	8
Large, Constant Temperature Gradient Needed.....	9
1.8 - Electronic Effect Improvement.....	9
Charge Carrier Density.....	9
Charge Carrier Effective Mass.....	9
The Rashba Effect.....	10
Resonant Levels.....	10
Critical Phenomena-Induced Effects.....	10
1.9 - Phonon Disruption.....	11
Complex Unit Cell.....	12
Disordered Cell.....	12
Mass Effect.....	12
Boundary Design.....	12
1.10 - Established Materials.....	13
Chalcogenides.....	14
Half-Heusler Alloys.....	15
Skutterudites.....	15
Organic Semiconductors.....	15
References.....	16
2 – Computational Methods.....	19
2.1 – Theoretical Background.....	19
2.1.1 - The Schrödinger Equation.....	19

<i>Hartree and Hartree-Fock</i>	21
<i>Density-Functional Theory</i>	22
<i>Local Density Approximation</i>	24
<i>Generalised Gradient Approximation</i>	25
2.1.2 - <i>Pseudopotentials and Plane-Waves</i>	25
<i>Plane Wave Basis Set</i>	25
<i>Pseudopotentials</i>	26
2.1.3 - <i>Tight-Binding Approximation</i>	27
2.1.4 - <i>Wannier Functions</i>	28
<i>Wannier90</i>	28
<i>BoltzWann</i>	30
2.1.5 - <i>Heat Transport Equations</i>	32
<i>Atomic Vibration</i>	32
<i>Phonopy and Phono3py</i>	35
2.2 - <i>Methodology</i>	40
2.2.1 – <i>Quantum Espresso</i>	40
<i>Relaxation</i>	40
2.2.2 – <i>Wannier90 and Postw90</i>	40
<i>Wannier90</i>	40
<i>Postw90</i>	41
2.2.3 – <i>CP2K</i>	41
<i>Relaxation</i>	42
2.2.4 – <i>Phono3py</i>	42
<i>Phonon Dispersion Spectra</i>	43
<i>Thermal Conductivity</i>	43
References.....	45
3 – Tin Chalcogenides	47
3.1 - <i>SnS and SnSe</i>	47
3.1.1 - <i>Electronic Properties</i>	47
<i>Characterisation</i>	47
<i>BoltzWann</i>	49
3.1.2 - <i>Phononic Properties</i>	51
<i>Characterisation</i>	51
<i>Phonon Spectral Analysis</i>	51
<i>Thermal Conductivity</i>	55
<i>Phonon Frequency</i>	56
<i>Phonon Lifetimes</i>	57
<i>Phonon Mean Free Paths</i>	58
3.1.3 - <i>Full Figure of Merit</i>	59
<i>At 300 K</i>	59
<i>Across a Temperature Range</i>	60
3.2 - <i>SnS (Cmcm)</i>	62
3.2.1 - <i>Electronic Properties</i>	62
<i>Characterisation</i>	62
3.2.2 - <i>Phononic Properties</i>	64

<i>Characterisation</i>	64
<i>Phonon Spectral Analysis</i>	65
<i>Thermal Conductivity</i>	65
<i>Phonon Lifetimes</i>	66
3.3.3 - <i>Full Figure of Merit</i>	67
<i>At 300 K</i>	67
3.3 - <i>Comparison</i>	69
3.3.1 - <i>Electronic Properties</i>	69
<i>Power Factor</i>	69
3.3.2 - <i>Phononic Properties</i>	70
<i>Lattice Thermal Conductivity</i>	70
<i>Phonon Mean Free Paths</i>	71
<i>Phonon Lifetimes</i>	71
<i>Phonon Group Velocities</i>	73
3.3.3. - <i>Figure of Merit</i>	74
<i>At 300, 500 and 750 K</i>	74
<i>Across The Temperature Range 300 K to 750 K</i>	75
3.4 - <i>Summary</i>	78
3.4.1 - <i>Lattice Thermal Conductivities</i>	78
<i>Correct Ordering of Pnma Lattice Thermal Conductivities</i>	78
<i>Understanding the Phonon Pathway Disruptors</i>	78
3.4.2 - <i>Electronic Suitability</i>	79
References.....	80
4 – Uniform Layering	82
4.1 – <i>SnS/SnSe, 2SnS/2SnSe and 3SnS/3SnSe</i>	82
4.1.1 - <i>Electronic Properties</i>	82
<i>Characterisation</i>	82
<i>BoltzWann</i>	86
<i>Power Factors</i>	88
4.1.2 - <i>Phononic Properties</i>	89
<i>Characterisation</i>	89
<i>Phonon Dispersion</i>	89
<i>Lattice Thermal Conductivity</i>	90
<i>Phonon Lifetimes</i>	94
<i>Phonon Mean Free Paths</i>	96
<i>Phonon Group Velocities</i>	98
4.1.3 - <i>Full Figure of Merit</i>	100
<i>At 300 K</i>	100
<i>At 300, 500 and 750 K</i>	101
<i>Across a Temperature Range</i>	103
4.2 - <i>Summary</i>	107
4.2.1 - <i>Lattice Thermal Conductivity</i>	107
<i>Effective Reduction of the Heat Transport</i>	107
<i>Reduction of the Phonon Lifetimes and Mean Free Paths</i>	107
<i>Softened Phonon Modes and the Reduction of Group Velocities</i>	107

4.2.2 - <i>Electronic Suitability</i>	107
4.2.3 - <i>Full Figure of Merit</i>	108
<i>Competitive Nature</i>	108
<i>Low Temperature Efficiency</i>	108
References.....	109
5 – Asymmetric Layering	110
5.1 – <i>SnS/2SnSe, 2SnS/SnSe, SnS/3SnSe and 3SnS/SnSe</i>	110
5.1.1 - <i>Electronic Properties</i>	110
<i>Characterisation</i>	110
<i>BoltzWann</i>	114
<i>Power Factor</i>	116
5.1.2 - <i>Phononic Properties</i>	117
<i>Characterisation</i>	117
<i>Phonon Dispersion</i>	118
<i>Lattice Thermal Conductivity</i>	118
<i>Phonon Lifetimes</i>	120
<i>Phonon Mean Free Paths</i>	123
<i>Group Velocities</i>	124
5.1.3 - <i>Full Figure of Merit</i>	126
<i>At 300 K</i>	126
<i>At 300, 500 and 750 K</i>	127
<i>Across a Temperature Range</i>	128
5.2 - <i>Summary</i>	133
5.2.1 - <i>Lattice Thermal Conductivity</i>	133
5.2.2 - <i>Electronic Suitability</i>	133
5.2.3 - <i>Full Figure of Merit</i>	133
Conclusion and Closing Remarks	135
Outlook.....	138
<i>Adjustment of the xTB Interatomic Potential</i>	138
<i>New Layering Schemes</i>	138
<i>Inclusion of Dichalcogenide Species</i>	138
<i>Large-Scale Mechanical Engineering</i>	138
Supplementary	139
<i>List of Publications</i>	139
<i>RTA vs. LBTE</i>	140
<i>Cutoff Pair-Distance</i>	141
<i>Supercell Sizes</i>	143
<i>Sampling Mesh</i>	144

Abstract

This work utilised Density Functional Theory and Wannier functions for the evaluation of the Boltzmann transport equations, and Tight Binding methods with the frozen phonon approach, to determine lattice thermal conductivity values of tin sulphide, tin selenide, and periodic heterostructure derivatives of these two structures. The properties were evaluated within the context of thermoelectric application, with the aim to lower lattice thermal conductivity via the creation of sandwiched SnSe/SnS tin chalcogenide periodic heterostructures.

This approach was found to give significant reduction of lattice thermal conductivity values in all structures with layering above a 1 to 1 ratio (1 SnS: 1 SnSe), reaching ultralow lattice thermal conductivities for the 3SnS/3SnSe structure of 0.14, 0.60 and 0.51 W/m/K along the a , b and c axes respectively at 300 K, a **significant reduction** from the lattice thermal conductivities of $Pnma$ -SnSe calculated at 0.34, 0.77 and 0.57 W/m/K along the a , b and c axes respectively 300 K. These lattice thermal conductivity reductions were shown to positively influence the full thermoelectric figure of merit over a range of relevant temperatures (300, 500 and 750 K), for several heterostructure motifs, with particular benefits seen in the n -doping region of the 3SnS/3SnSe, reaching a 300 K figure of merit theoretical maximum of 2.56, and in the p -doping region of the SnS/2SnSe structures, reaching a 300 K theoretical figure of merit maximum of 1.37. Both represent a **pronounced improvement** on the calculated maxima of $Pnma$ -SnSe of 1.76 and 0.98 in the p - and n -doping regions respectively. The reasons beyond these significant improvements included phonon boundary scattering effects occurring at the interfaces between the SnS and SnSe regions and phonon softening modes, which reduce the group velocity of the phonons and disrupt the heat transport further. The combination of these intrinsic (phonon softening) and extrinsic (phonon scattering) factors comes into existence as the resulting heterostructures tends to become more similar, both in lattice and electronic transport, to the $Cmcm$ high-temperature structure, which can be shown to exhibit lowered lattice thermal conductivities and greater electrical conductivity, low/large enough to compensate for a smaller Seebeck coefficient maximum.

Acknowledgements

I would like to firstly thank my supervisor, Dr. Stefano Leoni, for his expert guidance and support throughout the course of my PhD program. I am incredibly grateful for his help, and especially his patience and advice when things (often) didn't go according to plan.

For their support and friendship over my time in the Leoni group I would also like to thank Drs. Samuel Jobbins, Timothy Flack, Duncan Hardie and Darren Wragg. It wouldn't have been the same without you all, and that's mostly a good thing.

I would also like to thank the teams at Deregallera and KESS for their sponsorship and their help. It was a pleasure to work with you and I am grateful for the opportunity that you have provided to me.

A large part of my ability to complete this program has come from my wonderful family, to whom I am eternally grateful, and from my partner Kristi, who has been an immense support throughout, all of whom pushed me to continue and got me this far.

Chapter 1:

Thermoelectric Materials

For the underlying principles of this chapter “Thermoelectric Materials and Devices” by Lidong Chen, Ruiheng Liu and Xun Shi^[1] was used extensively.

1.1 - Use of Thermoelectric Devices

As the world moves to solve its dependency on environmentally damaging energy sources, much attention is given to renewable energy generation, such as wind and solar, or more efficient generation, such as nuclear power. These systems serve to replace the fossil fuel plants as a new first step in the energy production infrastructure. Thermoelectric generators are currently not proposed as first step energy production on this same scale, although they have been implemented for smaller systems such as watches and in places where conventional methods are impractical such as space probes. Instead, they are looked at in terms of integration into the system at later points to increase the efficiency of every step in the process, from energy generation to use. Heat is the largest source of loss in energy systems, and recapture and reintroduction of this waste heat energy has the capacity to increase the efficiency of almost every production, transfer and usage step. The energy efficiency of different power plants are given below, where the energy efficiency is defined as the amount of electricity produced per heat unit used relative to the theoretical maximum amount of electricity available from that heat unit.

Energy efficiency of production:

Coal 33%, Petroleum 31%, Natural Gas 43%, Nuclear 33%^[2]

Thermoelectric generation is not solely beneficial in energy scavenging and has many situational benefits. As mentioned above thermoelectric energy has been used to power a smartwatch, providing the benefit of not needing charging and relying instead on waste body heat, and a radioisotope thermoelectric generator is used in systems developed for deep space where reliability is important, but light is limited, reducing solar power's appeal. The reliability of thermoelectric devices derives from their lack of moving parts that might wear down, and their solid-state build allows great scalability, down to low surface area energy scavenging or heat management.

1.2 - The Thermoelectric Effect

Thermoelectric materials produce a potential difference when a temperature difference exists across the material, whereby charge carriers in the material diffuse along the temperature gradient from hot to cold, resulting in a build-up of positive or negative charge, dependent on the nature of the charge carrier.

The Seebeck Effect

The Seebeck effect was first discovered by A. Volta in 1794, then later independently rediscovered by T. Seebeck in 1821, and was identified as a thermoelectric effect by H. Ørsted in 1823. Seebeck observed that two differing metals joined into a closed loop and heated at the joins would deflect a compass needle, however misattributed this effect to a directly induced magnetic field, rather than an electric current.

The voltage gradient of the system in a steady state is given by:

$$\Delta V = S\Delta T \quad (1.1)$$

where S is the Seebeck coefficient, and ΔT is the difference in temperature across the material. ^[3]

The Peltier Effect

The Peltier effect, discovered by J. Peltier in 1834, exists as the mirror to the Seebeck effect in that an applied current instigates the movement of heat across a material by charge carriers. The heat generated at the junctions between materials is given by:

$$Q = (\Pi_A - \Pi_B)I \quad (1.2)$$

where Π_A and Π_B are the Peltier coefficients of the two conductors A and B , and I is the applied current from A and B . ^[1]

The Peltier effect and the Seebeck effect are linked via the temperature by the equation:

$$\Pi = TS \quad (1.3)$$

The Thomson Effect

It was discovered by W. Thomson (later Lord Kelvin) in 1854 that a single-material conductor with an applied current and temperature difference across its length will absorb or evolve heat across the length of the conductor, without the presence of a thermocouple, depending on the direction of the current relative to the temperature gradient. This is distinct from the Peltier effect in that the temperature absorption/evolution occurs across the material, rather than solely at the junctions. ^[1]

1.3 - Related Effects

The Hall Effect

Charge carriers in a conductor with an applied current 'curve' when in the presence of a magnetic field. The curve direction is relative to the current flow direction and the magnetic field direction, and is a result of the Lorentz forces upon the charge carriers. This is named after E. Hall, who first observed the effect in 1879, ^[4] and sees use largely in magnetometers for the detection of magnetic fields.

The Nernst-Ettinghausen Effects

The Nernst-Ettinghausen effects are two effects characterised by W. Nernst and A. Ettinghausen in 1886, whilst Nernst was studying as a PhD student under Ettinghausen. It was discovered that if a temperature gradient and magnetic field are applied to a conducting material perpendicular to each other, then an electric field will be created perpendicular to both. That is to say, if a temperature gradient is established along the x axis, and a magnetic field along the y axis, then an electric current will be produced along the z axis. This is in essence a combination of the Seebeck effect and the Hall effect, where charge carriers are moved along the temperature gradient, but are curved in opposing directions based on their charges (electrons or holes). This is designated the 1st Nernst-Ettinghausen effect, or simply the Nernst effect. ^[5]

It was also observed that when a magnetic field and an electric current are applied to a material orthogonal to each other, a temperature difference is observed orthogonal to both across the material, resulting in a heating at one end of the material. This is due to the accumulation of electrons at one end, and more collisions leading to the rise in temperature. This is designated the 2nd Nernst-Ettinghausen effect, or simply the Ettinghausen effect. ^[5]

The Righi-Leduc Effect

Discovered by A. Righi and S. Leduc, 1887. A material subjected to a magnetic field and an orthogonal temperature gradient will exhibit a second temperature gradient orthogonal to both. This is the thermal equivalent of the Hall effect. [6]

1.4 - Thermoelectric Devices

A thermoelectric device is comprised of two thermoelectric materials, one p -type consisting of positive charge carriers and one n -type consisting of negative charge carriers. These are ordered into 'legs' and arranged electrically in an alternating p - and n -type series, and thermally in parallel. This is shown in (Fig. 1.1) and can be seen that as the charge carriers move from the hot to the cold side of the device through thermal diffusion an electric flow is generated, with the current moving in line with the electron diffusion and in opposition to the hole diffusion.

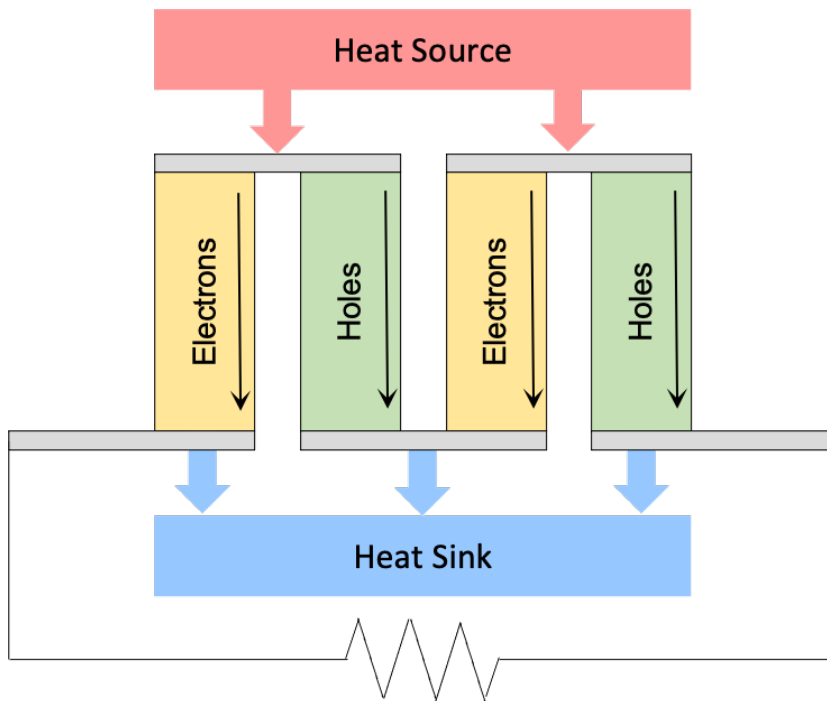


Figure 1.1: A thermoelectric device, showing two n - and two p -type thermoelectric legs. The black arrows represent the movement of charge carriers. The electrons and holes both move "top to bottom", which gives a total electron movement "right to left".

The Thermoelectric Figure of Merit

To compare thermoelectric materials and their suitability, the thermoelectric figure of merit (zT) is defined as

$$zT = \frac{\sigma S^2 T}{\kappa} \quad (1.4)$$

where σ is the electrical conductivity, S is the Seebeck coefficient, T is the temperature, and κ is the total thermal conductivity, the sum of the lattice and electronic thermal conductivities, κ_L and κ_e . The relation between these properties is shown in Fig. 1.2.

There are two interrelating properties that form adversely dependant relationships with the figure of merit. The relation between the Seebeck coefficient and the charge carrier concentration, and the relation between the electrical conductivity and the electronic component to the thermal conductivity.

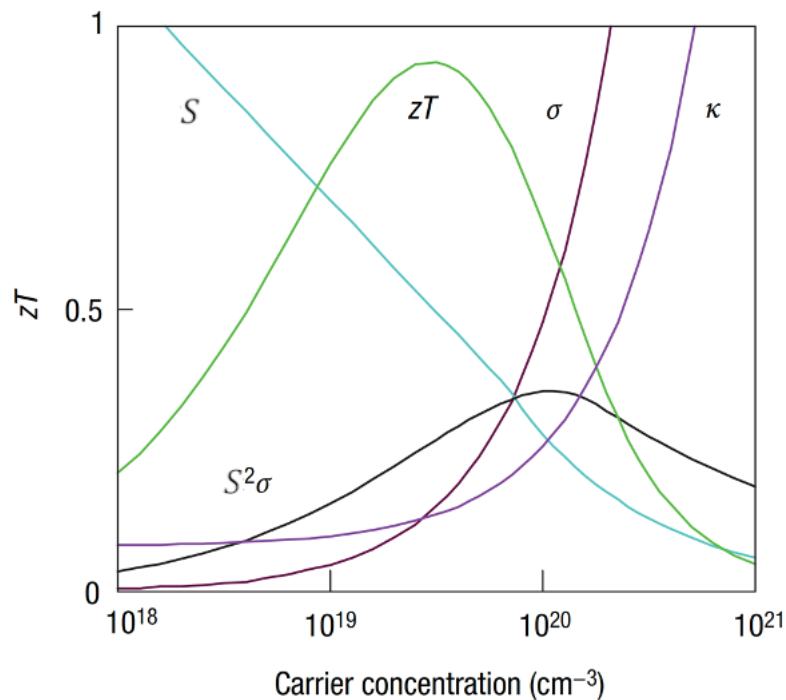


Figure 1.2: A representation of the relationship between the Figure of merit, zT , the Seebeck coefficient, S (α in original), the electrical conductivity, σ , and the thermal conductivity, κ , across carrier concentration levels. The power factor, $S^2\sigma$, is also shown.

Image obtained from [7].

The Seebeck coefficient is inversely related to the carrier concentration through the inverse power relationship:

$$S = \frac{8\pi^2 k_B^2}{3eh^2} m^* T \left(\frac{\pi}{3n} \right)^{\frac{2}{3}} \quad (1.5)$$

where n is the carrier concentration and m^* is the carrier effective mass.^[7] The carrier concentration is in turn related to the electrical conductivity through:

$$\sigma = ne\mu \quad (1.6)$$

where μ is the carrier mobility. This leads to the inverse relation between the Seebeck and the electrical conductivity through the carrier concentration.

The total thermal conductivity can be defined as the sum of the electronic and lattice thermal conductivities:

$$\kappa = \kappa_e + \kappa_L \quad (1.7)$$

The electronic component to the thermal conductivity is related to the electrical conductivity through the Wiedemann-Franz law:^[8]

$$\frac{\kappa_e}{\sigma} = LT \quad (1.8)$$

where L is the Lorenz number, which is generally equal to $2.44 \times 10^{-8} \text{ W}\Omega\text{K}^{-2}$, however has been shown to vary somewhat by material and to be less reliable at intermediate temperatures.

These relationships set limitations on the improvement to zT possible through increased electrical conductivity, as any increase must be carefully balanced to not substantially disrupt either S or κ_e . The lattice thermal conductivity is of particular importance in the enhancement of zT as it is not included in the Wiedemann-Franz Law, and as such can be utilised as a method of zT improvement. That is to say that κ_L lowering will leave the

electronic properties undisturbed, and whilst lattice and structural changes will inevitably affect the electronic structure of the material, this approach can be undertaken without the explicit balancing relationship between two interdependent properties.

1.5 - Thermoelectrics vs. Pyroelectrics vs. Piezoelectrics

Two other effects share similarities with thermoelectrics in the generation of an electric current through a physical process phenomenon, pyroelectricity and piezoelectricity. These are interrelated by the asymmetric nature of the crystal structure, which provides an easier path for ion movement along one axis than the others.

Pyroelectricity is the characteristic of certain materials that have a spontaneous electric potential, where the material can generate a temporary voltage when heated or cooled^[9]. This is similar to the thermoelectric effect in the production of an electric current through a temperature change but through the polarisation of atoms within the crystal structure. As such, the potential difference is only present as the temperature changes, and a constant temperature, high or low, will diminish this effect. Ferroelectric materials also have a spontaneous electric potential, and exhibit pyroelectricity, but the internal electric potential can be reversed by the application of an external electric current. All ferroelectric materials are also pyroelectric, but not all pyroelectric materials are ferroelectric.

Piezoelectricity is the accumulation of electrical charge in certain materials due to mechanical stress, or the change in structure due to an applied electric current.^[10]

1.6 - Thermoelectric Cooling vs. Mechanical Refrigeration

Peltier coolers are used in niche small-scale, localised cooling, where mechanical refrigeration has low efficiency, high weight, and high cost. Thermoelectric cooling is not as powerful as compression cooling and is usually far more sensitive to outside temperature. Thermoelectric devices usually won't be able to produce a temperature difference of more than ~70K in truly ideal settings and will consume a large amount of power compared to mechanical refrigeration on all but the smallest of cooling areas.^[11]

Positive attributes of Peltier cooling are that they have no moving parts, making them less likely to break or wear due to mechanical stress. They also allow a fine-tuned temperature control as the temperature difference is directly proportional to the applied current. This allows numerous uses in scientific or industrial fields that require specific and controlled temperature, with accuracies as low as $\pm 0.01\text{K}$. There is also an environmental benefit, as

thermoelectric devices do not require refrigerants, which are often harmful to humans or the environment.^[11]

1.7 - Problems with Thermoelectrics

Electrical conductivity vs. Thermal conductivity

As shown above in equation 1.8, the Wiedemann-Franz law inversely links the electronic contribution to the thermal conductivity of a material with the electronic conductivity, via the temperature and a Lorenz factor, given as $L = 2.44 \times 10^{-8} \text{ W}\Omega\text{K}^{-2}$. This relationship shows that increasing the electronic conductivity will proportionally increase the thermal conductivity, and that attempting to decrease the electronic contribution to the thermal conductivity will proportionally decrease the electronic conductivity. This also shows that at high temperatures, the thermal conductivity increases in relation to the electrical conductivity, lowering the efficiency of thermoelectric devices, which require a high electrical conductivity and low thermal conductivity.

A number of caveats with, and exceptions to, this law exist. Firstly, the Lorenz number, while explicitly given, has been shown to differ depending on the material in question. Experimental measurements of the Lorenz number showed values from $2.23 \times 10^{-8} \text{ W}\Omega\text{K}^{-2}$ for copper to $3.2 \times 10^{-8} \text{ W}\Omega\text{K}^{-2}$ for tungsten. These numbers also depend on the temperature, with a difference of $0.18 \times 10^{-8} \text{ W}\Omega\text{K}^{-2}$ between 0°C and 100°C for molybdenum. The Wiedemann-Franz law is generally valid at very high and very low temperatures, but is less so at the intermediate temperatures, such as those where a thermoelectric device may more frequently be in operation.

There are also more explicit exceptions to the Wiedemann-Franz law, such as with $\text{Li}_{0.9}\text{Mo}_6\text{O}_{17}$,^[12] where the decreasing temperature from the metallic phase diverges the expected thermal and electrical conductivities due to spin-charge separation, and VO_2 ,^[13] where nearing the metal-insulator transition in the metallic phase causes a far lower electronic contribution to thermal conductivity than predicted.

Weight vs Efficiency (Moving Systems)

When thermoelectric devices are applied to moving systems, such as a car exhaust to scrape energy waste, the weight of the system is relevant to the measured efficiency of the device and method. A heavy device would provide an extra load for the moving system, and so require excess energy to be applied. Therefore, the energy regained from the

thermoelectric effect must be larger than the energy required to move the device, and in practice must be sufficiently greater, such that the device is worth the development and material costs associated.

Large, Constant Temperature Gradient Needed

In order to maintain efficiency, a large temperature difference must be kept across the device. As the system moves heat across from the hot to cold side of the device, there must be an efficient heat sink to sufficiently dissipate that heat away from the cold side to the surroundings in order to keep the heat difference. This is usually accomplished by the use of air or water cooling, and as such would often require a dedicated cooling system with its own limitations as well as operating costs.

1.8 - Electronic Effect Improvement

Both the Seebeck Coefficient and the Electron Conductivity are properties tied to the nature of the electronic band structure, and both values contribute positively to a thermoelectric device's efficiency.

Charge Carrier Density

The most immediately obvious form of doping to improve the thermoelectric efficiency is focused on improving the charge carrier density. This form of doping requires aiming at an n - or p -doped system, as the addition of both n - and p -type charge carriers would adversely affect the Seebeck due to competition caused by both negative and positive charge movement along the temperature gradient. Increasing the charge carrier concentration understandably has a positive effect on the electrical conductivity, however charge carrier concentration is inversely related to the Seebeck coefficient. This means the system must be tailored to balance these two competing mechanisms in order to maximise the power factor of a doped thermoelectric.

Charge Carrier Effective Mass

The effective mass of the charge carriers also exhibits a relationship between the Seebeck coefficient and the electrical conductivity that must be balanced for optimising thermoelectric efficiency. A material with charge carriers of large effective masses will produce a high Seebeck coefficient, but due to the slower movement of the heavier carriers, the electrical conductivity will be adversely affected. This relationship is a particularly complex one, and as such it is harder to quantify which direction one should push a system

when doping, with materials of both high and low charge carrier effective masses showing strong thermoelectric properties.

The Rashba Effect

The Rashba effect is a band splitting effect through a spin-orbit coupling, produced by heavy atoms in an asymmetric crystal system, where a charged particle with spin feels a magnetic effect on moving through an electric field.

This effect leads to sharp features in the DOS near the Fermi level, enhancing the Seebeck coefficient, and can also lead to an internal electric field which lowers κ_l through enhanced anharmonicity, and softens bonds, lowering the group velocity of phonons. This effect is seen in Sn-doped GeTe.^[14]

Resonant Levels

Impurity levels in conduction or valence band induce a DOS peak at the resonance energy through electron coupling.^[15] Resonance levels were first discovered in metals but have since been observed in semiconductors such as Bi₂Te₃. A weakly bound electron in a donor impurity close to the conduction band edge can be excited into the conduction band, leading to the creation of a resonance level within the band, causing a spike in the DOS.

At low temperatures, when phonon scattering is weak, resonant levels provide a resonant scattering mechanism which, through the Mott relation, causes an increase in the Seebeck Coefficient.

Critical Phenomena-Induced Effects

Through the use of electronic phase transitions, enhanced Seebeck coefficients can be obtained from access to electronic microstates. This effect is harmed by associated structural phase transition, and so an electronic phase transition without structural phase transition would be effective. This is seen as the analogue to the ratios between the specific heat capacities of constant pressure and volume, C_P and C_V .^[16]

$$\gamma_{PV} = \frac{C_P}{C_V} \quad (1.9)$$

$$\gamma_{Ei} = 1 + ZT \quad (1.10)$$

In general, the ratio γ_{PV} is low, but at phase transitions can be significantly higher. This, along with the theorised symmetry between γ_{PV} and γ_{Ei} suggests a similar effect in

thermoelectric efficiency at transition critical points. This effect has been reported in Iodine^[17] and Silver^[18] doped Cu₂Se systems in their temperature phase transitions at 400K.

1.9 - Phonon Disruption

Where the movement of electronic charge carriers are the heat transport mechanism for the electronic thermal conductivity, the phonon pathway gives the heat transport mechanism for the lattice thermal conductivity. The lattice contribution to the thermal conductivity can be described by the product of the heat capacity, C , the group velocity by group velocity matrix, $\mathbf{v} \otimes \mathbf{v}$, and the relaxation time, τ , of each phonon mode, summed over all modes and rescaled by volume:

$$\kappa_l = \frac{1}{NV_0} \sum_{\lambda} C_{\lambda} \mathbf{v}_{\lambda} \otimes \mathbf{v}_{\lambda} \tau_{\lambda} \quad (1.11)$$

where the mean free path of a phonon mode is given by the product of the group velocity and the lifetime of a phonon mode:

$$l_{\lambda} = v_{\lambda} \tau_{\lambda} \quad (1.12)$$

such that Equation 1.11 can be rewritten as:

$$\kappa_l = \frac{1}{NV_0} \sum_{\lambda} C_{\lambda} \mathbf{v}_{\lambda} \otimes l_{\lambda} \quad (1.13)$$

Therefore, it can be seen that lowering the lattice thermal conductivity can be achieved through two main pathways, the weakening of the phonon mode group velocities, or the disruption of the phonon mode mean free path.

The group velocities of a phonon mode are closely related to the phonon dispersion spectra, where flatter bands are indicative of a lower phonon mode group velocity^[19]. As such, the softening of these bands through intrinsic lattice structural changes is a key method for decreasing the lattice thermal conductivity of a material.

For the reduction of the phonon mode mean free path, scattering effects are often used. This can be achieved through many forms that introduce a disorder into the lattice of the crystal, as discussed below. This lowering of κ_L through phonon scattering approaches a minimum where the phonon mean free path reaches the size of the interatomic distance, the amorphous limit. At this limit heat is transported through random walks, without the aid of crystal periodicity.^[20]

Complex Unit Cell

A large, complex unit cell can be imagined as short-range disorder for a phonon or charge carrier passing through. Therefore, with reference to the disorder decreasing lattice thermal conductivity, it is logical that a complex unit cell will have a similarly beneficial effect on the zT of its corresponding material. This is shown in Bi_2Te_3 , with high lattice thermal conductivities which can be improved greatly by the addition of Cs layers to form CsBi_4Te_6 , increasing the unit cell complexity in an ordered manner and improving the thermoelectric properties.^[21]

Disordered Cell

Disordered unit cells can be effective at reducing lattice thermal conductivity. This disorder can be from interstitial sites, partial occupancies, or 'rattling atoms', as well as inherent alloying disorder. $\text{La}_{3-x}\text{Te}_4$ have low thermal conductivities attributed to x vacancies of non-uniform distribution.^[22] Structures containing large empty areas can benefit from the insertion of 'rattling atoms', and heavier atoms can further decrease the lattice thermal conductivity, with lower vibrational frequency linked to lower thermal conductivity.

Mass Effect

Heavy dopants can also lower the lattice thermal conductivity through lowering the frequency of the phonons, weakening them in heat transport. This can be seen when comparing the lattice thermal conductivities of tin sulphide (SnS) and tin selenide (SnSe). SnS , with the lighter sulphur atom, has a measured lattice conductivity larger than that of SnSe , with the heavier selenium, despite both systems sharing very similar relaxed structures (matching symmetry ($Pnma$) and comparable cell lattice constants).

Boundary Design

As mentioned above, the disruption of the phonon pathway can be used to greatly lower the lattice thermal conductivity of a material. Structural phase boundaries, such as between low and high temperature or pressure phases of a material, can produce a lattice mismatch

that disrupts the phonon movement without equally diminishing the electronic capability.^[23] This requires structural stress within the device, or a material that undergoes a phase transition within the operating temperature range, however, and so is practically more complex to achieve.

Another form of phase boundary can be produced with materials that exhibit intrinsic layered structures. These materials can show very low lattice thermal conductivities across the layered direction through phonon scattering as the vibrations transition through the alternating regimes, but the thermoelectric efficiency is harmed by the fact that these layering directions will often show lower electronic conductivity than the intra-layer directions as charge carriers must also bridge the layer gaps.

1.10 - Established Materials

The field of thermoelectrics is not a new one, although it is growing rapidly. The advances in high figure of merit materials ordered by their year of discover and the groups they belong to are shown in Fig. 1.3, where the general upward trend can be seen as materials are improved and the effects underlying their improvements better understood.

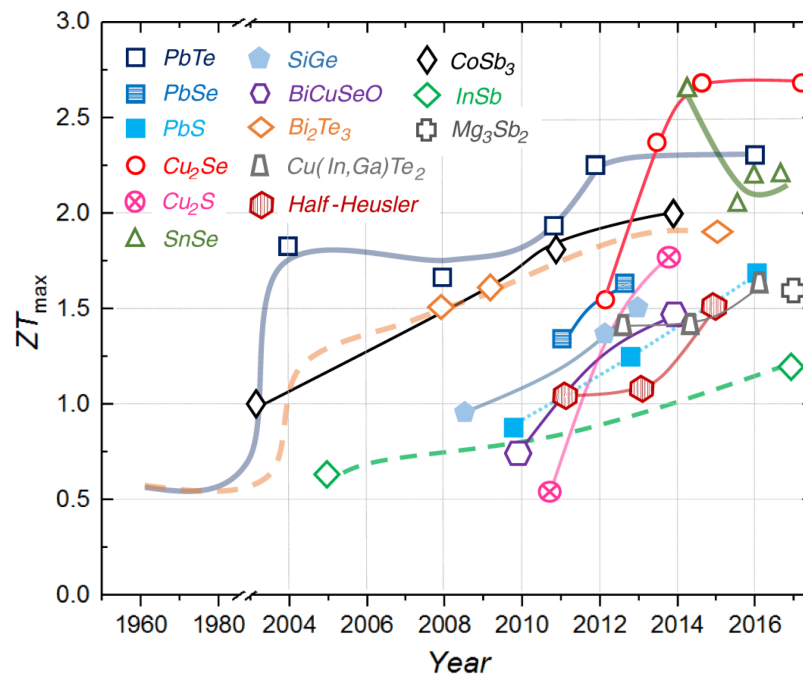


Figure 1.3: Maximum figure of merits obtained from various materials of differing types and their year of discovery. Image obtained from [24]

Chalcogenides

Bi_2Te_3 one of the most widely used low temperature thermoelectric materials, with a peak effective temperature around 500 K. ^[25] Heavy atoms disrupt the high frequency phonons and scatter effectively, thus lowering the material's κ_L . Bi_2Te_3 also exhibits electron scattering in the bismuth layers, due to their negative charge, and hole scattering in the telluride layers, which show a positive charge. This allows for the tailoring of the material to *n*- and *p*-doped systems by softening of these layers with telluride-selenium substitution in *n*-type, and bismuth-antimony substitution in *p*-type thermoelectrics. This alloying has been seen to improve the figure of merit to values of 1.41 and 1.13 for the *p*- and *n*-type figure of merits at 308 K. ^[26]

Lead telluride has also been shown to be a strong thermoelectric material with a good figure of merit, reaching 1.4 in the 700-850 K temperature range, ^[27] and strong chemical stability, allowing for a wide application. ^[28] Due to its early discovery, it has also been rigorously studied and improved upon through doping, to tailor the material to an *n*- or *p*-type thermoelectric. Issues have been raised in the use of PbTe however, largely due to its relative toxicity, fuelling the search for less harmful alternatives.

Both tin and germanium chalcogenides have been explored as strong thermoelectrics, ^[29] with similar structures that exhibit a divergence from the NaCl-like symmetry of PbTe in the stretching along the *c*-axis leading to a zig-zag motif within the layer. Tin selenide in particular has been noted as a material with very strong potential in thermoelectric application. With a strong Seebeck coefficient and low κ_L , very high *p*- and *n*- type figure of merits have been recorded, with values of 2.6 at 923 K for single-crystal, ^[30] and 3.1 at 783 K in polycrystalline SnSe. ^[31]

Cu_2Se reaches a high *zT* of 1.5 at 1000 K ^[32] through superionic Cu atoms exhibiting an ionic liquid mobility, allowing for a very low lattice thermal conductivity through the evasion of the phonon-glass minimum heat transport, instead following a phonon-liquid model. Below 400 K the copper atoms are structurally stable and do not exhibit ionic mobility, but still show reasonable *zT* values, whereas above this temperature the system undergoes a phase transition that allows for the low lattice thermal conductivity whilst retaining a strong Seebeck coefficient and electrical conductivity. However, the mobility of the Cu^+ ions leads to chemical instability within the system and make the material generally unsuitable for practical use. Various attempts have been made to further improve up these values, with particular focus on the mid-range temperatures. The use of indium nano-inclusion in the

Cu₂Se lattice have led to large gains in this regard, with recorded zT values of 2.6 at 850 K and an averaged zT of 1.5 across the 450-850 K temperature range.^[33] The inclusion of indium also shows a stabilisation of the Cu⁺ migration, leading to a more stable material in the working temperature range.

Half-Heusler Alloys

Materials of the form XYZ, where X and Y are transition metals, and Z is a p-block element. These are arranged in a face-centred cubic lattice, with vacancies in the lattice distinguishing the Half-Heusler XYZ from the Full-Heusler X₂YZ. Half-Heusler alloys show strongest figure of merits at high working temperatures, and are more often better suited to *n*-type than *p*-type thermoelectric performance. They have been characterised with figure of merits reaching around 1 above 700 K.^[34]

Skutterudites

CoSb₃, mid-temperature thermoelectric comprised of cheap and abundant materials, with a relatively stable thermoelectric performance and shown to exhibit a figure of merit of 1.3 at 850 K.^[35] Rattling atoms can be added to the caged structure, where elements that are more electronically neutral are favoured, although they are also harder to keep caged within the voids.^[36]

Organic Semiconductors

A relatively new group of materials showing promise in thermoelectric application are the organic polymers. These are relatively low cost and are particularly earth abundant, as well as displaying other interesting mechanical properties such as flexibility. They generally exhibit very low lattice thermal conductivity, with operating ranges around room temperature. Poly(3,4-ethylenedioxythiophene) (PEDOT) has shown figure of merit maxima of 0.42 at room temperature,^[37] whereas the selenium-substituted diketopyrrolopyrrole polymer (PDPP-Se-12) reached a peak figure of merit of 0.22 at 328 K.^[38]

References

- [1] L. Chen, R. Liu and X. Shi, *Thermoelectric Materials and Devices*, Elsevier, 2021.
- [2] "Power Plant Operations Report," U.S. Energy Information Administration, 2020.
- [3] A. I. Hofmann, R. Kroon and C. Müller, "13 - Doping and Processing of Organic Semiconductors for Plastic Thermoelectrics," in *Handbook of Organic Materials for Electronic and Photonic Devices*, Woodhead Publishing, 2019, pp. 429-449.
- [4] E. H. Hall, "On a New Action of the Magnet on Electric Currents," *American Journal of Mathematics*, vol. 2, no. 3, pp. 287-292, 1879.
- [5] K. Behnia and H. Aubin, "Nernst Effect in Metals and Superconductors: A Review of Concepts and Experiments," *Reports on Progress in Physics*, vol. 79, p. 046502, 2016.
- [6] O. Lindberg, "Hall Effect," *Proceedings of the IRE*, vol. 40, no. 11, pp. 1414-1419, 1952.
- [7] G. J. Snyder and E. S. Toberer, "Complex Thermoelectric Materials," *Nature Materials*, vol. 7, no. 2, pp. 105-114, 2008.
- [8] M. Jonson and G. D. Mahan, "Mott's Formula for the Thermopower and the Wiedemann-Franz Law," *Physical Review B*, vol. 21, no. 10, pp. 4223-4229, 1980.
- [9] P. Muralt, "Pyroelectricity," in *Encyclopedia of Condensed Matter Physics*, Elsevier, 2005, pp. 441-448.
- [10] H.-P. Kim, W.-S. Kang, C.-H. Hong, G.-J. Lee, G. Choi, J. Ryu and W. Jo, "Piezoelectrics," in *Advanced Ceramics for Energy Conversion and Storage*, Elsevier, 2020, pp. 157-206.
- [11] D. Zhao and G. Tan, "A Review of Thermoelectric Cooling: Materials, Modeling and Applications," *Applied Thermal Engineering*, vol. 66, no. 1, pp. 15-24, 2014.
- [12] N. Wakeham, A. F. Bangura, X. Xu, J.-F. Mercure, M. Greenblatt and N. E. Hussey, "Gross Violation of the Wiedemann-Franz Law in a Quasi-One-Dimensional Conductor," *Nature Communications*, vol. 2, no. 396, 2011.
- [13] S. Lee, K. Hippalgaonkar, F. Yang, J. Hong, C. Ko, J. Suh, K. Liu, K. Wang, J. J. Urban, X. Zhang, C. Dames, S. A. Hartnoll, O. Delaire and J. Wu, "Anomalously Low Electronic Thermal Conductivity in Metallic Vanadium Dioxide," *Science*, vol. 355, no. 6323, pp. 371-374, 2017.
- [14] M. Hong, W. Lyv, M. Li, S. Xu, Q. Sun, J. Zou and Z.-G. Chen, "Rashba Effect Maximises Thermoelectric Performance of GeTe Derivatives," *Joule*, vol. 4, no. 9, pp. 2030-2043, 2020.
- [15] J. P. Heremans, B. Wiendlocha and A. M. Chamoire, "Resonant Levels in Bulk Thermoelectric Semiconductors," *Energy & Environmental Science*, vol. 5, no. 2, pp. 5510-5530, 2012.
- [16] C. B. Vining, "The Thermoelectric Process," *MRS Proceedings*, vol. 478, pp. 3-13, 1997.
- [17] H. Liu, X. Yuan, P. Lu, X. Shi, F. Xu, Y. He, Y. Tang, S. Bai, W. Zhang, L. Chen, Y. Lin, L. Shi, H. Lin, X. Gao, X. Zhang, H. Chi and C. Uher, "Ultrahigh Thermoelectric Performance by Electron and Phonon Critical Scattering in Cu₂Se_{1-x}Tx," *Advanced Materials*, vol. 25, no. 45, pp. 6607-6612, 2013.
- [18] D. R. Brown, T. Day, K. A. Borup, S. Christensen, B. B. Iversen and G. J. Snyder, "Phase Transition Enhanced Thermoelectric Figure-of-Merit in Copper Chalcogenides," *APL Materials*, vol. 1, no. 5, p. 052107, 2013.
- [19] O. Bourgeois, D. Tainoff, A. Tavakoli, Y. Liu, C. Blanc, M. Boukhari, A. Barski and E. Hadji, "Reduction of Phonon Mean Free Path: From Low-Temperature Physics to

- Room Temperature Applications in Thermoelectricity," *Comptes Rendus Physique*, vol. 17, no. 10, pp. 1154-1160, 2016.
- [20] D. G. Cahill, S. K. Watson and R. O. Pohl, "Lower Limit to the Thermal Conductivity of Disordered Crystals," *Physical Review B*, vol. 46, no. 10, pp. 6131-6140, 1992.
- [21] D.-Y. Chung, T. P. Hogan, M. Rocci-Lane, P. Brazis, J. R. Ireland, C. R. Kannewurf, M. Bastea, C. Uher and M. G. Kanatzidis, "A New Thermoelectric Material: CsBi₄Te₆," *Journal of the American Chemical Society*, vol. 126, no. 20, pp. 6414-6428, 2004.
- [22] A. F. May, J.-P. Fleurial and G. J. Snyder, "Optimizing Thermoelectric Efficiency in La_{3-x}Te₄ via Yb Substitution," *Chemistry of Materials*, vol. 22, no. 9, pp. 2995-2999, 2010.
- [23] D. Selli, S. E. Boufelfel, P. Schapotschnikow, D. Donadio and S. Leoni, "Hierarchical Thermoelectrics: Crystal Grain Boundaries as Scalable Phonon Scatterers," *Nanoscale*, vol. 8, no. 6, pp. 3729-3738, 2016.
- [24] J. He and T. Tritt, "Advances in Thermoelectric Materials Research: Looking Back and Moving Forward," *Science*, vol. 357, no. 6358, p. eaak9997, 2017.
- [25] Z. Dashevsky and S. Skipidarov, "Investigating the Performance of Bismuth-Antimony Telluride," in *Novel Thermoelectric materials and Device Design Concepts*, Springer, 2019, pp. 3-22.
- [26] O. Yamashita, S. Tomiyoshi and K. Makita, "Bismuth Telluride Compounds with High Thermoelectric Figures of Merit," *Journal of Applied Physics*, vol. 93, no. 1, pp. 368-374, 2003.
- [27] A. D. LaLonde, Y. Pei and G. J. Snyder, "Reevaluation of PbTe_{1-x} as High Performance n-type Thermoelectric Material," *Energy & Environmental Science*, vol. 4, no. 6, pp. 2090-2096, 2011.
- [28] Z. H. Dughaish, "Lead Telluride as a Thermoelectric Material for Thermoelectric Power Generation," *Physica B: Condensed Matter*, vol. 322, no. 1-2, pp. 205-223, 2002.
- [29] B. Ul-Haq, S. AlFaify and A. Laref, "Exploring Novel Flat-Band Polymorphs of Single-Layered Germanium-Sulfide for High-Efficiency Thermoelectric Applications," *The Journal of Physical Chemistry C*, vol. 123, no. 30, pp. 18124-18131, 2019.
- [30] L.-D. Zhao, S.-H. Lo, Y. Zhang, H. Sun, G. Tan, C. Uher, C. Wolverton, V. P. Dravid and M. G. Kanatzidis, "Ultralow Thermal Conductivity and High Thermoelectric Figure of Merit in SnSe Crystals," *Nature*, vol. 508, no. 7496, pp. 373-377, 2014.
- [31] C. Zhou, Y. K. Lee, Y. Yu, S. Byun, Z.-Z. Luo, H. Lee, B. Ge, Y.-L. Lee, X. Chen, J. Y. Lee, O. Cojocaru-Mirédin, H. Chang, J. Im, S.-P. Cho, M. Wuttig, V. P. Dravid, M. G. Kanatzidis and I. Chung, "Polycrystalline SnSe with a Thermoelectric Figure of Merit Greater than the Single Crystal," *Nature Materials*, vol. 20, pp. 1378-1384, 2021.
- [32] H. Liu, X. Shi, F. Xu, L. Zhang, W. Zhang, L. Chen, Q. Li, C. Uher, T. Day and G. J. Snyder, "Copper Ion Liquid-Like Thermoelectrics," *Nature Materials*, vol. 11, no. 5, pp. 422-425, 2012.
- [33] A. A. Olvera, N. A. Moroz, P. Sahoo, P. Ren, T. P. Bailey, A. A. Page, C. Uher and P. F. P. Podeu, "Partial Indium Solubility Induces Chemical Stability and Colossal Thermoelectric Figure of Merit in Cu₂Se," *Energy & Environmental Science*, vol. 10, no. 7, pp. 1668-1676, 2017.
- [34] R. He, H. Zhu and S. Chen, "Half-Heusler Thermoelectrics," in *Novel Thermoelectric Materials and Device Design Concepts*, Springer, 2019, pp. 203-266.

- [35] Y. Tang, R. Hanus, S. Chen and G. J. Snyder, "Solubility Design Leading to High Figure of Merit in Low-Cost Ce-CoSb₃ Skutterudites," *Nature Communications*, vol. 6, no. 1, 2015.
- [36] G. Rogl and P. Rogl, "Skutterudites: Progress and Challenges," in *Novel Thermoelectric Materials and Device Design Concepts*, Springer, 2019, pp. 177-201.
- [37] G.-H. Kim, L. Shao, K. Zhang and K. P. Pipe, "Engineered Doping of Organic Semiconductors for Enhanced Thermoelectric Efficiency," *Nature Materials*, vol. 12, no. 8, pp. 719-723, 2013.
- [38] J. Ding, Z. Liu, W. Zhao, W. Jin, L. Xiang, Z. Wang, Y. Zeng, Y. Zou, F. Zhang, Y. Yi, Y. Diao, C. R. McNeill, C.-a. Di, D. Zhang and D. Zhu, "Selenium-Substituted Diketopyrrolopyrrole Polymer for High-Performance p-Type Organic Thermoelectric Materials," *Angewandte Chemie International Edition*, vol. 58, no. 52, pp. 18994-18999, 2019.

Chapter 2:

Computational Methods

The following references have been essential for the completion of this section: Density Functional Theory: A Practical Introduction, by David S. Sholl and Janice A Steckel. ^[1] Introduction to Computational Chemistry, Frank Jensen, ^[2] Phonons and related crystal properties from density-functional perturbation theory, Stefano Baroni, Stefano de Gironcoli, and Andrea Dal Corso. ^[3]

Chemistry is the study of substances, the changes they undergo and the mechanisms by which they undergo them. The application of theoretical methodologies allows for the expansion of this study to theoretical materials, either for a deeper understanding of the mechanics or as a search for improvements on the materials currently available. Whereas these methods are currently the basis for computational modelling and study, the theory predates the advent of computers and instead involved the painstaking calculation of energies by hand. Thankfully for modern day theoretical chemists, this is no longer the case, and instead the rapid increase in computational power, as well as the increased accessibility of computers to theoreticians, have led to a wide range of complex equations and models for the characterisation of and experiment on new and complex materials.

2.1 – Theoretical Background

2.1.1 - Schrödinger Equation

In 1925, Erwin Schrödinger proposed a theory for the description of a quantum-mechanical system. ^[4] This theory was based on the wave-like properties of matter and involved the characterisation of the wavefunction, which is finite, single-valued, and continuous. This wavefunction maps to real quantities via $\Psi^*\Psi$, where Ψ^* is the complex conjugate of the wavefunction Ψ .

The time-independent Schrödinger equation, for the description of stationary states, is:

$$\hat{H}|\Psi\rangle = E|\Psi\rangle \quad (2.1)$$

Where the wavefunction is an eigenfunction of the Hamiltonian operator, and the energy E is the eigenvalue. This Hamiltonian is the sum of the kinetic and potential energy operators, for a single particle taking the form:

$$\hat{H} = \hat{T} + \hat{V} \quad (2.2)$$

Such that:

$$\hat{H} = -\frac{\hbar^2}{2m}\nabla^2 + V(\mathbf{r}, t) \quad (2.3)$$

Where m is the particle mass, \hbar is the reduced Planck's constant and ∇^2 is the Laplace operator, the sum of second partial derivatives with respect to Cartesian coordinates:

$$\nabla^2 = \frac{\partial^2}{\partial x^2} + \frac{\partial^2}{\partial y^2} + \frac{\partial^2}{\partial z^2} \quad (2.4)$$

When applied to an N -particle system, the kinetic operator is simply the sum of all independent particle kinetic operators, whereas the potential operator is a function of all the particles spatial positions and time:

$$\hat{V} = V(\mathbf{r}_1, \mathbf{r}_2, \dots, \mathbf{r}_N, t) \quad (2.5)$$

This gives the N -particle Schrödinger Hamiltonian as:

$$\hat{H} = -\frac{\hbar^2}{2} \sum_n^N \frac{1}{m_n} \nabla_n^2 + V(\mathbf{r}_1, \mathbf{r}_2, \dots, \mathbf{r}_N, t) \quad (2.6)$$

As the potential now depends on the spatial positions of all particles, this enters a many-body problem into the Schrödinger equation.

Hartree and Hartree-Fock

The Hartree ^[5] method involved the characterisation of an electron field using a single potential so as to reduce the complexity of the calculation from one of $3N$ -dimensions per N electrons to simply 3-dimensions per N electrons. This is achieved through the simplification of the Hamiltonians potential operator such that the electrons are non-interacting, and their positions decoupled. From this, equation 2.6 can be reduced to simply the product of single-electron orbital wavefunctions, ϕ_i , and the energy of the electron defined by:

$$\left\{ -\frac{\hbar^2}{2m} \nabla_i^2 + V(\mathbf{r}) \right\} \phi_i(\mathbf{r}) = \varepsilon_i \phi(\mathbf{r}) \quad (2.7)$$

with the full system non-interacting wavefunction, Φ , is defined by the product of the ground state orbital wavefunctions:

$$\Phi(\mathbf{r}_1, \mathbf{r}_2, \dots, \mathbf{r}_N) = \phi_0(\mathbf{r}_1) \phi_0(\mathbf{r}_1) \dots \phi_0(\mathbf{r}_N) \quad (2.8)$$

The potential of the orbital wavefunction is given by:

$$V(\mathbf{r}) = V_N(\mathbf{r}) + V_H(\mathbf{r}) \quad (2.9)$$

where $V_N(\mathbf{r})$ is the potential from the electron-nucleus interaction:

$$V_N(\mathbf{r}) = -\frac{e^2}{4\pi\epsilon_0} \sum_j \frac{Z_j}{|\mathbf{r} - \mathbf{R}_j|} \quad (2.10)$$

and $V_H(\mathbf{r})$ is the potential describing the approximate interaction of the electron with all others:

$$V_H(\mathbf{r}) = \frac{e^2}{4\pi\epsilon_0} \int \frac{[n(\mathbf{r}')]^2}{|\mathbf{r} - \mathbf{r}'|} d^3r' \quad (2.11)$$

In this potential, $n(\mathbf{r}')$ is the charge density and is determined by the solution to the orbital Schrödinger equation through:

$$n(\mathbf{r}) = \sum_i |\phi_i(\mathbf{r})|^2 \quad (2.12)$$

This self-referential aspect leads to the self-consistent field (SCF) approach, where the charge density must be re-evaluated until there is no change and can be assumed to be *self-consistent*.

The Hartree method has two main sources of error, exchange and correlation. The Hartree-Fock method partially corrects for this through the addition of the exchange energy from the Fock operator, ^[6] a Slater determinant, allowing for the correct application of the Pauli exclusion principle, where the wavefunction changes sign with the exchange of two electrons. This accounts for one major source of error with the Hartree method, but the use of non-interacting single electron wavefunctions gives the second major error, the correlation energy. The Slater determinant takes the form:

$$\Phi = \frac{1}{\sqrt{N!}} \begin{vmatrix} \phi_1(\mathbf{r}_1) & \phi_2(\mathbf{r}_1) & \dots & \phi_N(\mathbf{r}_1) \\ \phi_1(\mathbf{r}_2) & \phi_2(\mathbf{r}_2) & \dots & \phi_N(\mathbf{r}_2) \\ \vdots & \vdots & \ddots & \vdots \\ \phi_1(\mathbf{r}_N) & \phi_2(\mathbf{r}_N) & \dots & \phi_N(\mathbf{r}_N) \end{vmatrix} \quad (2.13)$$

And leads to a Fock operator in the form:

$$\hat{F} = -\frac{\hbar^2}{2m} \nabla^2 - \frac{e^2 Z}{4\pi\epsilon_0 r} + \sum_i (2\hat{J}_i - \hat{K}_i) \quad (2.14)$$

Where \hat{J}_i corresponds to the classical coulomb interaction between electrons, and \hat{K}_i is the exchange operator accounting for the error from discounting exchange energy.

Density-Functional Theory

“The electron density that minimises the energy of the overall function is the true electron density corresponding to the full solution of the Schrödinger equation”

Whilst the Hartree-Fock method contained the understanding that the charge density is required for the solution to the orbital wavefunction, it was not until the work of Hohenberg Kohn and Sham ^[7, 8] that the electron density was shown to fully determine all ground-state properties of an N -electron system:

$$E_0 = T[n(\mathbf{r})_0] + E_{ee}[n(\mathbf{r})_0] + E_{Ne}[n(\mathbf{r})_0] \quad (2.15)$$

where E_{ee} and E_{Ne} are the electron-electron and Nucleus-electron interaction energies. This allowed the energies of the system to be derived from its electron densities, rather than from its wavefunctions.

The Kohn-Sham energy functional then takes the form:

$$E[\psi_i] = E_{known}[\psi_i] + E_{XC}[\psi_i] \quad (2.16)$$

$$\begin{aligned} E_{known}[\psi_i] &= \frac{\hbar^2}{2m} \sum_i \int \psi_i^* \nabla^2 \psi_i d^3\mathbf{r} \\ &+ \int V(\mathbf{r})n(\mathbf{r})d^3\mathbf{r} \\ &+ \frac{e^2}{2} \int \int \frac{n(\mathbf{r})n(\mathbf{r}')}{|\mathbf{r} - \mathbf{r}'|} d^3\mathbf{r}d^3\mathbf{r}' \\ &+ \frac{1}{4\pi\epsilon_0} \frac{|q_1q_2|}{R^2} \end{aligned} \quad (2.17)$$

where the known terms to the Hohenberg-Kohn functional are the kinetic energies, the Coulomb interactions between the electrons and the nuclei, the Coulomb interactions between electrons, and the Coulomb interactions between nuclei, where q represents the charge on the atoms. This final term is frequently removed from the equation in line with the Born-Oppenheimer approximation and the assumption that the nuclear positions are fixed, thus this interaction energy becomes a constant. E_{XC} corresponds to the exchange correlation functional and consists of all the other quantum-mechanical effects.

The Kohn-Sham equation allows the calculation of the electron density by solving a set of equations each involving only a single electron, where the potential is given by:

$$\left[\frac{\hbar^2}{2m} \nabla^2 + V(\mathbf{r}) + V_H(\mathbf{r}) + V_{XC}(\mathbf{r}) \right] \psi_i(\mathbf{r}) = \varepsilon_i \psi_i(\mathbf{r}) \quad (2.18)$$

where $V(\mathbf{r})$ is the electron-nuclei interaction, $V_H(\mathbf{r})$ is the Hartree potential and describes the Coulomb repulsion between the electron and the electron density of all electrons. This includes an interaction of the electron and its contribution to the electron density, and the correction is part of the third term, $V_{XC}(\mathbf{r})$.

$$V_H(\mathbf{r}) = e^2 \int \frac{n(\mathbf{r}')}{|\mathbf{r} - \mathbf{r}'|} d^3r' \quad (2.19)$$

$$V_{XC}[n(\mathbf{r})] = \frac{\delta E_{XC}[n(\mathbf{r})]}{\delta n(\mathbf{r})} \quad (2.20)$$

Local Density Approximation

The exchange-correlation functional is still undefined, however it can be numerically approximated in the case of a uniform electron gas, and therefore when $n(\mathbf{r})$ is a constant. This is used in the Local Density Approximation (LDA), where the exchange-correlation energy at each point is set to the exchange-correlation energy of a uniform electron cloud of the same electron density. A true electron gas assumption is only useful for simple metallic systems, but its approximation in the calculation of the exchange correlation can be used with less restrictive calculation for the other terms.

$$E_{XC}^{LDA}[\rho] = \int \rho(\mathbf{r}) \varepsilon_{XC}(\rho(\mathbf{r})) d\mathbf{r} \quad (2.21)$$

where $\varepsilon_{XC}(\rho(\mathbf{r}))$ is the individual particles exchange-correlation energy, and given by

$$E_{XC}^{LDA}(\rho(\mathbf{r})) = E_X^{LDA}(\rho(\mathbf{r})) + E_C^{LDA}(\rho(\mathbf{r})) \quad (2.22)$$

as simply the combined exchange and correlation terms. The correlation term has varying methods for its calculation, whereas the value for the exchange term is given by

$$E_X^{LDA}[\rho] = -\frac{3}{4}\left(\frac{3}{\pi}\right)^{\frac{1}{3}} \int \rho(\mathbf{r})^{\frac{4}{3}} d\mathbf{r} \quad (2.23)$$

The LDA approach has also been expanded to include spin-polarised systems, by simply splitting the electron densities into their spin-up and spin-down equivalents

Generalised Gradient Approximation

The Generalised Gradient Approximation expands on the LDA by use of the second order Taylor expansion to include the electron density gradient, thus attempting to better characterise the varying electron density and move from a homogenous electron cloud to a more representative approximation.

$$E_{XC}^{GGA}[\rho_{\uparrow}, \rho_{\downarrow}] = \int \varepsilon_{XC}(\rho_{\uparrow}, \rho_{\downarrow}, \nabla\rho_{\uparrow}, \nabla\rho_{\downarrow}) \rho(\mathbf{r}) d^3\mathbf{r} \quad (2.24)$$

This can be improved further by including the second derivative of the electron density, as in Meta-GGA DFT, or by partially including Hartree-Fock calculated exact exchange correlation energy, as in hybrid functionals such as B3LYP (Becke 3-Parameter Lee-Yang-Parr)^[9, 10, 11]

2.1.2 - Pseudopotentials and Plane-Waves

Plane-Wave Basis Sets

For periodic systems the orbitals can be represented by the linear combination of repeating plane-waves rather than localised atom-centred orbitals, such as gaussians. These plane-waves exhibit a much simpler force calculation due to the exclusion of Pulay forces, which are errors in the ground state energy calculation caused by an incomplete basis set, occurring when the lattice parameters are changed such that the reciprocal lattice energy cutoff boundary no longer corresponds to a sphere. The exclusion of this error greatly simplifies cell and atomic relaxation calculations in plane-wave systems.

In order to fully describe the electron wavefunction, an infinite number of reciprocal sampling points are needed. To reach feasible levels this must be addressed. 24

$$\psi_n(\mathbf{r}) = u_n(\mathbf{r})e^{i\mathbf{k}\cdot\mathbf{r}} \quad (2.25)$$

which is the product of the periodic and plane-wave components, with \mathbf{k} representing the wave vector confined to the first Brillouin zone. The periodic component can be expanded to:

$$u_n(\mathbf{r}) = \sum_{\mathbf{G}} c_{n,\mathbf{G}} e^{i\mathbf{G}\cdot\mathbf{r}} \quad (2.26)$$

where $c_{n,\mathbf{G}}$ are the plane wave coefficients and \mathbf{G} are the reciprocal lattice vectors, such that when L is the lattice vector and m is an integer, $\mathbf{G}L = 2\pi m$. This can be reinserted into the electronic wavefunction to give:

$$\psi_n(\mathbf{r}) = \sum_{\mathbf{G}} c_{n,\mathbf{k}+\mathbf{G}} e^{i(\mathbf{k}+\mathbf{G})\cdot\mathbf{r}} \quad (2.27)$$

This leaves $c_{n,\mathbf{k}+\mathbf{G}}$ as the plane wave coefficient, which will be small for larger values of $|\mathbf{k} + \mathbf{G}|$. This allows the plane wave to be truncated such that only the reciprocal lattice vectors with kinetic energy below the cutoff value are used in the plane-wave expansion, greatly reducing the computational load. ^[12]

Pseudopotentials

Even with truncation, the plane-wave basis set can be very expensive when required to describe the core, near-nucleus electrons, which are less relevant to the bonding interatomic interactions. Pseudopotentials are used to approximate the complicated behaviour of the electrons within the context of the Schrödinger equation. Proposed by H. Hellmann in 1934, ^[13] they simplify the system by freezing the core electrons such that they are treated with the nuclei as a single ionised centre, leaving only the valence electrons described by the plane-waves, with fewer nodes present and matching the real wavefunction above a selected radial distance, the cut-off radius. This simplification allows the calculation to explicitly deal with only the valence, and not the core, electrons. This is of

particular importance in the use of plane-wave basis sets, which do not easily describe these core electrons. The two most common forms of pseudopotential are the Norm-conserving and the Ultrasoft pseudopotentials.

Norm-conserving pseudopotentials were theorised by D. Hamann, M. Schlüter and C. Chiang in 1979, and aim to optimise the transferability of the pseudopotential. That is, allowing the pseudopotential to remain effective and representative in the varying chemical environments, contrasting to prior methods that required orthogonalization to the core states and renormalisation for charge densities outside the core region. The initial norm-conserving pseudopotentials were presented with four requirements:

- “(1) Real and pseudo valence eigenvalues agree for a chosen "prototype" atomic configuration
- (2) Real and pseudo atomic wave functions agree beyond a chosen "core radius" r_c
- (3) The integrals from 0 to r of the real and pseudo charge densities agree for $r > r_c$ for each valence state (norm conservation).
- (4) The logarithmic derivatives of the real and pseudo wave function and their *first energy derivatives* agree for $r > r_c$ “ [14]

Ultrasoft pseudopotentials [15] do not require norm-conservation, which allows for a smaller basis-set and the use of far smaller cut-off values. However, this does introduce a generalised eigenvalue problem. The generalised eigenvalue problem is the problem of finding the non-zero vector v such that it satisfies the equation $Av = \lambda Bv$, where A and B are matrices and λ is the generalised eigenvalue of A and B when v is the generalised eigenvector.

2.1.3 - Tight Binding Approximation

The Tight-Binding (TB) approximation utilises the Linear Combination of Atomic Orbitals (LCAO) approach, suggested independently by Finkelstein and Horowitz for molecular orbitals, [16] and Bloch for solids [17] in 1928. This was expanded upon by Slater and Koster in 1954, but due to the required computation of the large number of complex integrals, it was deemed too demanding for full computation and only suggested with an interpolated approach. [18] With the vast improvements in computational ability achieved since the approach's inception, this limitation is no longer of significance.

The TB approach describes electrons tightly bound to the atomic core, experiencing only limited interaction with the surroundings, and showing strong similarities to the unbound atomic orbitals. Simplistically, the tight binding approximation is a very computationally inexpensive method which nonetheless still retains the correct quantum mechanical description of a system. This is important for systems containing a very large number of atoms, as the full wavefunction evaluation can become impractically complex. In the tight-binding approximation, the Hamiltonian is constructed from a parameterised set. The Hamiltonian matrix takes the form of an integral of three separate site functions, two orbital functions, and a potential function. This is a one-centre matrix element when all functions occupy the same site, or a two centre when the orbitals are on separate neighbouring sites and the potential also one of these sites. No other orientations are considered, and as such any not defined by one of these terms is disregarded. This gives the core principle of the tight-binding approximation, where the Hamiltonian is defined by only the nearest-neighbour interactions.

2.1.4 - Wannier Functions

Wannier functions are used as they are very efficient in the interpolation of band structures and evaluation of very dense-grid Brillouin zone integrals. These interpolated band structures allow complex electronic transport properties to be obtained through much less computationally demanding methods than through usual *ab-initio* methods.

Wannier90

For the determination of the Wannier functions, Wannier90^[19] was used.

Theorised by Gregory Wannier in 1937,^[20] Wannier functions are obtained through transformation of the crystal Bloch functions, such that the wave functions are orthogonal and closely related to the molecular orbitals of non-crystalline systems. These Wannier functions form a basis set from which various transport properties can be calculated, such as the Seebeck coefficient, electronic conductivity, and electronic contribution to the thermal conductivity.

The optimal Wannier functions for a system are not a simple mathematical consistency, as the Bloch orbital phases are not rigidly defined. This in turn means that the Wannier functions need to be selected to best represent the system through the minimisation of their spread.

The choice of Wannier function is evaluated through an initial guess Wannier function:

$$|w_{nR}\rangle = V \int_{BZ} \frac{d\mathbf{k}}{(2\pi)^3} e^{-i\mathbf{k}\cdot\mathbf{R}} \sum_{m=1}^J |\psi_{m\mathbf{k}}\rangle U_{mn\mathbf{k}} \quad (2.28)$$

where J is a set of bands such that the electronic states can also be described as a set of J Wannier functions, w_{nR} is a periodic Wannier function with quantum number \mathbf{R} , itself a conjugate variable of the Bloch wave vector \mathbf{k} , V is the volume of the unit cell, and $U_{\mathbf{k}}$ are unitary matrices used to mix Bloch states at the given \mathbf{k} , and representing the gauge freedom of the Bloch states, the ability to redefine the field, which is therefore inherent to the Wannier functions. The consequence of this is that a system for determining the most appropriate Wannier function is required, this is most commonly the maximally localised Wannier function (MLWF) where the Wannier functions are iteratively compared and the matrix $U_{\mathbf{k}}$ chosen such that the real space spread is minimised. The spread functional Ω is given by:

$$\begin{aligned} \Omega &= \sum_{n=1}^J [\langle w_{n0} | \mathbf{r} \cdot \mathbf{r} | w_{n0} \rangle - |\langle w_{n0} | \mathbf{r} | w_{n0} \rangle|^2] \\ &= \Omega_I + \tilde{\Omega} \end{aligned} \quad (2.29)$$

Where Ω_I is gauge-invariant and therefore not influenced by the choice of the unitary matrix, $U_{\mathbf{k}}$, and $\tilde{\Omega}$ is gauge-dependent and therefore the focus of the minimisation, with the two Ω decompositions defined by:

$$\Omega_I = \sum_n \left[\langle w_{n0} | \mathbf{r} \cdot \mathbf{r} | w_{n0} \rangle - \sum_{m\mathbf{R}} |\langle w_{m\mathbf{R}} | \mathbf{r} | w_{n0} \rangle|^2 \right] \quad (2.30)$$

and

$$\tilde{\Omega} = \sum_n \sum_{m\mathbf{R} \neq n0} |\langle w_{m\mathbf{R}} | \mathbf{r} | w_{n0} \rangle|^2 \quad (2.31)$$

where $\bar{\mathbf{r}}$ denotes the centre of the Wannier function such that $\langle r^2 \rangle_n - \bar{\mathbf{r}}_n^2$ is the Wannier function spread, and defined by:

$$\bar{\mathbf{r}}_n \equiv \langle w_{n0} | \mathbf{r} | w_{n0} \rangle = -\frac{1}{N} \sum_{k,b} w_b \mathbf{b} \text{Im} \ln M_{nn}^{(k,b)} \quad (2.32)$$

where w_b are the weights given to the finite-difference representation of $\nabla_{\mathbf{k}}$ for a given geometry, and the matrix of overlaps $M_{nn}^{(k,b)}$ is given by:

$$M_{nn}^{(k,b)} = \langle u_{m\mathbf{k}} | u_{n,\mathbf{k}+\mathbf{b}} \rangle \quad (2.33)$$

BoltzWann

To calculate the electronic transport properties with the obtained MLWF's, the BoltzWann package is utilised. ^[21] This is integrated into the Wannier90 code and calculates the transport properties from the Boltzmann transport equation. For this, the derivatives of the band energies across the k-space are required, given by:

$$v_i(n, \mathbf{k}) = \frac{1}{\hbar} \frac{\partial E_{n,\mathbf{k}}}{\partial k_i} \quad (2.34)$$

This complex calculation usually requires a dense, and computationally expensive, \mathbf{k} -mesh. BoltzWann aims to avoid this through the interpolation of the band structure with the MLWF basis set, and with the exclusion of low-lying bands, which are generally significantly less important to the transport than those around the Fermi level, to further reduce the computational load.

To determine the transport properties, the transport distribution function Σ_{ij} is used. This is defined as:

$$\Sigma_{ij}(E) = \frac{1}{V} \sum_{n,\mathbf{k}} v_i(n, \mathbf{k}) v_j(n, \mathbf{k}) \tau_{n\mathbf{k}} \delta(E - E_{n,\mathbf{k}}) \quad (2.35)$$

$E_{n,k}$ is the energy for band n at wavevector \mathbf{k} , v_i and v_j correspond to the i -th and j -th components of the velocity of band n at \mathbf{k} , where i and j are cartesian indices, and τ_{nk} is the electron relaxation time on band n at \mathbf{k} . This relaxation time is obtained through fitting of the relaxation time dependent electrical conductivity to experimental values, with the relaxation time independent Seebeck coefficient used as a reference for the corresponding chemical potential, μ , and is fixed for all values of μ using the constant relaxation-time approximation.

From this transport distribution function, the relevant properties can be obtained through the transport coefficient equations:^[22]

$$\sigma_{ij}(\mu, T) = e^2 \int_{-\infty}^{\infty} dE \left(-\frac{\partial f(E, \mu, T)}{\partial E} \right) \Sigma_{ij}(E) \quad (2.36)$$

$$[\sigma S]_{ij}(\mu, T) = \frac{e}{T} \int_{-\infty}^{\infty} dE \left(-\frac{\partial f(E, \mu, T)}{\partial E} \right) (E - \mu) \Sigma_{ij}(E) \quad (2.37)$$

$$K_{ij}(\mu, T) = \frac{1}{T} \int_{-\infty}^{\infty} dE \left(-\frac{\partial f(E, \mu, T)}{\partial E} \right) (E - \mu)^2 \Sigma_{ij}(E) \quad (2.38)$$

where $\delta f/\delta E$ is the derivative of the Fermi-Dirac distribution function with respect to the energy, σ is the electrical conductivity, S is the Seebeck tensor, and K is the K-coefficient, related to κ_e , the electronic contribution to the thermal conductivity, through the relation:

$$\kappa_e = K - T\sigma S^2 \quad (2.39)$$

The electronic thermal conductivity can also be separately calculated through the use of the Wiedemann-Franz Law:

$$L = \frac{\kappa}{\sigma T} = \frac{\pi^2}{3} \left(\frac{k_B}{e} \right)^2 = 2.44 \times 10^{-8} \text{ W}\Omega\text{K}^{-2} \quad (2.40)$$

2.1.5 - Heat Transport Equations

Atomic Vibration

For the determination of the heat transport properties of a crystal lattice, the vibrational properties of the ground-state must be obtained. The energy of this ground state can be obtained through the Schrödinger equation:

$$\mathcal{E}\Psi(\mathbf{R}) = \left(- \sum_I \frac{\hbar^2}{2M_I} \frac{\partial^2}{\partial \mathbf{R}_I^2} + E(\mathbf{R}) \right) \Psi(\mathbf{R}) \quad (2.41)$$

where \mathbf{R}_I is the coordinate value of atom I with mass M_I , \mathbf{R} is the set of all atomic coordinates, such that $\mathbf{R} \equiv \{\mathbf{R}_I\}$, and $E(\mathbf{R})$ is the Born-Oppenheimer energy surface, defined as the ground-state energy of a system with fixed nuclei positions and interacting electrons. The Hamiltonian of this energy is given by:

$$\begin{aligned} H_{BO}(\mathbf{R}) = & -\frac{\hbar^2}{2m} \sum_i \frac{\partial^2}{\partial \mathbf{r}_i^2} + \frac{e^2}{2} \sum_{i \neq j} \frac{1}{|\mathbf{r}_i - \mathbf{r}_j|} \\ & - \sum_{iI} \frac{Z_I e^2}{|\mathbf{r}_i - \mathbf{R}_I|} + E_N(\mathbf{R}) \end{aligned} \quad (2.42)$$

where Z_I is the charge of nucleus I , $-e$ is the charge of an electron, \mathbf{r}_i is the position of electron i , and $E_N(\mathbf{R})$ is the interaction energy between differing nuclei:

$$E_N(\mathbf{R}) = \frac{e^2}{2} \sum_{I \neq J} \frac{Z_I Z_J}{|\mathbf{R}_I - \mathbf{R}_J|} \quad (2.43)$$

In the structural determination of a system, the forces acting upon atoms are determined, such that the ground-state positions are defined as the overall structure at which the atomic forces are reduced to zero, given by:

$$\mathbf{F}_I \equiv - \frac{\partial E(\mathbf{R})}{\partial \mathbf{R}_I} = 0 \quad (2.44)$$

This allows the definition of the ground-state structure of a system, from which the vibrational frequencies, ω , can be obtained using the second derivative of $E(\mathbf{R})$, the derivative of the forces, scaled by nuclear mass.

$$\left| \frac{1}{\sqrt{M_I M_J}} \frac{\partial^2 E(\mathbf{R})}{\partial \mathbf{R}_I \partial \mathbf{R}_J} - \omega^2 \right| = 0 \quad (2.45)$$

The first and second derivative of the Born-Oppenheimer energy surface can be achieved through the use of the Hellmann-Feynman theorem,^[23] where the first derivative of a Hamiltonian, H_λ is given by the expectation value, in essence the weighted average of all possible outcomes, of the derivative of H_λ .

$$\frac{\partial E_\lambda}{\partial \lambda} = \left\langle \Psi_\lambda \left| \frac{\partial H_\lambda}{\partial \lambda} \right| \Psi_\lambda \right\rangle \quad (2.46)$$

where Ψ_λ is the eigenfunction of H_λ , corresponding to E_λ through $H_\lambda \Psi_\lambda = E_\lambda \Psi_\lambda$.

Therefore, the force can be defined as:

$$\mathbf{F}_I = - \frac{\partial E(\mathbf{R})}{\partial \mathbf{R}_I} = - \left\langle \Psi(\mathbf{R}) \left| \frac{\partial H_{BO}(\mathbf{R})}{\partial \mathbf{R}_I} \right| \Psi(\mathbf{R}) \right\rangle \quad (2.47)$$

where $\Psi(\mathbf{R})$ is the electronic ground-state wave function of H_{BO} . As the Born-Oppenheimer Hamiltonian depends on \mathbf{R} through the electron charge density the force can be evaluated as:

$$\mathbf{F}_I = - \int n_{\mathbf{R}}(\mathbf{r}) \frac{\partial V_{\mathbf{R}}(\mathbf{r})}{\partial \mathbf{R}_I} d\mathbf{r} - \frac{\partial E_N(\mathbf{R})}{\partial \mathbf{R}_I} \quad (2.48)$$

where $n_{\mathbf{R}}(\mathbf{r})$ is the ground-state electron charge density of configuration \mathbf{R} , and the electron-nucleus interaction, $V_{\mathbf{R}}(\mathbf{r})$, defined as:

$$V_{\mathbf{R}}(\mathbf{r}) = - \sum_{iI} \frac{Z_I e^2}{|\mathbf{r}_i - \mathbf{R}_I|} \quad (2.49)$$

The Hessian matrix of the Born-Oppenheimer energy surface Hamiltonian, H_{BO} , can then be obtained through the differentiation of the Hellmann-Feynman forces with respect to their nuclear coordinates

$$\begin{aligned} \frac{\partial^2 E(\mathbf{R})}{\partial \mathbf{R}_I \partial \mathbf{R}_J} &\equiv - \frac{\partial \mathbf{F}_I}{\partial \mathbf{R}_J} \\ &= \int \frac{\partial n_{\mathbf{R}}(\mathbf{r})}{\partial \mathbf{R}_J} \frac{\partial V_{\mathbf{R}}(\mathbf{r})}{\partial \mathbf{R}_I} d\mathbf{r} \\ &\quad + \int n_{\mathbf{R}}(\mathbf{r}) \frac{\partial^2 V_{\mathbf{R}}(\mathbf{r})}{\partial \mathbf{R}_I \partial \mathbf{R}_J} d\mathbf{r} + \frac{\partial^2 E_N(\mathbf{R})}{\partial \mathbf{R}_I \partial \mathbf{R}_J} \end{aligned} \quad (2.50)$$

This equation gives the basis for the linear response approach to computational calculation of vibrational properties, where the Hessian matrix is shown to depend on the ground-state energy, the charge density, and the charge density's linear response to the distortion of the ground-state atomic coordinates.

This potential energy surface Hessian can also be evaluated through the finite displacement method, where the atomic coordinates are adjusted in a supercell of multiple unit cell size, and the effects of these atomic displacements on the energy of the system are obtained. As such, the potential energy again takes the form of a function of all atomic coordinates, but with the inclusion of the unit cell designation l :

$$E(\mathbf{R}) = E[\mathbf{R}(k_1 l), \dots, \mathbf{R}(k_n l_N)] \quad (2.51)$$

where $\mathbf{R}(k_n l_N)$ is the point of the k^{th} atom in the l^{th} unit cell, where n is the total number of atoms in a unit cell, and N is the total number of unit cells in the full supercell. From this potential, the first and second derivatives of the energy can be defined by:

$$\mathbf{F}_a(jl) = -\frac{\partial E(\mathbf{R})}{\partial \mathbf{R}_a(kl)} \quad (2.52)$$

$$\Phi_{ab}(jl, j'l') = \frac{\partial^2 E(\mathbf{R})}{\partial \mathbf{R}_a(kl) \partial \mathbf{R}_b(k'l')} = -\frac{\partial \mathbf{F}_b(k'l')}{\partial \mathbf{R}_a(kl)} \quad (2.53)$$

where a and b are cartesian indices. This second order force constant can be approximated as

$$\Phi_{ab}(kl, k'l') \approx -\frac{\mathbf{F}_b(k'l'; \Delta \mathbf{R}_a(kl)) - \mathbf{F}_b(k'l')}{\Delta \mathbf{R}_a(kl)} \quad (2.54)$$

where $\mathbf{F}_b(k'l'; \Delta \mathbf{R}_a(kl))$ are the forces acting upon atom \mathbf{R}_a with finite displacement of $\Delta \mathbf{R}_a(kl)$. With the assumption that the system is in a relaxed ground state configuration, the forces $\mathbf{F}_b(k'l')$ can be assumed to be zero

Phonopy and Phono3py

The phonon and heat transport properties were evaluated through the Phonopy^[24] and Phono3py^[25] packages. Phono3py determines the vibrational properties of the crystal through the frozen-phonon approach, where a finite displacement is applied to a system of multiple unit-cell size

The approach focuses on the determination of the phonon lifetimes calculated from the imaginary part of the phonon self-energy, where the third order interactions are assumed to have the most significant contribution.

The Hamiltonian H can be expressed as:

$$H = \Phi_0 + H_H + H_3 + \dots, \quad (2.55)$$

Where Φ_0 is the constant potential, H_H is the harmonic Hamiltonian and H_3 is the three-body crystal potential. The harmonic Hamiltonian can be expressed as:

$$H_H = \sum_{\lambda} \hbar \omega_{\lambda} \left(\frac{1}{2} + \hat{a}_{\lambda}^{\dagger} \hat{a}_{\lambda} \right) \quad (2.56)$$

Where λ represents the phonon modes with band index j and wave vector \mathbf{q} , \hbar is the reduced Planck constant, ω_{λ} is the harmonic frequency, and $\hat{a}_{\lambda}^{\dagger}$ and \hat{a}_{λ} are the phonon creation and annihilation operators. The harmonic Hamiltonian is also defined as the sum of the kinetic energy, K_E , and the 2-body crystal potential, H_2 :

$$H_H = K_E + H_2 \quad (2.57)$$

with

$$K_E = \frac{1}{2} \sum_{lka} m_k [\dot{u}_a(lk)]^2 \quad (2.58)$$

$$H_2 = \frac{1}{2} \sum_{lka} \sum_{l'k'b} \Phi_{ab}(lk, l'k') u_a(lk) u_b(l'k') \quad (2.59)$$

and the 3-body potential can be expressed as

$$H_3 = \frac{1}{6} \sum_{lka} \sum_{l'k'b} \sum_{l''k''c} \Phi_{abc}(lk, l'k', l''k'') \times u_a(lk) u_b(l'k') u_c(l''k'') \quad (2.60)$$

where $u(lk)$ is the displacement of atom k in unit cell l , m_k is the atomic mass of atom k , and a , b and c are the cartesian axes, and Φ_{ab} and Φ_{abc} are the second and third order force constants.

The three-body crystal potential can also be expressed as:

$$H_3 = \sum_{\lambda\lambda'\lambda''} \Phi_{\lambda\lambda'\lambda''} (\hat{a}_\lambda + \hat{a}_{-\lambda}^\dagger) (\hat{a}_{\lambda'} + \hat{a}_{-\lambda'}^\dagger) (\hat{a}_{\lambda''} + \hat{a}_{-\lambda''}^\dagger) \quad (2.61)$$

Where $\Phi_{\lambda\lambda'\lambda''}$ is the interaction strength between scattering phonons modes λ , λ' and λ'' , and λ correspond to the normal mode (\mathbf{q}, j) of a band index j and wave vector \mathbf{q} :

$$\begin{aligned} & \Phi_{\lambda\lambda'\lambda''} \\ &= \frac{1}{\sqrt{N}} \frac{1}{3!} \sum_{\kappa\kappa'\kappa''} \sum_{abc} W_a(\kappa, \lambda) W_b(\kappa', \lambda') W_c(\kappa'', \lambda'') \sqrt{\frac{\hbar}{2m_\kappa\omega_\lambda}} \sqrt{\frac{\hbar}{2m_{\kappa'}\omega_{\lambda'}}} \sqrt{\frac{\hbar}{2m_{\kappa''}\omega_{\lambda''}}} \\ & \times \sum_{l'l''} \Phi_{abc}(0\kappa, l'\kappa', l''\kappa'') e^{i\mathbf{q}' \cdot [\mathbf{r}(l'\kappa') - \mathbf{r}(0\kappa)]} e^{i\mathbf{q}'' \cdot [\mathbf{r}(l''\kappa'') - \mathbf{r}(0\kappa)]} e^{i(\mathbf{q} + \mathbf{q}' + \mathbf{q}'') \cdot \mathbf{r}(0\kappa)} \Delta(\mathbf{q} \\ & + \mathbf{q}' + \mathbf{q}'') \end{aligned} \quad (2.62)$$

With $W(\kappa, \lambda)$ representing the polarisation vector. From this, the imaginary part of the self-energy, $\Gamma_\lambda(\omega)$, can be calculated:

$$\begin{aligned} \Gamma_\lambda(\omega) &= \frac{18\pi}{\hbar^2} \sum_{\lambda'\lambda''} |\Phi_{-\lambda\lambda'\lambda''}|^2 \{ (n_{\lambda'} + n_{\lambda''} + 1) \delta(\omega \\ & - \omega_{\lambda'} - \omega_{\lambda''}) \\ & + (n_{\lambda'} + n_{\lambda''}) [\delta(\omega + \omega_{\lambda'} - \omega_{\lambda''}) \\ & - \delta(\omega - \omega_{\lambda'} + \omega_{\lambda''})] \} \end{aligned} \quad (2.63)$$

With n_λ corresponding to the phonon occupation number at equilibrium. The self-energy is related to the phonon linewidth as $2\Gamma_\lambda(\omega)$, and as such the phonon lifetime is defined as:

$$\tau_\lambda = \frac{1}{2\Gamma_\lambda(\omega_\lambda)} \quad (2.64)$$

The lattice thermal conductivity can be calculated using a single-mode relaxation time (SMRT) approximation or the direct solution to the linearised Boltzmann transport equation

(LBTE). The SMRT approximation is far less computationally demanding than LBTE, but generally provides good agreement with the LBTE method, as shown in Tables A.1 and A.2 in the Supplementary Data, and is therefore a suitable method for the calculation of lattice thermal conductivity. Under the SMRT approximation, the lattice thermal conductivity is:

$$\kappa_l = \frac{1}{NV_0} \sum_{\lambda} C_{\lambda} \mathbf{v}_{\lambda} \otimes \mathbf{v}_{\lambda} \tau_{\lambda} \quad (2.65)$$

where τ_{λ} is the relaxation time of phonon mode λ calculated with the SMRT approximation. The heat capacity is the property of a system defining the conversion of absorbed energy into a temperature increase, where the phonon mode heat capacity is the contribution to the total heat capacity from phonon mode λ , given by:

$$C_{\lambda} = k_B \left(\frac{\hbar\omega_{\lambda}}{k_B T} \right)^2 \frac{e^{\frac{\hbar\omega_{\lambda}}{k_B T}}}{\left[e^{\frac{\hbar\omega_{\lambda}}{k_B T}} - 1 \right]^2} \quad (2.66)$$

and \mathbf{v}_{λ} is the group velocity of phonon mode λ , the velocity of the phonon transversing the crystal lattice as a wave packet, given by:

$$\mathbf{v}_a(\lambda) = \frac{1}{2\omega_{\lambda}} \sum_{\kappa\kappa'bc} W_b(\kappa, \lambda) \frac{\partial D_{bc}(\kappa\kappa', \mathbf{q})}{\partial q_a} W_{\gamma}(\kappa', \lambda) \quad (2.67)$$

where V_0 is the unit cell volume and $W(\kappa, \lambda)$ is the polarisation vector and obtained through the dynamic matrix $D(\kappa\kappa', \mathbf{q})$.

The direct solution to the linearised Boltzmann equation can also be used for the determination of the lattice thermal conductivity.

$$\frac{\partial n_{qp}^{(1)}}{\partial t} + \frac{\partial n_{qp}^{(2)}}{\partial T} \frac{\partial T}{\partial \vec{r}} \cdot \vec{v}_{qp} = C(qp, n_{qp}^{(1)}) + \frac{1}{2} D(qp, n_{qp}^{(1)}) \quad (2.68)$$

Where $n_{qp}^{(0)}$ is the occupation function for a phonon of wave vector q in branch p at equilibrium, and $n_{qp}^{(1)}$ is the first order derivation from equilibrium, such $n_{qp} \approx n_{qp}^{(1)} + n_{qp}^{(0)}$. The scattering terms are expressed by the collision processes, $C(qp)$ and the decay processes, $D(qp)$, and \vec{v}_{qp} is the phonon velocity.

Whilst not explicitly used, another important parameter in the definition of the heat transport properties of a thermoelectric material is the Grüneisen parameter. This parameter describes the effect on the vibrational properties of a crystal lattice with changing volume. This is tied intrinsically to the effect of temperature on the phonon modes if a crystal, and can be defined as:

$$\gamma_G = \alpha \frac{K_T}{C_V \rho} \quad (2.69)$$

where α is the thermal expansion coefficient, K_T is the isothermal compressibility, C_V is the heat capacity at constant volume, and ρ is the density. Above the Debye temperature, the temperature at which the highest frequency mode is excited, the thermal conductivity is inversely proportional to the square of the Grüneisen parameter: ^[26]

$$\kappa \propto \frac{1}{\gamma_G^2} \quad (2.70)$$

2.2 - Methodology

2.2.1- Quantum Espresso

For the electronic characterisation, Quantum Espresso was used.^[27] Quantum Espresso is primarily a DFT based software utilising pseudopotentials and plane-wave basis sets for first-principles *ab-initio* electronic calculations. The software is modular and open-source, inviting third-party code creation and implementation, allowing for a wide variety of uses in structural and electronic calculation. The core module of Quantum Espresso is the PWscf (Plane-Wave self-consistent field) package, used for cell and geometry minimisation and electronic ground-state characterisation.

Relaxation

The cell parameters and atomic positions were relaxed using the PWscf (Plane-Wave Self-Consistent Field) package within Quantum Espresso. The SCF calculations were run on a k-grid of 3x8x8 (*Pnma*), 2x8x8 (2:2, 3:3, 1:2, 2:1, 1:3 and 3:1) and 9x9x9 (*Cmcm*) data points. Energy cutoff values of 70 Ry, for the wavefunction, and 560 Ry, for the charge density, were used. These values were optimised and suggested by the MaterialsCloud pseudopotential website.^[28] Each SCF step was converged such that the estimated energy error was below 1×10^{-8} Ry, and the full relaxation was continued until the difference between SCF cycles was less than 1×10^{-8} Ry for the total energy and 1×10^{-6} Ry/bohr for all the component forces on each atom, and such that the total cell pressure was within 1×10^{-9} Kbar of the target (1 atm or 1.01325 bar). The relaxations were also constrained to retain each cell's corresponding Bravais Lattice Index. The NSCF calculation used a larger Monkhorst-Pack k-grid size, with values of 4x11x10 (*Pnma*), 2x11x10 (2:2, 3:3, 1:2, 2:1, 1:3 and 3:1), and 12x12x12 (*Cmcm*).

2.2.2 - Wannier90 and Postw90

The electronic properties were examined through Wannier functions, the localised molecular orbital equivalent for crystal systems. The spread of the Wannier function is minimised to achieve the maximally localised Wannier function, which was then used to interpolate the band structure and perform electronic transport analysis

Wannier90

The Wannier90 package can restrict the calculation by selecting only specific orbitals for each atomic type, and as such only the p-orbitals of both Sn and S/Se were used for the

wannierisation as the orbitals further away from the Fermi level have sharply diminishing effects on the electronic properties whilst still requiring large computational resources. The minimisation of the spreads was obtained with a 1.0×10^{-10} convergence tolerance across 5 iterations, and a Monkhorst-Pack k-grid equivalent to the grid used in the NSCF calculations. The k-paths used for the band structure were obtained from the Materials Cloud SeeKPath tool^[29, 30] using the structures symmetry.

Postw90

The Postw90 package is used to calculate the electronic properties from the Wannier functions produced by Wannier90. A Monkhorst-Pack k-grid density of 500 points per Angstrom was used and the Fermi level set to midpoint between highest occupied and lowest unoccupied energy levels, with μ values ranging from Fermi energy -3 eV to +3 eV, in steps of 0.001 eV. The temperature range was set to 200 K to 900 K, in steps of 10 K. The relaxation time for the calculation was set to 1 fs. As the relaxation time acts as a multiplier on the electrical conductivity and K-coefficient values, a relaxation time of 1 fs allows the true relaxation time to be determined by multiplication of these values to fit to experimental calculations.

2.2.3 - CP2K

As with Quantum Espresso, CP2K is a modular and open-source suite of codes, with a variety of third-party methods available for use in the distribution package. One such method is the Geometry, Frequency, Noncovalent, eXtended TB (GFN-xTB),^[31] which was used in application of the tight-binding approach in this work. Whilst presented mainly in the context of protein and organic computation, this system is also suited to inorganic calculations. This method states a target system of around 1000 atoms, and successful application on systems of 3000 atoms, which suits its intended use in this work with atom counts reaching 3072 atoms for the largest systems.

The total energy used in the GFN-xTB method is defined as:

$$E = E_{el} + E_{rep} + E_{disp} + E_{XB} \quad (2.71)$$

and the electronic energy E_{el} is defined as:

$$\begin{aligned}
E_{el} = & \sum_i^{occ.} n_i \langle \psi_i | H_0 | \psi_i \rangle + \frac{1}{2} \sum_{A,B} \sum_{l(A)} \sum_{l'(B)} p_l^A p_{l'}^B \gamma_{AB, ll'} \\
& + \frac{1}{3} \sum_A \Gamma_A q_A^3 - T_{el} S_{el}
\end{aligned} \tag{2.72}$$

where H_0 is the zero order Hamiltonian, and ψ_i correspond to valence molecular orbitals of occupation number n_i . $T_{el} S_{el}$ is the electronic free energy and the self-consistent charge contributions are accounted for by the second and third terms, where q_A is the Mulliken charge of atom A , and Γ_A is the charge derivative of the atomic Hubbard parameter η_A . Finally, the second term is summed over shells l and l' on atoms A and B with p the charge distributed over those orbital shells.

Relaxation

The cell parameters and atomic positions were relaxed using the tight-binding xTB function within the CP2K package. The SCF parameters used were a Monkhorst-Pack k-grid of 6x8x8 on the *Pnma*-size unit cells and 4x8x8 on those larger than the *Pnma* unit cell, a dispersion radius of 0.7, and convergence accuracy of 1×10^{-9} .

The cell relaxation was calculated using the Broyden-Fletcher-Goldfarb-Shanno (BFGS)^[32, 33, 34, 35] scheme, and the limits used were 0.001 a_0 for the max geometric change and 0.0001 a_0 for the root mean squared of this change, 0.0001 $E_h a_0^{-1}$ for the max force and 0.001 $E_h a_0^{-1}$ for the max root mean squared for the force, and 0.001 bar for the pressure tolerance, with the orthorhombic symmetry fixed.

2.2.4 - Phono3py

Due to the lack of an official CP2K interface for Phono3py, a workaround using the QE interface was created. The structure, relaxed through the method above in CP2K, was written into a QE input file. This was used as the Phono3py input to create the perturbed supercells necessary for the thermal conductivity calculation. A script was created to take the atomic positions and cell parameters from the supercells to create CP2K SCF input files for each. These SCF inputs had far lower computational requirements than the QE equivalents, and as such could allow for far greater supercell sizes to be completed in far shorter time. The xTB atomic parameters for Sn and S/Se pull the orbitals tighter around the atomic centre than in plane-wave pseudopotential methods. As such, the atoms

themselves are pulled closer and held more tightly to each other than in other methods such as QE, and a finite displacement of atoms would result in a force upon the atom larger than expected by Phono3py. As such it was seen as important to proportionally weaken these forces in order to align the acoustic phonons to the appropriate levels. This weakening of forces lowered the frequencies of the phonon dispersion curves such that the acoustic phonon bands were closely matched between CP2K and literature phonon band. As these acoustic phonons are the larger contributors to the lattice thermal conductivity the alignment of these bands was seen as the most important indicator of an appropriate model. The forces obtained through this method were added to a pseudo-QE output, with flags that Phono3py maps to in order to allow the necessary post-processing.

Phonon Dispersion Spectra

The phonon dispersion spectra calculation uses the same k-path as for the electronic band structure. The calculation also uses a k-grid of 100, using the automatic k-point generation included in the Phonopy package such that:

$$N_{n^*} = \max[1, \text{nint}(l|n^*|)] \quad (2.73)$$

where N_{n^*} is the mesh number generated for the n coordinate (a, b, c) for an input value l , equal to 100 in this case.

For the path itself 1001 sampling points along each high-symmetry path were chosen.

Thermal Conductivity

The lattice thermal conductivity calculation requires multiple unit-cell supercell sizes, with second order interactions obtained through calculations on large supercells, and third order interactions calculated through a significantly larger number of individual displacements on a smaller grid. The *Pnma* structures used 3x3x3 and 4x8x8 third and second order supercell sizes, the double-layered structures used 2x3x3 and 3x6x6, the triple-layered structures used 1x3x3 and 2x4x4, and the *Cmcm* used 3x3x3 and 6x6x6. A selection of different supercell sizes and their 300 K lattice thermal conductivity values are shown in Table A.3 of the Supplementary Data.

For the larger unit cell structures, a cutoff pair-distance was used to minimise the number of third order force calculations necessary. This takes the form of a reduction of the number of individual calculations required by restricting the interaction distance to below a certain

cutoff value. In the generation of the individual force calculations, a list of pairs of interacting atoms is generated for third order interactions. When the distance between these pairs is above a specified threshold the supercell is not generated and the forces are assumed to be zero. This reduces the number of calculations required significantly, and as the long-range interactions are assumed to have a lower impact on the lattice phonon conductance this trade-off is generally a beneficial one. This value was evaluated individually for each calculation, but a distance encompassing less than 20% of the full number of supercells was generally deemed sufficient for all structures, and convergence curves are shown in Figures A.1-3 of the Supplementary Data. Sampling meshes were also evaluated individually for each system using convergence criteria and shown in Figures A.4-9 of the Supplementary Data.

References

- [1] D. S. Sholl and J. A. Steckel, *Density Functional Theory: A Practical Introduction*, John Wiley & Sons, 2009.
- [2] F. Jensen, *Introduction to Computational Chemistry*, Wiley, 2017.
- [3] S. Baroni, S. de Gironcoli, A. Dal Corso and P. Giannozzi, "Phonons and Related Crystal Properties from Density-Functional Perturbation Theory," *Reviews of Modern Physics*, vol. 73, no. 2, pp. 512-562, 2001.
- [4] E. Schrödinger, "An Undulatory Theory of the Mechanics of Atoms and Molecules," *Physical Review*, vol. 28, no. 6, pp. 1049-1070, 1926.
- [5] D. R. Hartree, "The Wave Mechanics of and Atom with a Non-Coulomb Central Field, Part II," *Mathematical Proceedings of the Cambridge Philosophical Society*, vol. 24, no. 01, p. 111, 1928.
- [6] V. Fock, "Näherungsmethode zur Lösung des quantenmechanischen Mehrkörperproblems," *Zeitschrift für Physik*, vol. 61, pp. 126-148, 1930.
- [7] P. Hohenberg and W. Kohn, "Inhomogeneous Electron Gas," *Physical Review B*, vol. 136, no. 3B, pp. B864-B871, 1964.
- [8] W. Kohn and L. J. Sham, "Self-Consistent Equations Including Exchange and Correlation Effects," *Physical Review*, vol. 140, no. 4A, pp. A1133-A1138, 1965.
- [9] A. D. Becke, "Density-Functional Exchange-Energy Approximation with Correct Asymptotic Behavior," *Physical Review A*, vol. 38, no. 6, pp. 3098-3100, 1988.
- [10] C. Lee, W. Yang and R. G. Parr, "Development of the Colle-Salvetti Correlation-Energy Formula into a Functional of the Electron Density," *Physical Review B*, vol. 37, no. 2, pp. 785-789, 1988.
- [11] S. H. Vosko, L. Wilk and M. Nusair, "Accurate Spin-Dependent Electron Liquid Correlation Energies for Local Spin Density Calculations: A Critical Analysis," *Canadian Journal of Physics*, vol. 58, no. 8, pp. 1200-1211, 1980.
- [12] N. W. Ashcroft and N. D. Mermin, "Electron Levels in a Periodic Potential: General Properties," in *Solid State Physics*, Philadelphia, Saunders College Publishing, 1976.
- [13] H. Hellman, "A New Approximation Method in the Problem of Many Electrons," *The Journal of Chemical Physics*, vol. 3, no. 1, p. 61, 1935.
- [14] D. Hamann, M. Schlüter and C. Chiang, "Norm-Conserving Pseudopotentials," *Physical Review Letters*, vol. 43, no. 20, pp. 1494-1497, 1979.
- [15] D. Vanderbilt, "Soft self-consistent Pseudopotentials in a Generalized Eigenvalue Formalism," *Physical Review B*, vol. 41, no. 11, pp. 7892-7895, 1990.
- [16] B. N. Finkelstein and G. E. Horowitz, "Über die Energie des He-Atoms und des Positiven H²-Ions im Normalzustande," *Zeitschrift Für Physik*, vol. 48, no. 1-2, pp. 118-122, 1928.
- [17] F. Bloch, "Über die Quantenmechanik der Elektronen in Kristallgittern," *Zeitschrift Für Physik*, vol. 52, no. 7-8, pp. 555-600, 1929.
- [18] J. C. Slater and G. F. Koster, "Simplified LCAO Method for the Periodic Potential Problem," *Physical Review*, vol. 94, no. 6, pp. 1498-1524, 1954.
- [19] G. Pizzi, V. Vitale, R. Arita, S. Blügel, F. Freimuth, G. Géranton, M. Gibertini, D. Gresch, C. Johnson, T. Koretsune, J. Ibañez-Azpiroz, H. Lee, J. M. Lihm, D. Marchand, A. Marrazzo, Y. Mokrousov, J. I. Mustafa, Y. Nohara, Y. Nomura, L. Paulatto, S. Poncé, T. Ponweiser, J. Qiao, F. Thöle, S. S. Tsirkin, M. Wierzbowska, N. Marzari, D. Vanderbilt, I. Souza, A. A. Mostofi and J. R Yates, "Wannier90 as a Community Code: New Features and Applications," *Journal of Physics: Condensed Matter*, vol. 32, p. 165902, 2020.

- [20] G. H. Wannier, "The Structure of Electronic Excitation Levels in Insulating Crystals," *Physical Review*, vol. 52, no. 3, pp. 191-197, 1937.
- [21] G. Pizzi, D. Volja, B. Kozinsky, M. Fornari and N. Marzari, "BoltzWann: A Code for the Evaluation of Thermoelectric and Electronic Transport Properties with a Maximally-Localised Wannier Functions Basis," *Computer Physics Communications*, vol. 185, no. 1, pp. 442-429, 2014.
- [22] T. Scheidemantel, C. Ambrosch-Draxl, T. Thonhauser, J. V. Badding and J. O. Sofo, "Transport Coefficients from First-Principles Calculations," *Physical Review B*, vol. 68, no. 12, pp. 125210-125216, 2003.
- [23] R. P. Feynman, "Forces in Molecules," *Physical Review*, vol. 56, pp. 340-343, 1939.
- [24] A. Togo and I. Tanaka, "First Principles Phonon Calculations in Materials Science," *Scripta Materialia*, vol. 108, pp. 1-5, 2015.
- [25] A. Togo, L. Chaput and I. Tanaka, "Distributions of Phonon Lifetimes in Brillouin Zones," *Physical Review B*, vol. 91, no. 9, 2015.
- [26] J. M. Ziman, "Transport Properties," in *Principles of the Theory of Solids*, Cambridge University Press, 1972, p. 240.
- [27] P. Giannozzi, S. Baroni, N. Bonini, M. Calandra, R. Car, C. Cavazzoni, D. Ceresoli, G. L. Chiarotti, M. Cococcioni, I. Dabo, A. Dal Corso, S. de Gironcoli, S. Fabris, G. Fratesi, R. Gebauer, U. Gerstmann, C. Gougoussis, A. Kokalj, M. Lazzeri, L. Martin-Samos, N. Marzari, F. Mauri, R. Mazzarello, S. Paolini, A. Pasquarello, L. Paulatto, C. Sbraccia, S. Scandalo, G. Sclauzero, A. P. Seitsonen, A. Smogunov, P. Umari and R. M. Wentzcovitch, "QUANTUM ESPRESSO: A Modular and Open-Source Software Project for Quantum Simulations of Materials," *Journal of Physics: Condensed Matter*, vol. 21, no. 39, p. 395502, 2009.
- [28] G. Prandini, A. Marrazzo, I. E. Castelli, N. Mounet, E. Passaro and N. Marzari, "A Standard Solid State Pseudopotentials (SSSP) Library Optimised for Precision and Efficiency," *Materials Cloud Archive 2021.76*, 2021.
- [29] Y. Hinuma, G. Pizzi, Y. Kumagai, F. Oba and I. Tanaka, "Band Structure Diagram Paths Based on Crystallography," *Computational Materials Science*, vol. 128, pp. 140-184, 2017.
- [30] A. Togo and I. Tanaka, "Spglib: A Software Library for Crystal Symmetry Search," 2018.
- [31] S. Grimme, C. Bannwarth and P. Shushkov, "A Robust and Accurate Tight-Binding Quantum Mechanical Method for Structures, Vibrational Frequencies, and Noncovalent Interactions of Large Molecular Systems Parameterized for All spd-Block Elements (Z=1-86)," *Journal of Chemical Theory and Computation*, vol. 13, no. 5, pp. 1989-2009, 2017.
- [32] C. G. Broyden, "The Convergence of a Class of Double-rank Minimization Algorithms 1. General Considerations," *IMA Journal of Applied Mathematics*, vol. 6, no. 1, pp. 76-90, 1970.
- [33] R. Fletcher, "A New Approach to Variable Metric Algorithms," *The Computer Journal*, vol. 13, no. 3, pp. 317-322, 1970.
- [34] D. Goldfarb, "A Family of Variable-Metric Methods Derived by Variational Means," *Mathematics of Computation*, vol. 24, pp. 23-26, 1970.
- [35] D. F. Shanno, "Conditioning of Quasi-Newton Methods for Function Minimization," *Mathematics of Computation*, vol. 24, pp. 647-656, 1970.

Chapter 3:

Tin Chalcogenides

With lead chalcogenides firmly established in literature as strong thermoelectric materials, ^[1, 2, 3] the tin chalcogenides were introduced as suitable candidates exhibiting a lower toxicity than the Pb-based counterparts. With a small band gap, high carrier mobility, large Seebeck coefficient and an extremely low lattice thermal conductivity, SnSe has been the focus of many bodies of work in the search for high figure of merit materials to use as an aid to energy production and scavenging. ^[4] The distorted NaCl geometry gives rise to layered sheets, with much the same structure as exhibited in black phosphorous. An elongated c-axis creates a zig-zag motif with a less rigid structure than the b-axis, leading to a slightly lower thermal conductivity and producing the $a < c < b$ axial thermal conductivity ordering. At high temperatures, the *Pnma*-SnS and SnSe undergo a phase transition to the *Cmcm* symmetry, in which the c-axis shortens to more closely resemble the b-axis.

The layered structure of SnSe and its counterpart, SnS, give rise to interesting possibilities for utilising structural boundaries as a means to disrupt the heat transport through phonon scattering, and further increase the already impressive figure of merit. This chapter focuses on the characterisation of the *Pnma* phases of these two materials with the aim to exploit the pre-existing layering boundaries in phonon scattering. This chapter will also introduce the high temperature *Cmcm* phase of SnS, calculated at low temperatures, as a means of understanding the structural impacts on the thermoelectric properties. The fundamental objective is to set a strong and effective baseline through which to compare the interlayered theoretical structures.

3.1 - SnS and SnSe

3.11 - Electronic Properties

Characterisation

The SnS and SnSe relaxed structure retained the GeS-type structure (B16, SG *Pnma*), a distorted NaCl (B1) structure. Their crystal structures were relaxed with Quantum Espresso using a GGA-PBE exchange-correlation functional. SnS showed relaxed lattice parameters $a = 11.4455 \text{ \AA}$, $b = 4.0240 \text{ \AA}$, $c = 4.4481 \text{ \AA}$, which are comparable with experimental literature parameters $a = 11.200 \text{ \AA}$, $b = 3.987 \text{ \AA}$ and $c = 4.334 \text{ \AA}$,^[5] and previous plane-wave

GGA calculated values of $a = 11.433 \text{ \AA}$, $b = 4.024 \text{ \AA}$ and $c = 4.443 \text{ \AA}$,^[6] highlighting the retained axial ratios, $b_{\text{calc}}/a_{\text{calc}} = 0.35$ and $b_{\text{exp}}/a_{\text{exp}}=0.36$, $c_{\text{calc}}/a_{\text{calc}} = 0.39$ and $c_{\text{exp}}/a_{\text{exp}} = 0.39$. SnSe showed relaxed lattice parameters $a = 11.7834 \text{ \AA}$, $b = 4.2054 \text{ \AA}$, $c = 4.5638 \text{ \AA}$, which are comparable with experimental literature parameters $a = 11.501 \text{ \AA}$, $b = 4.153 \text{ \AA}$ and $c = 4.445 \text{ \AA}$,^[5] and previous GGA calculated values of $a = 11.790 \text{ \AA}$, $b = 4.219 \text{ \AA}$ and $c = 4.524 \text{ \AA}$,^[7] with axial ratios, $b_{\text{calc}}/a_{\text{calc}} = 0.36$ and $b_{\text{exp}}/a_{\text{exp}}=0.36$, $c_{\text{calc}}/a_{\text{calc}} = 0.39$ and $c_{\text{exp}}/a_{\text{exp}} = 0.39$.

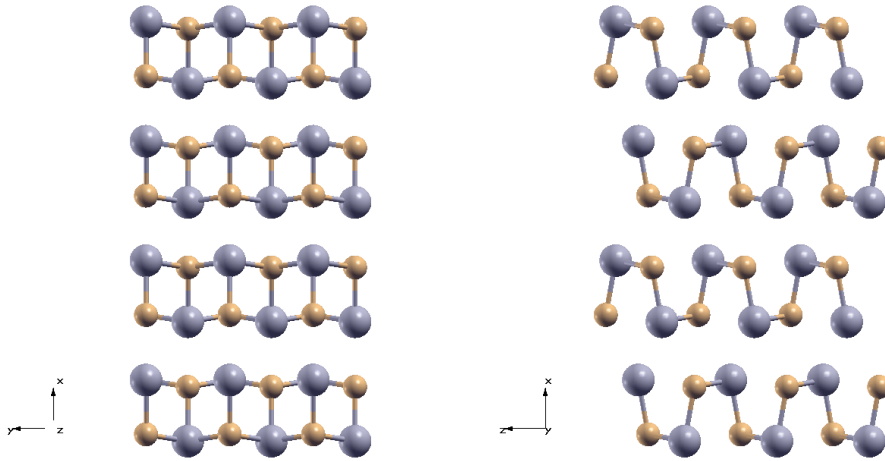


Figure 3.1: Pnma structure of SnS showing the layered motif along the a direction (x -axis) and the asymmetry along b and c directions (y and z axes).

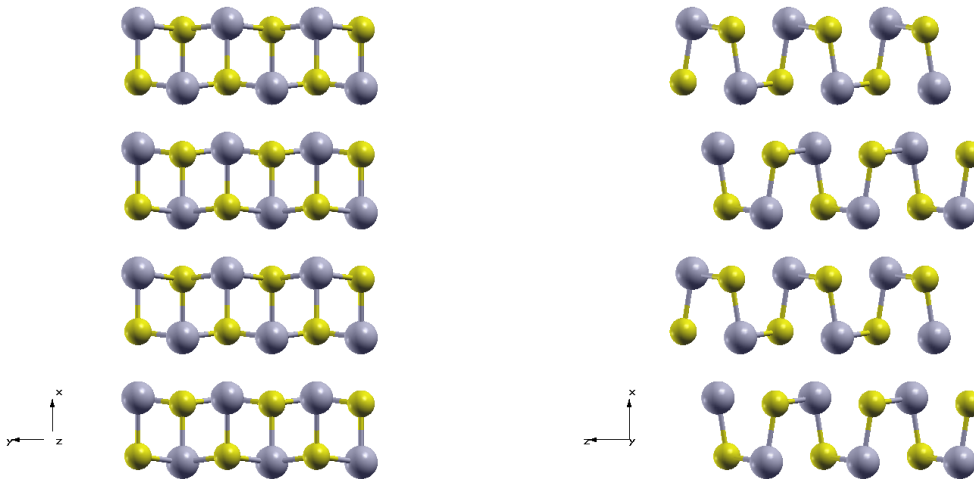


Figure 3.2: Pnma structure of SnSe showing the layered motif along the a direction (x -axis) and the asymmetry along b and c directions (y and z axes).

The electronic band structure of SnS and SnSe (Fig. 3.3) show characteristic agreement to established literature band structures. The $Y-\Gamma-Z$ path show two maxima in the highest valence band which share k -point positions with two minima in the lowest conduction band, connecting the two regions in an “opened Dirac cone”.

The direct band gap for SnS is 1.08 eV, falling in the Y- Γ path, and the indirect band gap is 0.95 eV. This is comparable to the literature value of 1.07 eV^[8], as well as computational literature values of 1.1 eV for the direct and 0.86 eV for the indirect band gaps^[9]. SnSe has a calculated direct band gap of 0.86 eV and an indirect of 0.61 eV, which has been shown to be valid in previous GGA bulk calculations, with a 0.98 eV direct gap and a 0.582 eV indirect gap^[9].

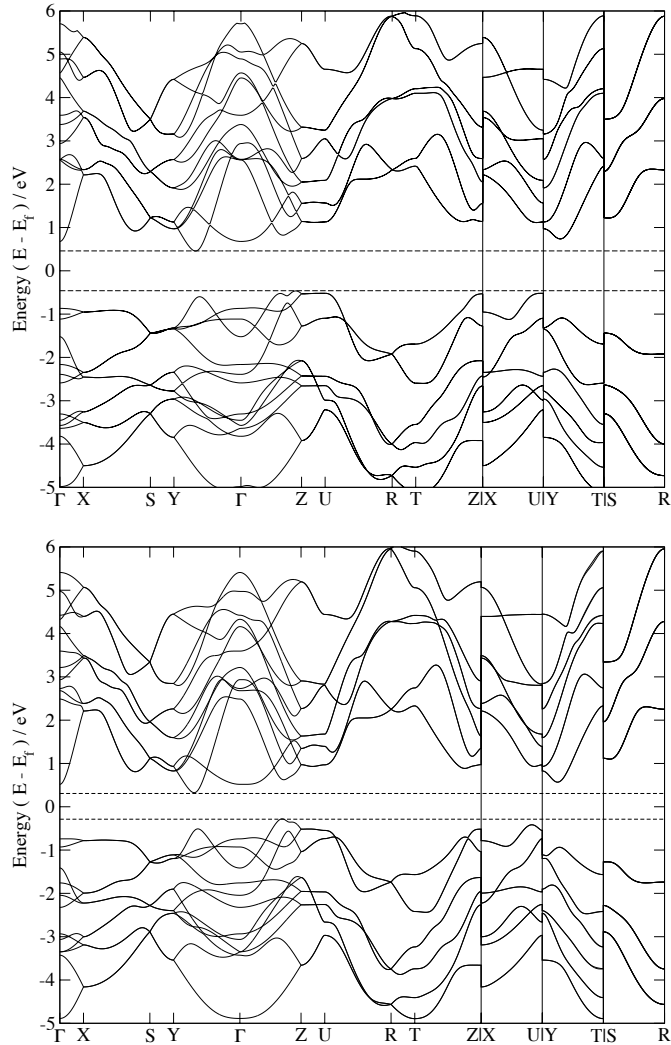


Figure 3.3: SnS (above) and SnSe (below) electronic band structures calculated with Wannier90

BoltzWann

The Seebeck tensor and the electronic conductivity tensor were calculated from the BoltzWann module of Wannier90 using the semiclassical Boltzmann transport equation, where the interpolated band velocities were used to evaluate the transport distribution

functions. These two data sets were used to calibrate the relaxation time for SnS at 300 K by the mapping of the Seebeck, which is unaffected by the relaxation time, to determine the equivalent chemical potential, μ . At 300 K, the Seebeck values 729 and 682 $\mu\text{V/K}$ for the y and z axes were chosen as the best match to the chosen experimental values of 704 and 709 $\mu\text{V/K}$ ^[10], with the calculated values showing greater anisotropy than the experimental. This alignment gave $\mu = -0.3123$, allowing the electronic conductivity to be compared to the experimental data to obtain a relaxation time of $\tau = 24.9394$ fs, with calculated electronic conductivity values of 2.76 and 1.62 S/cm matching experimental values of 2.26 and 1.95 S/cm^[10]. The same methodology gave Seebeck values of 533 and 482 $\mu\text{V/K}$ for the SnSe y and z directions at $\mu = -0.2224$, comparable to literature values of 505 and 512 $\mu\text{V/K}$ ^[11], and electronic conductivities of 9.98 and 13.2 S/cm along the y and z directions at a relaxation time of $\tau = 20.1182$ fs, which closely match experimental value of 10.52 and 12.47 S/cm for y and z^[11]. These relaxation times, and the relaxation times of the higher temperature calculations, match well with previous work, taken along a range 27 to 4 fs from 300 to 750 K^[12].

The peak Seebeck values of *Pnma*-SnS at 300 K were 1559, 1555 and 1508 $\mu\text{V/K}$ along the a, b and c axes in the *p*-doping region, and -1539, -1465 and -1466 $\mu\text{V/K}$ in the *n*-doping region. For *Pnma*-SnSe, the Seebeck peak maxima were 1023, 1062 and 1029 $\mu\text{V/K}$ along the a, b and c axes in the *p*-doping region, and -1022, -992 and -979 $\mu\text{V/K}$ in the *n*-doping region. The electrical conductivity values at the minima within the *Pnma*-SnS band gap were 3, 16 and 13 $\mu\text{S/cm}$, whereas the electrical conductivity minima of *Pnma*-SnSe were 1349, 3450 and 3773 $\mu\text{S/cm}$. Whilst SnSe shows lower Seebeck coefficient peak maxima, it benefits from a greatly increased near-Fermi-level electrical conductivity, over 100 times larger than that of *Pnma*-SnS, which at least in part explains the strong thermoelectric suitability of this material seen in experimental measurements. With regards to the electrical conductivity maximum values, it should be noted that whilst the two systems reach similar plateaus, the thermoelectric figure of merit is dependent on the square of Seebeck, and as such the lowered Seebeck coefficients seen farther from the Fermi-level would significantly hamper the efficiency before reaching a point of equal electrical conductivity between the two materials.

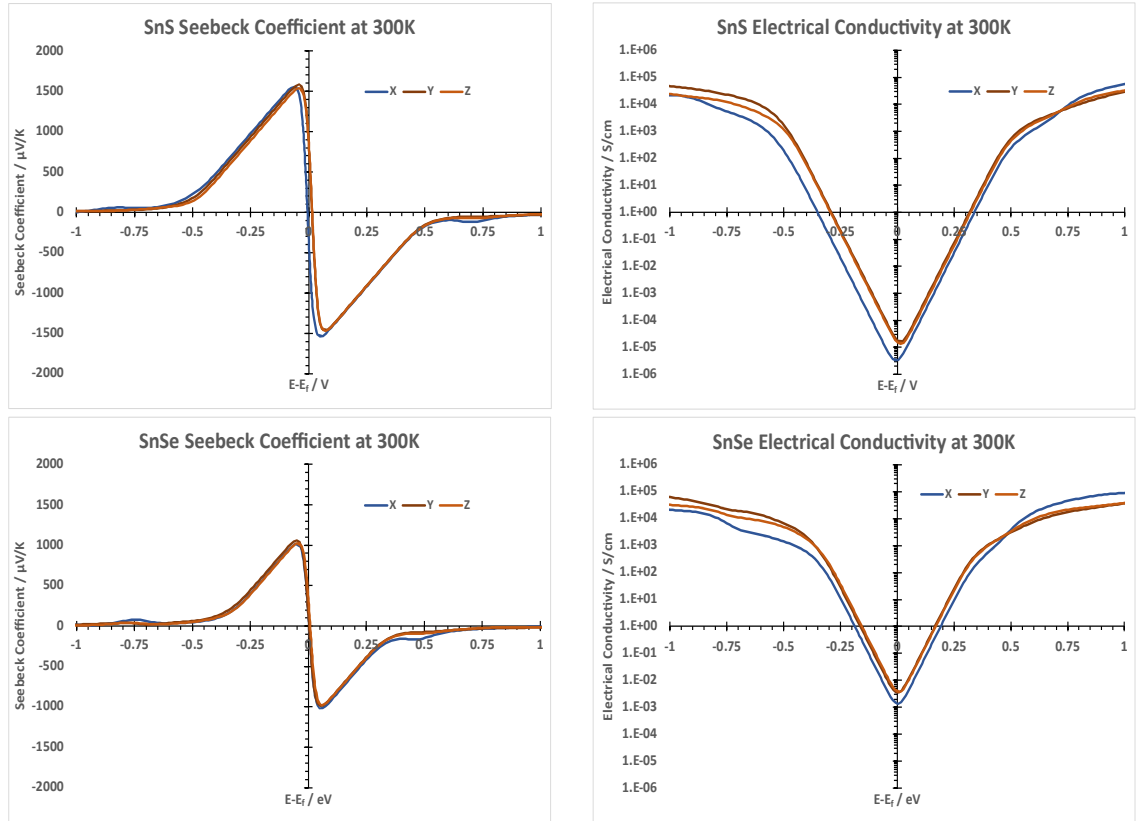


Figure 3.4: SnS (above) and SnSe (below) Seebeck Coefficient and Electrical Conductivity across μ values ± 1 eV from the Fermi level at 300 K.

3.1.2 - Phononic Properties

Characterisation

Using the xTB methodology within CP2K, the relaxed structures also retained the GeS-type structure, with SnS lattice parameters $a = 10.4111 \text{ \AA}$, $b = 3.7127 \text{ \AA}$, $c = 3.8204 \text{ \AA}$, and SnSe lattice parameters of $a = 10.7111 \text{ \AA}$, $b = 3.9015 \text{ \AA}$, $c = 3.9562 \text{ \AA}$. These are distinct from the literature cell lengths of $a = 11.200 \text{ \AA}$, $b = 3.987 \text{ \AA}$ and $c = 4.334 \text{ \AA}$ ^[5] for SnS and $a = 11.501 \text{ \AA}$, $b = 4.153 \text{ \AA}$ and $c = 4.445 \text{ \AA}$ ^[5] for SnSe, with the xTB parameters pulling the atoms tighter and lowering the cell lengths.

Phonon Spectral Analysis

As was mentioned above, the parameters given by the xTB method are particularly tight, and therefore produce strong forces constants between the Sn/S/Se atoms. This in turn pulls these atoms tighter to each other in bonding, and so a finite distance displacement will have a higher proportional pull back to the minima, exhibited as greater forces acting upon the displaced atoms.

When these forces are evaluated by Phono3py in the force constants Φ_{ab} and Φ_{abc} , a much more rigid material is seen than should be, and the lattice thermal conductivities are overexaggerated. With this in mind, there are two avenues of approach in remedying this misattribution. The first is applying a scaling factor to the resultant thermal conductivities to bring them in line with the experimentally recorded values. This approach is least desirable as it is the least robust and the evaluation of phonon bands, phonon lifetimes, and mean free paths would not be possible. The second approach, and the one used for this work, is a rescaling of the forces prior to the calculation of the force constants. However, without a clear value for the degree to which the forces are enhanced in the xTB method this approach requires parameterisation. For this, two phonon band structures were obtained for *Pnma*-SnS, one using a 2x4x4 supercell and Quantum Espresso as the force calculator, and one using a 4x8x8 supercell and CP2K as the force calculator. These are shown below in Fig. 3.5, and whilst showing strong similarities it is noticeable that the CP2K forces lead to a much higher frequency than expected with QE or other literature phonon spectra, calculated with the VASP code, using PAW pseudopotentials and PBE and PBEsol functionals [13, 14].

From these spectra it was decided to approach the force correction by alignment with the acoustic band along the reciprocal cartesian directions Γ -X, Γ -Y, and Γ -Z. These paths were chosen as they show clear characteristics in the linear increases out from the central gamma point, and the focus on the acoustic band specifically was chosen as the contribution to the lattice thermal conductivity is significantly higher for low-frequency acoustic phonons than the higher optical ones [15, 16]. All xTB force calculations hereafter can therefore be assumed to have had a scaling applied, equal to x0.25 of the calculated forces.

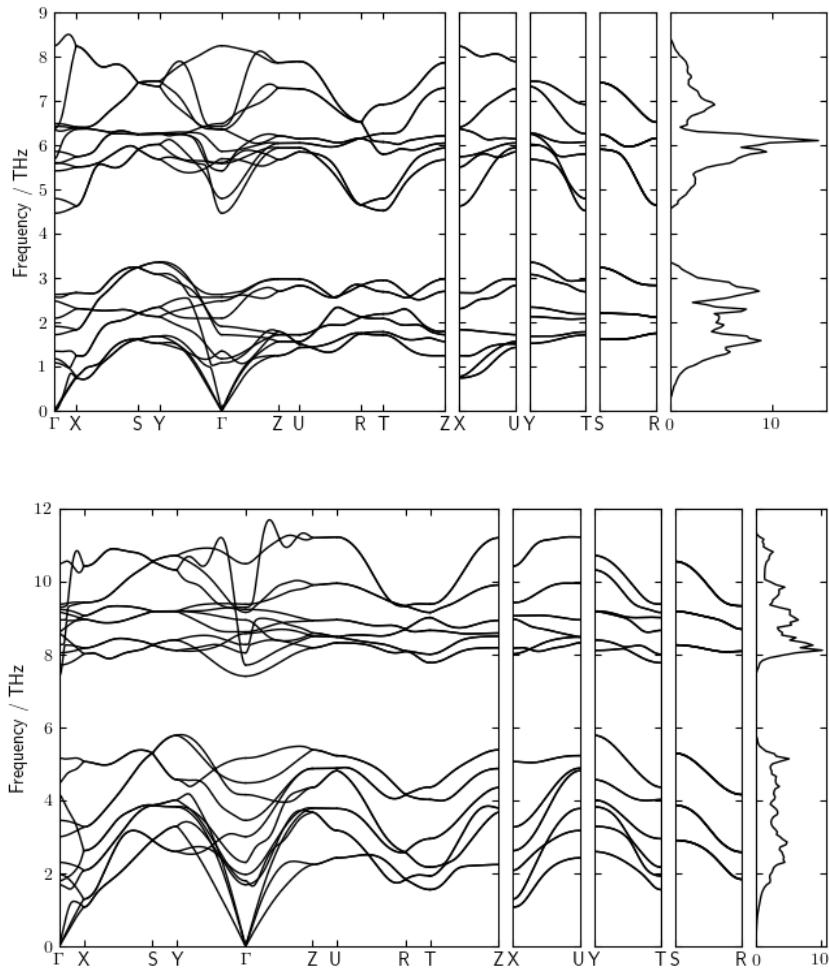


Figure 3.5: Phonon dispersion spectra with Quantum Espresso as force calculator (above), and CP2K as force calculator (below)

The resultant phonon spectra produced on a $4 \times 8 \times 8$ supercell size and using CP2K as the force calculator with uniformly scaled final forces are shown below in Fig. 3.6, with the SnSe phonon spectrum produced with the same method. The phonon dispersion spectra for both the CP2K and QE compare well, including the linear dispersion of phonon bands along the Γ -X, Γ -Y and Γ -Z paths, corresponding to the a, b and c axes respectively. In SnS, the lowest frequency points at the cartesian direction maxima are 0.5371 1.2986 and 1.1204 THz at points [0.5 0.0 0.0], [0.0 0.5 0.0], and [0.0 0.0 0.5], the X, Y and Z directions.

In SnSe these points show lower frequencies, with low band frequencies of 0.4243, 0.8428 and 0.7681 THz. The lowering of these phonon frequencies is key to the lower lattice thermal conductivity exhibited by *Pnma*-SnSe as the softer phonon frequencies lower the

phonon velocities, and therefore the efficiency of the heat transport across the lattice. The SnSe structure also shows a phonon band gap closure, attributed to a smaller cation/anion mass ratio compared to Sn. Whilst SnSe phonon band gap closure has been calculated in previous works^[17,18], it is not usually to the degree shown in this spectrum. This could be explained by a better model of the strong anharmonicity present in SnSe when viewed through this approach, as previous calculations tend to overestimate the lattice thermal conductivity when compared to literature values (0.52, 1.88 and 1.43 W/m/K^[17] for the a, b and c axes using PBEsol functional and PAW pseudopotentials via the VASP code, compared to literature values of 0.46, 0.70 and 0.68 W/m/K^[19]).

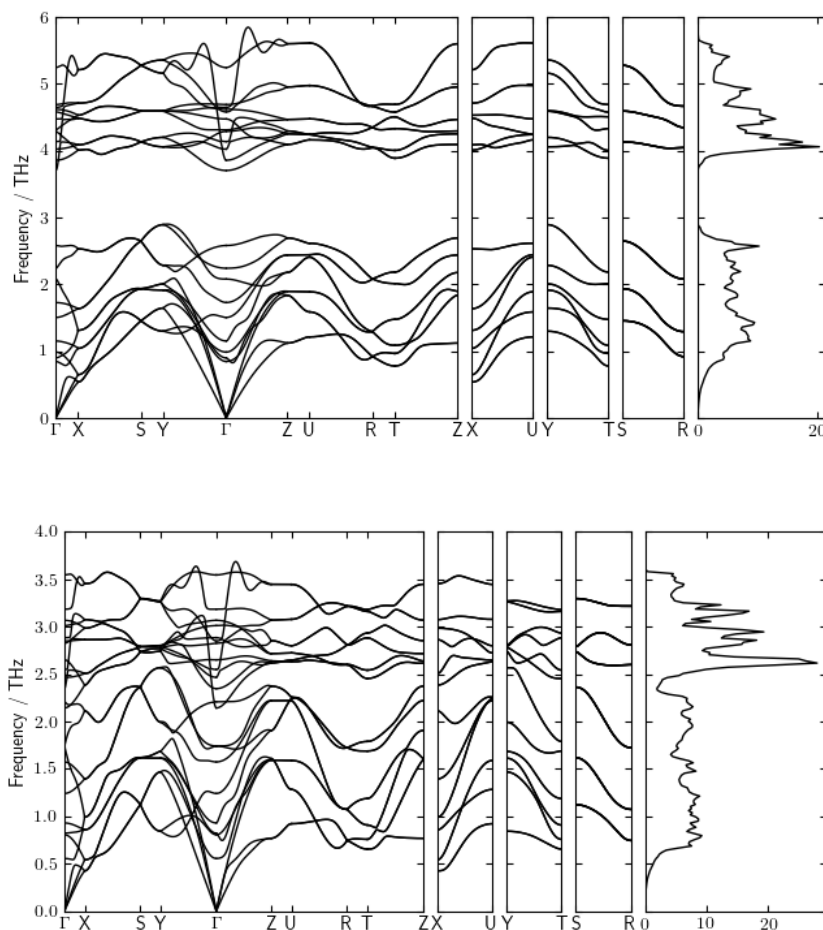


Figure 3.6: Phonon dispersion spectra of SnS (above) and SnSe (below), given in THz, calculated through Phonopy using CP2K/xTB for force calculation, with a 4x8x8 supercell size.

Thermal Conductivity

For the calculation of the lattice thermal conductivity, supercells were created to better examine the long-range properties of the phonon transport. For the third order interactions, a supercell size of 3x3x3 unit cells was chosen. The second order interactions are understood to be of longer range than the third order and require fewer finite displacement supercells to be calculated, and therefore a larger supercell was used to evaluate these interactions separately from the third order, with a supercell size of 4x8x8 unit cells.

The lattice thermal conductivity values of *Pnma*-SnS obtained through this method at 300 K were 0.7568, 1.8063 and 1.5776 W/m/K for the a, b and c axes respectively, with an averaged isotropic lattice thermal conductivity of 1.3802 W/m/K. This is in good agreement with literature values of 1.25^[20] and 1.4 W/m/K^[21]. The anisotropy shown in these values correlates with the anisotropy of the structure itself and correspond to the softness of the acoustic modes along the Γ -X, Γ -Y, Γ -Z paths, with the increasing softness ($Y < Z < X$) corresponding to a decreasing lattice thermal conductivity ($\kappa_b > \kappa_c > \kappa_a$). The dependency of the lattice thermal conductivities on temperature is shown in Fig. 3.7, and this dependency in κ_b and κ_c is greater than that of κ_a owing to the layers structural softness, however all axes show decrease at higher temperatures and κ_a is lowered to <0.3 W/m/K at 800 K.

The *Pnma*-SnSe calculations produced lattice thermal conductivity values of 0.3374, 0.7726 and 0.5652 W/m/K at 300K in the a, b and c axes. The axial ordering is the same as for SnS, however with a greater degree of anisotropy from a more significantly lowered κ_c . These values at 300 K show strong agreement with experimental values of 0.46, 0.70 and 0.68 W/m/K along the a, b and c axes, as well as showing a similar decrease to <0.2 W/m/K at high temperatures^[19].

The lattice thermal conductivity temperature dependence shows good general agreement with the experimental data, with a slight increase in low temperature b-axis values in *Pnma*-SnS, and a slight decrease in the a-axis values at higher temperatures. SnSe also sees slightly lower a- and b-axis values, and both SnS and SnSe show a larger degree of b/c anisotropy than the experimental data suggests. The generally better agreement from this method compared to previous computational literature calculations of the SnS and SnSe lattice thermal conductivities is also notable and indicates that whilst the force constants produced are stiffer than expected, the vibrational structure is better represented using the xTB parameters.

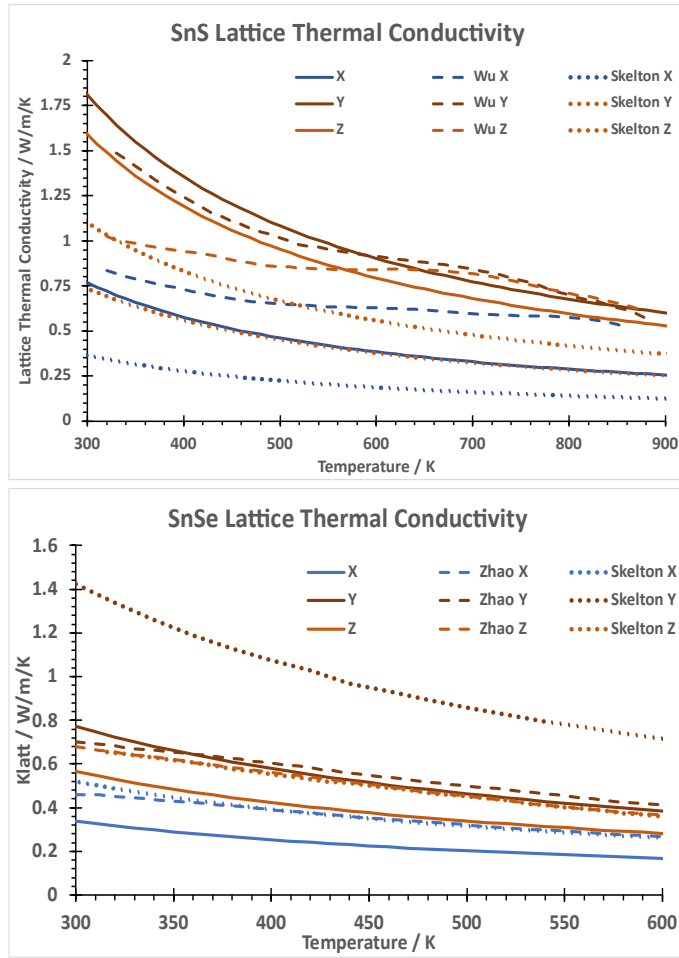


Figure 3.7: Lattice thermal conductivity, κ_{latt} , along the a, b and c axes as a function of temperature for SnS (above) and SnSe (below). Also shown are experimental curves, Wu-[22] and Zhao-[19], as well as previous computational literature curves, Skelton-[14, 17].

Phonon Frequency

With the lattice thermal conductivities obtained, an evaluation as to the reasons for the lower values in SnSe than in SnS was undertaken. The contributions to the lattice thermal conductivity across the frequency range were calculated and are shown in Fig. 3.8. These plots highlight the importance of the lower frequency acoustic phonons in heat transport in both SnS and SnSe, most significantly in the Y-direction, where the low frequency maxima of each (1 and 2 THz at 1.1 W/m/K in SnS and 2 THz at 0.6 W/m/K in SnSe) amounting to approximately 6 times the high frequency maxima (5 THz at 0.2 W/m/K in SnS and 3 THz at 0.1 W/m/K in SnSe). This effect is less pronounced along the layering X-direction, but is

still substantial, with contribution values approximately 4 times larger across the 0-2 THz range when compared to those of higher frequencies.

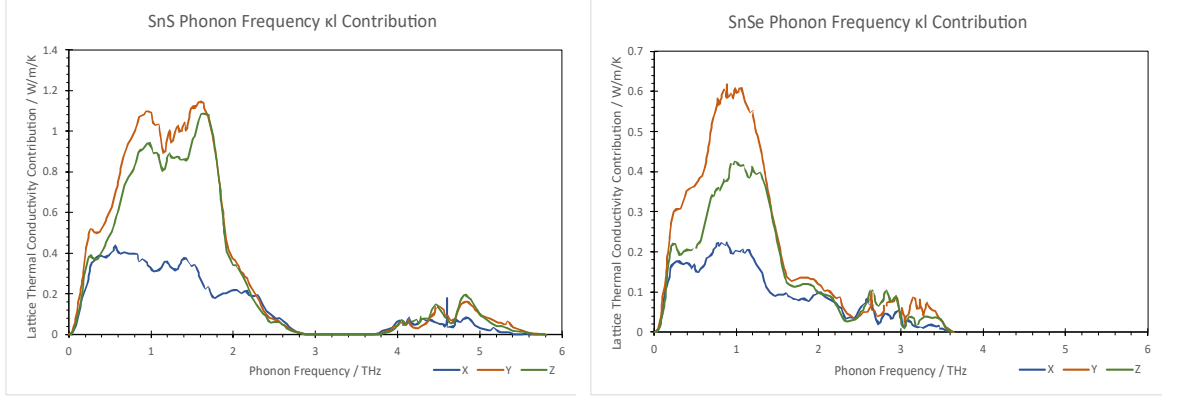


Figure 3.8: Contributions to the lattice thermal conductivity by phonon frequency for SnS (left) and SnSe (right)

Phonon Lifetimes

Both the phonon lifetime and the phonon mean free paths are directly interrelated with the lattice thermal conductivity, as shown in Equations 1.11 and 1.13. The lattice thermal conductivity is given by the sum over all phonon modes of the tensor products of the heat capacity and phonon velocity and the phonon velocity and relaxation time (lifetime) for each mode, divided by the total volume of the supercell. This relates to the mean free path of the phonon mode, l_λ , through the relationship:

$$l_\lambda = v_\lambda \tau_\lambda \quad (3.1)$$

The phonon lifetimes were calculated as a function of the phonon frequencies to better understand the reason for the low lattice thermal conductivities in SnSe compared to SnS. As the lower frequency phonons are the main heat conducting phonons, longer lifetimes at low frequencies will have a large impact on the material's lattice thermal conductivity. SnSe shows a flatter curve in its higher frequency range than SnS, with the peak at just below 3 THz barely rising above the rest of the nearby phonons, whereas SnS shows a large increase in phonon lifetime at just below 5 THz. However more relevant is the shallower slope of the lifetimes below 2 THz in SnSe, with the majority of the phonon lifetimes below 2.5 ps. SnS shows an extra peak at 2 THz, where the phonons average between 2.5 and 5

ps, and a further increase in phonon lifetimes at frequencies below 2 THz. The compact nature of the SnSe phonon lifetimes across the frequency range give a strong explanation for the decrease in thermal conductivity.

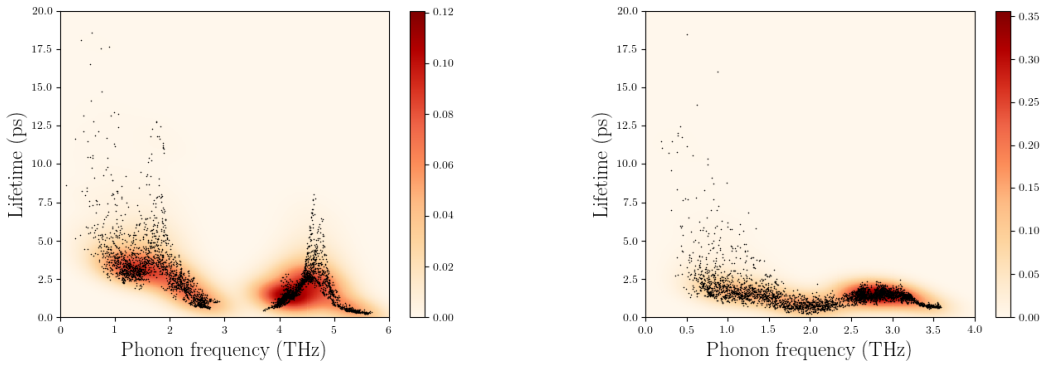


Figure 3.9: The lifetimes of phonons of varying frequencies for SnS (left) and SnSe (right). The heatmap indicating regions with a greater concentration of phonon modes.

Phonon Mean Free Paths

An alternate view on this can be given by contribution to the lattice thermal conductivity by mean free path, Fig. 3.10. This shows the contributions of higher mean free path phonon modes is far less in SnSe than in SnS. This is partially explained by the mass effect, where the heavier selenium disrupts the long-range phonons to a greater extent than the lighter sulphur, limiting heat transport to shorter paths and lower overall effectiveness, but is also an effect of differing vibrational modes accessible to the SnSe structure.

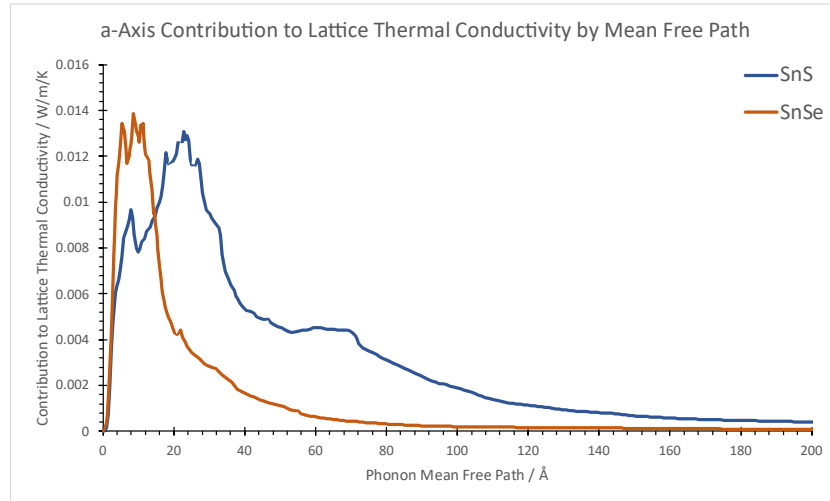


Figure 3.10: The phonon contributions to the lattice thermal conductivity at 300 K by phonon mean free path.

3.1.3 - Full Figure of Merit

With the Seebeck coefficient, S , electrical conductivity, σ , and electronic thermal conductivity, κ_e , calculated through the semiclassical Boltzmann transport equation via BoltzWann, and with the lattice thermal conductivity calculated through Phono3py, the electronic and lattice aspects of the thermoelectric figure of merit can be combined to give an indication as to the overall efficiency of these materials in a thermoelectric device.

At 300 K

The relaxation times at 300 K, $\tau = 24.9394$ fs for SnS and $\tau = 20.1182$ fs for SnSe, are calculated from alignment with experimental data. The electronic values show large anisotropy, with the b axis (y direction) showing more p -type nature and the a axis (x direction) showing more n -type nature. In SnS these two are fairly balanced, whereas in SnSe, whilst the p -type gives a similar figure of merit to SnS, the n -type improves greatly. The SnS and SnSe plots show similarities, but the smaller band gap and lower lattice thermal conductivity give rise to higher peaks for SnSe.

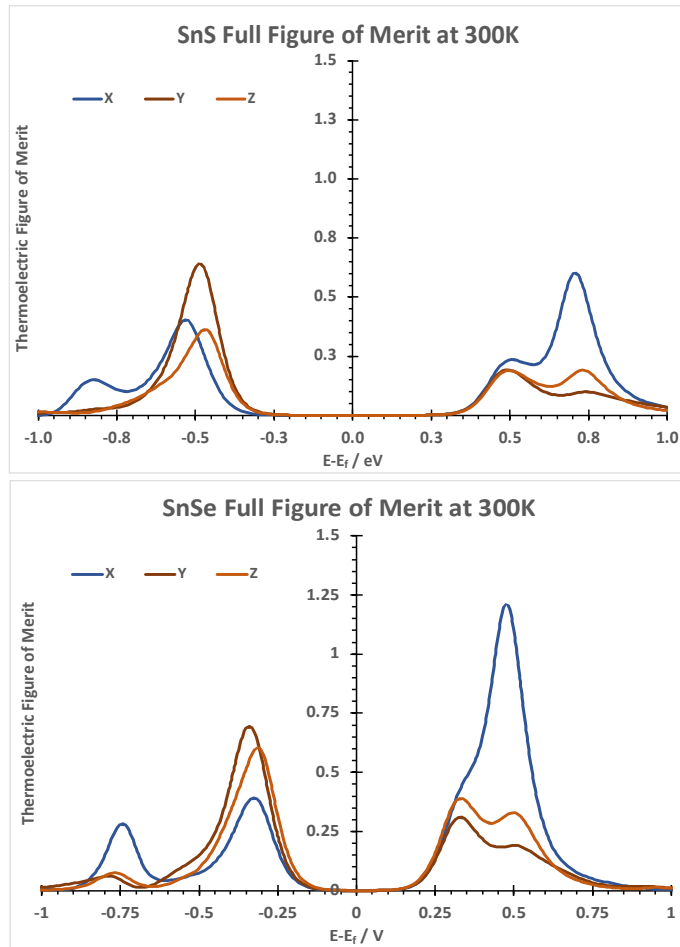


Figure 3.11: Figure of merits of SnS (above) and SnSe (below), across the chemical potential range $E_f \pm 1$ eV, for each axis

Across a Temperature Range

The relaxation time of SnS at 300 K is set to 24.9394 fs, at 500 K, 12.3156 fs, and at 750 K, 4.7640 fs. For SnSe the relaxation time at 300 K is set to 20.1182 fs, at 500 K, 7.6324 fs, and at 750 K, 5.7991 fs. As the temperature increases from 300 K to 500 K to 750 K, the dominance of *n*-type over *p*-type is enhanced in both SnS and SnSe. This is in agreement with established literature^[18] and whilst present in both structures is more pronounced in SnSe. Both structures also see a shift in the maxima position along the μ axis, with the optimal figure of merits moving closer to the centre as the temperature increases. This can be explained by the band gap closing as the temperature increases, giving more accessible states for the charge transport carriers to utilise.

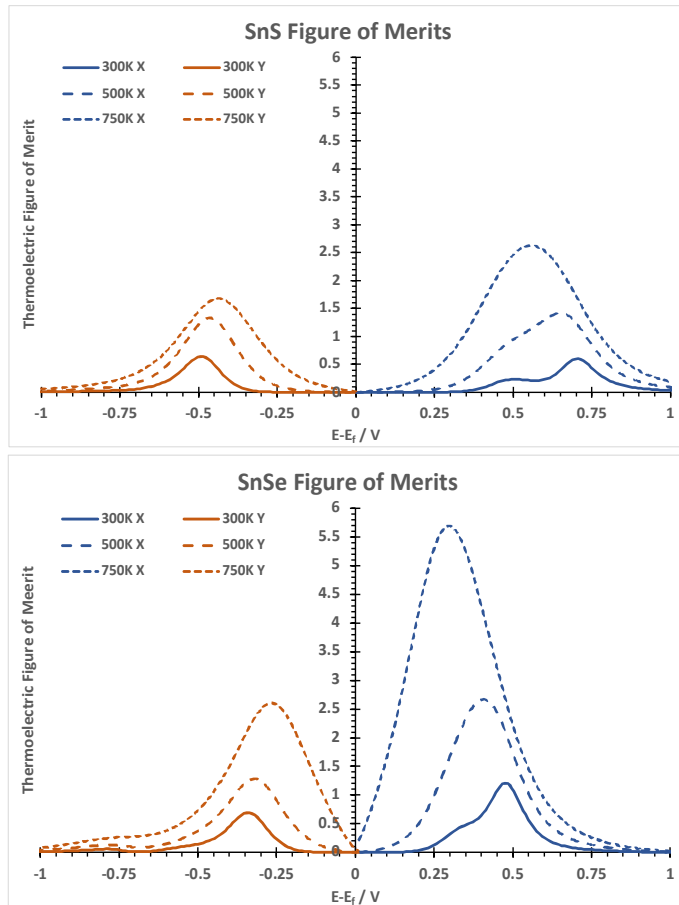


Figure 3.12: Figure of merits across chemical potentials for 300, 500 and 750 K
 Y-axis values are used for below the Fermi level and X-axis values are used for above

The figure of merits presented here reach far higher peaks than currently obtained experimental figure of merits. This can be due to a number of factors, but notably the “doping” present in these calculations are obtained through simply adjusting the chemical potential of the system, whereas doping in practice would almost invariably involve structural changes from brought about by the dopant, as well as the electronic and vibrational effects of dopants that are beyond the scope of this work.

3.2 - SnS (*Cmcm*)

With the view to lowering the lattice thermal conductivity and improving upon the already respectable thermoelectric properties of the SnX compounds, the high-temperature *Cmcm* phase is an interesting material to examine. When measuring the thermoelectric figure of merit as temperature increases, pure SnS shows a shallow increase in the low temperature region, however upon reaching ~800 K the curve takes a more rapid increase^[23]. This is taking place near the phase transition of *Pnma*-SnS into its high temperature phase, *Cmcm*-SnS. Therefore, one can look at *Cmcm*-SnS as an optimal phase for thermoelectric efficiency and understanding the underlying benefits this structure brings can allow for a more effective exploration and determination of improved SnX substructures, as well as an understanding of the effect of temperature and structural changes on the figure of merit.

3.2.1 - Electronic Properties

Characterisation

The QE relaxed structure kept the *Cmcm* symmetry and had cell lengths of $a = 6.2508 \text{ \AA}$, $b = 6.2508 \text{ \AA}$, $c = 4.1187 \text{ \AA}$, and axes angles $ab = 141.549^\circ$. These correspond to *Pnma* cell lengths of $a = 11.8044 \text{ \AA}$, $b = 4.1187 \text{ \AA}$ and $c = 4.1166 \text{ \AA}$ in an orthorhombic cell. These values are comparable to the literature orthorhombic cell lengths: $a = 11.517 \text{ \AA}$, $b = 4.162 \text{ \AA}$ and $c = 4.162 \text{ \AA}$ ^[24], and the computational literature cell lengths $a = 6.208 \text{ \AA}$, $b = 6.208 \text{ \AA}$, $c = 4.108 \text{ \AA}$, $ac = 141.322^\circ$ ^[25]. A notable difference in the *Cmcm* structure when compared to the *Pnma* is the zigzag motif along the z direction present in the *Pnma* is absent in the *Cmcm*, which crystallises with a more rigid, closely bound geometry along the b axis, but a looser structure of longer cell lengths along the x and z directions (*Pnma* $a = 11.4455 \text{ \AA}$, $b = 4.0240 \text{ \AA}$, $c = 4.448 \text{ \AA}$).

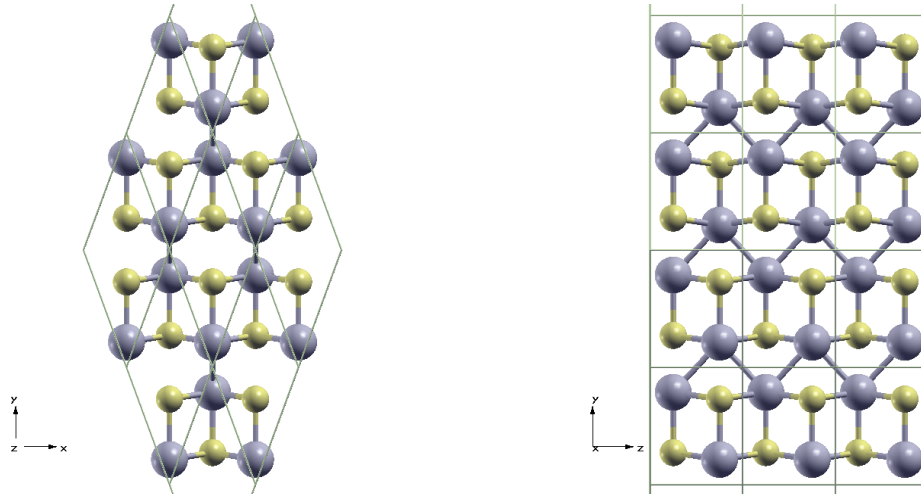


Figure 3.13: The relaxed 1 atm $Cmcm$ structure of SnS, looking down the c axis (left) and along the x direction, the ab axis (right)

The band structure shows characteristic agreement to established literature band structures and has band gaps in agreement with experimental data. The direct band gap is 0.706 eV, and the indirect band gap is 0.381 eV. Computational literature suggests a direct band gap of 1.4 eV, and an indirect of 0.3^[26], and 0.42 eV^[27]. The band gap shows similarities to other computational band structures^[7], including the position of the valence band maximum occurring in the x direction (Σ_0) and the conduction band minimum in the y direction.

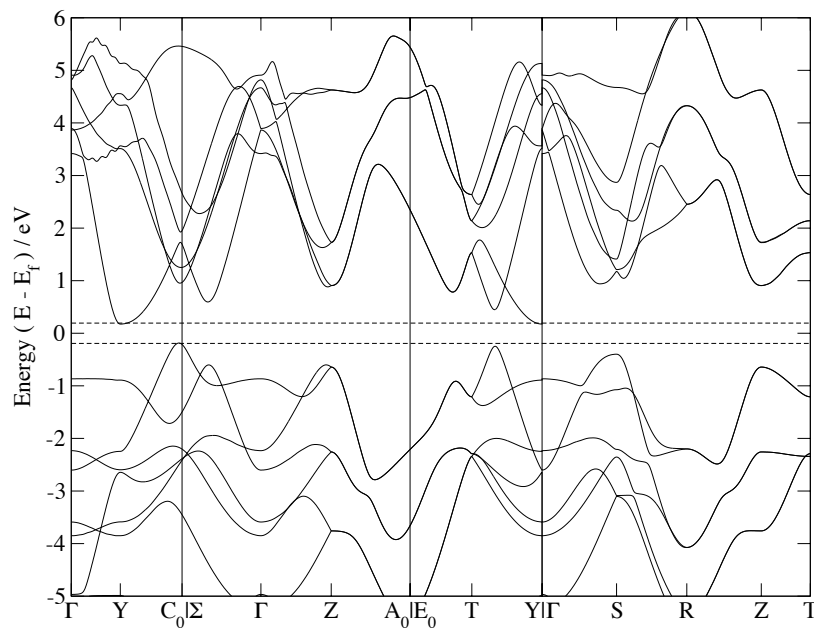


Figure 3.14: SnS- $Cmcm$ band structure calculated with Wannier90

The Seebeck values and the electronic conductivity were calculated from Wannier90. As *Cmcm*-SnS is not usually stable at room temperature and pressure, the relaxation time was set to match the *Pnma* structure, 24.9394 fs at 300K. As mentioned above, the decision to obtain these values at 300K was so as to understand more clearly the structural effect on the electronic and vibrational properties whilst in effect decoupling this from the temperature itself, and these are not meant to be an assessment of the true properties of the *Cmcm* phase.

The calculated electronic properties showed a greater anisotropy than *Pnma*-SnS, with a separation of the Seebeck cross-layer (y) and intralayer (x and z) direction curves. Whilst the Seebeck coefficient was much smaller than *Pnma*-SnS, and even lower than *Pnma*-SnSe, with maxima of 712, 549 and 733 $\mu\text{V/K}$ along the x, y and z axes, the electronic conductivity was greatly improved, with very large minimum values of 152, 248 and 270 mS/cm , nearly 100x larger than those in *Pnma*-SnSe.

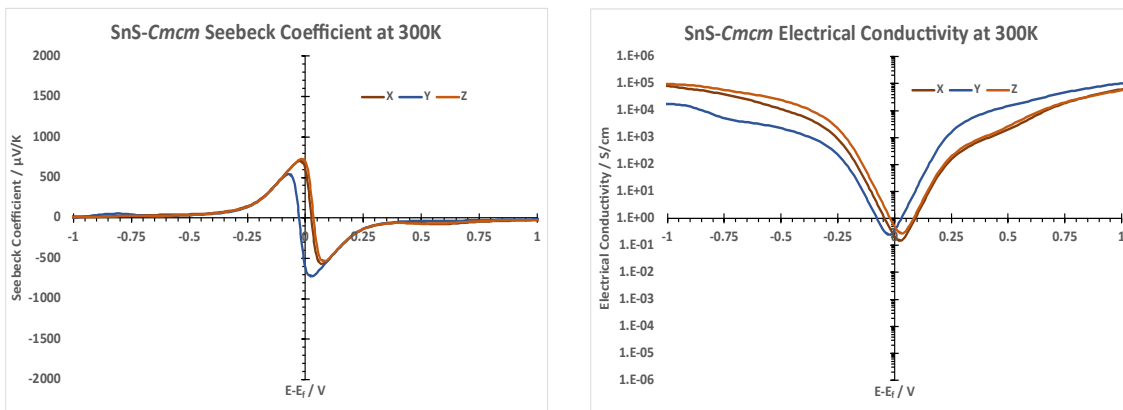


Figure 3.15: Seebeck Coefficient and Electrical Conductivity across μ values ± 1 from the Fermi level.

3.2.2 - Phononic Properties

Characterisation

The relaxed structure kept the *Cmcm* symmetry and had cell lengths of $a = 5.3406 \text{ \AA}$, $b = 5.3406 \text{ \AA}$ and $c = 3.9414 \text{ \AA}$ and an ab angle of 140.021° , these correspond to *Pnma* cell lengths of $a = 10.0377 \text{ \AA}$, $b = 3.9414 \text{ \AA}$, $c = 3.6514 \text{ \AA}$. This is again distinct from the literature

cell lengths of $a = 11.481 \text{ \AA}$, $b = 4.173 \text{ \AA}$ and $c = 4.128 \text{ \AA}$ [5], but as this calculation was run at 300 K and 1 atm there is no established literature for this specific case. However the xTB cell lengths are shorter than the QE cell lengths, $a = 11.8044 \text{ \AA}$, $b = 4.1187 \text{ \AA}$ and $c = 4.1166 \text{ \AA}$.

Phonon Spectral Analysis

The phonon spectra of *Cmcm*-SnS is shown in Fig. 3.16, with strong similarities to *Pnma*-SnS it is notable that the Γ -Y and Γ - Σ_0 (Y and X cartesian directions) show a reduced linearity, whilst the Γ -Z direction retains this feature, highlighting the effect that this symmetry change has on the x and y axes in particular. This can also be seen in the lowest frequency of these points, which shift from 0.5371, 1,2986 and 1.1204 THz in the *Pnma*-SnS x, y and z directions to 0.4151, 1.6865 and 0.8818 THz in the equivalent *Cmcm*-directions (y, z and x).

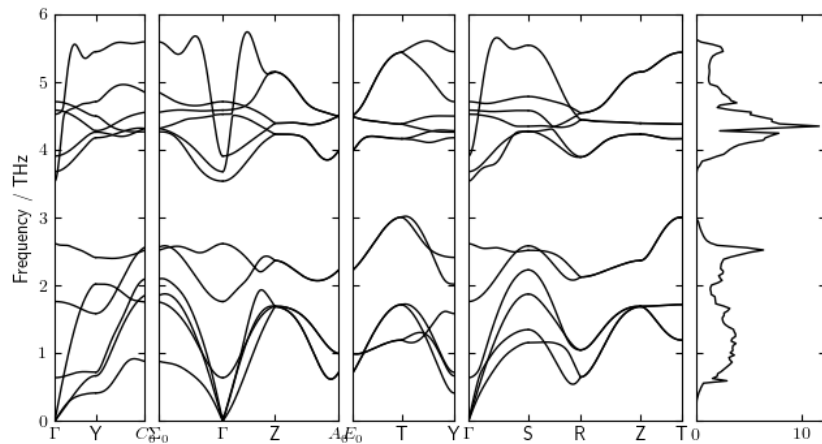


Figure 3.16: Phonon dispersion spectrum of *Cmcm*-SnS calculated through Phonopy, using CP2K/xTB for force calculation with a supercell size of 6x6x6

Thermal Conductivity

The supercell sizes chosen for the calculation of the lattice thermal conductivity were 3x3x3 for the third order interactions and 6x6x6 for the second order interactions.

The lattice thermal conductivity of *Cmcm* SnS at 300K is 0.8308, 0.4049, and 1.0338 W/m/K, for the x, y and z directions respectively (note, these correspond to *Pnma* c, a and b axes) with an isotropic average of 0.7565 W/m/k. At 850 K, the lattice thermal conductivity of *Cmcm*-SnS is 0.2929, 0.1436, and 0.3651 W/m/K for the x, y and z axes respectively,

with an isotropic average of 0.2672 W/m/K. This value is lower than shown by experimental data, with the lattice thermal conductivity of *Cmcm*-SnS usually measured at 0.5 [20, 21], but shows the expected trend of temperature dependence.

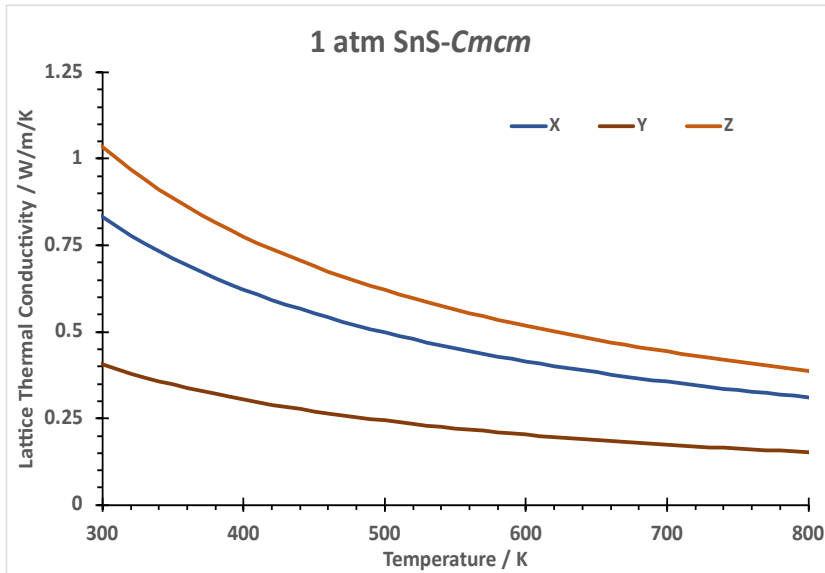


Figure 3.17: Lattice thermal conductivity, κ_{latt} , along the x, y and z directions as a function of temperature.

Phonon Lifetimes

The phonon lifetime at each frequency was calculated and plotted. The lower frequency phonons are the main heat conducting phonons, and longer lifetimes in these phonons will give rise to a larger effect on the material’s lattice thermal conductivity. The *Cmcm*-SnS structure can be seen to exhibit a significant reduction in phonon frequency lifetimes when compared to the *Pnma*-SnS, especially in the low-frequency region. This indicates a large disruption of phonons present in the more symmetric *Cmcm* structure through phonon scattering modes and is in agreement with the relative lattice thermal conductivities of these two structures.

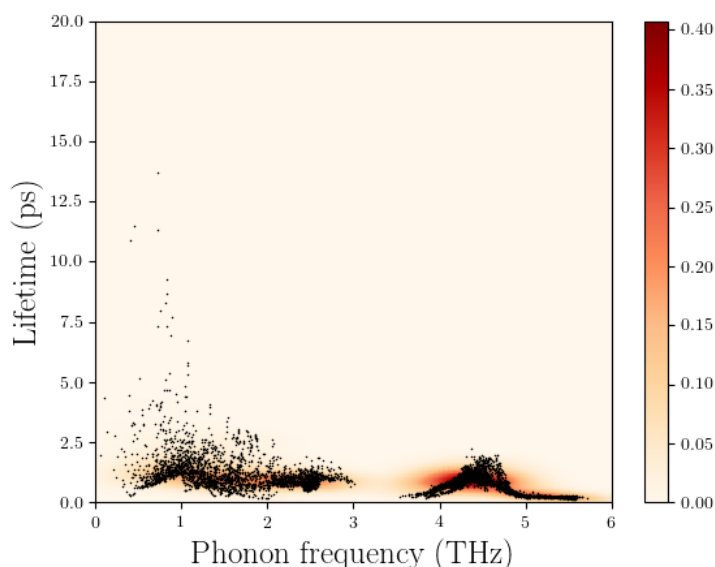


Figure 3.18: The lifetimes of phonons of varying frequencies for *Cmcm*-SnS. The heatmap indicating a greater concentration of phonons.

3.2.3 - Full Figure of Merit

At 300 K

Due to the lack of data for a 300K *Cmcm* phase of SnS, the relaxation time was set to the *Pnma* phase relaxation time, 23.7 fs. As for the individual electronic and vibrational aspects, these are calculated for comparison with the *Pnma* structure and not an attempt to justify this material, but rather to gain an understanding of the effect on the interrelated properties brought about by a shift from the *Pnma* to the *Cmcm* symmetry of the tin chalcogenides.

The 300 K figure of merits show the similar large *n*-type figure of merit along the layered direction as seen in the *Pnma* structures, with the curves better matching the *Pnma*-SnSe curves than the *Pnma*-SnS, indicating that the SnSe shares more electronic and vibrational similarity to the *Cmcm* symmetry than the SnS. The peaks of the figure of merit maxima in the *Cmcm*-SnS structure are also much closer to the Fermi-level than in either *Pnma* structure, and show already good values at the Fermi-level itself, indicating a minimal amount of doping would be needed in this theoretical configuration.

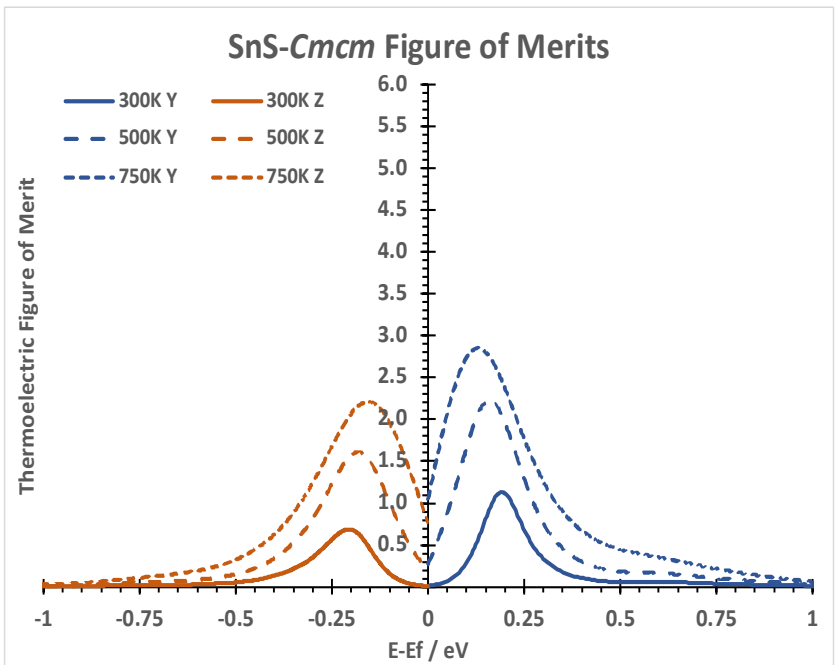
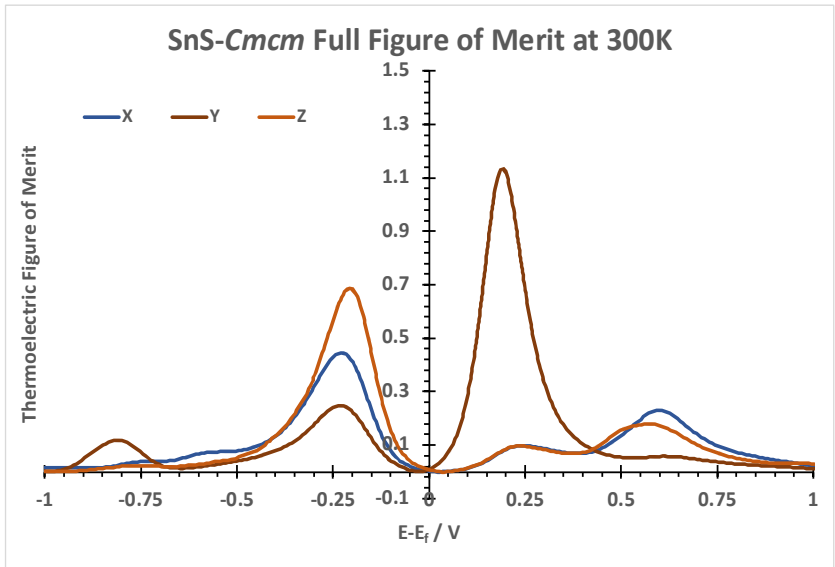


Figure 3.19: Figure of merits across chemical potentials for 300, 500 and 750 K
 Y-axis values are used for below the Fermi level and X-axis values are used for above

3.3 - Comparison

3.3.1 - Electronic Properties

Power Factor

The power factor is the theoretical electronic suitability of the material to thermoelectric activity. It corresponds to $PF = S^2\sigma$, such that the thermal conductivity is excluded. This allows the material to be evaluated in two parts, the electronic, through the power factor, and the lattice, through the lattice thermal conductivity. Whilst this neglects the electronic component to the thermal conductivity, this is generally far smaller than the lattice except at high temperatures. The Power Factors are shown in Fig. 3.20 and highlight the similarities in the electronic strengths of *Pnma*-SnS and *Pnma*-SnSe, and even the superiority of the *p*-doped *Pnma*-SnS. The power factors of the *Cmcm*-SnS show smaller peaks than the *Pnma*-SnS, indicating a lower maximum electronic suitability but do show higher power factors closer to the Fermi level which would be useful in minimising the disruption brought to the structural properties by dopants.

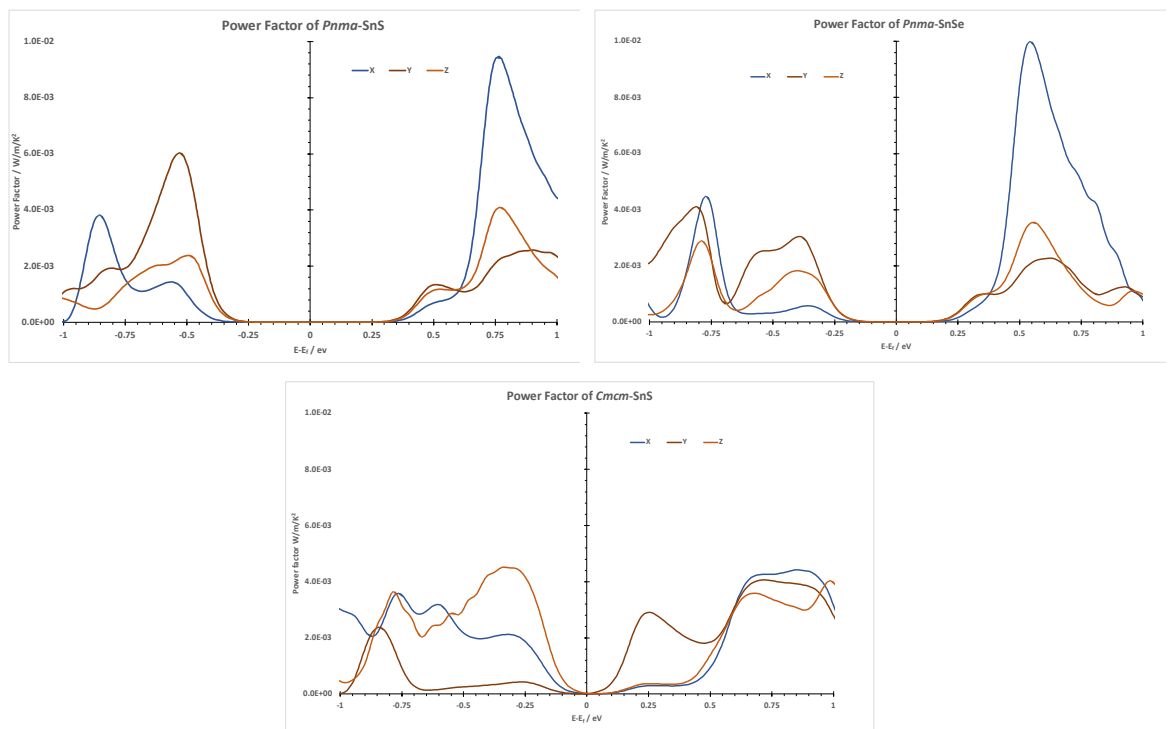


Figure 3.20: The power factors ($S^2\sigma$) of *Pnma*-SnS (upper left), *Pnma*-SnSe (upper right) and *Cmcm*-SnS (lower middle)

3.3.2 – Phononic Properties

Lattice Thermal Conductivity

The lattice thermal conductivities are shown in Fig. 3.21, separated into the cross-layer direction and the averaged intralayer direction. This highlights the difference between *Pnma*-SnS and *Pnma*-SnSe, with SnSe less than half that of *Pnma*-SnS across the temperature range. The *Cmcm*-SnS lattice thermal conductivities are seen to be much closer to the *Pnma*-SnSe than the *Pnma*-SnS, indicating the similarities in vibrational properties of these two structures and the improvement brought about by a more *Cmcm*-like symmetry from *Pnma*-SnS.

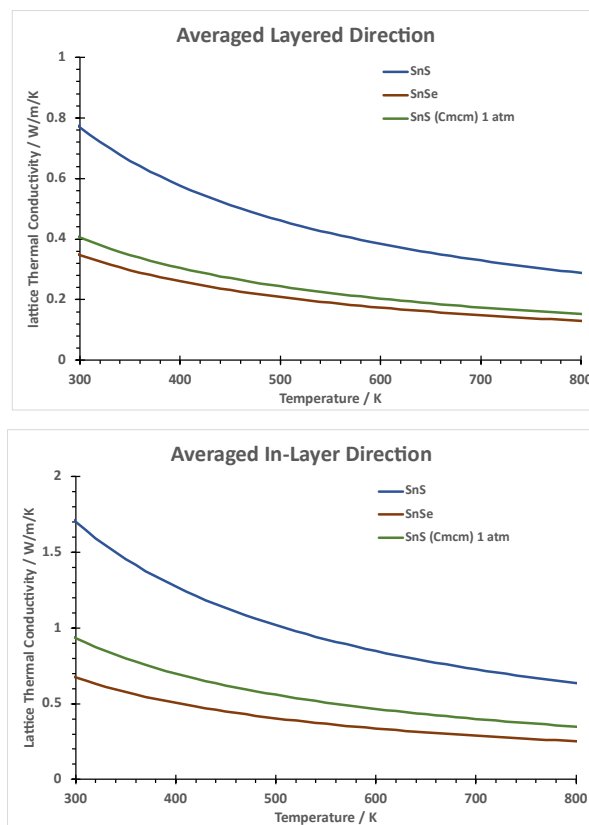


Figure 3.21: The lattice thermal conductivities of the layered direction, a in *Pnma*, y in *Cmcm* (above), and the intralayer direction, b and c in *Pnma*, x and z in *Cmcm* (below)

Phonon Mean Free Paths

The phonons' contributions to the lattice thermal conductivity were again determined, and their mean free paths obtained. This is shown in Fig. 3.22, and signifies the importance of the mean free path lengths in the lowering of the lattice thermal conductivity. The removal of the longer mean free path phonons leads to a sharp reduction in the lattice thermal conductivity of *Cmcm*-SnS through new phonon scattering modes, bringing the curve in line with the *Pnma*-SnSe mean free path lattice thermal conductivity contributions. The manipulation of the material to more *Cmcm*-like nature is therefore seen as a clear objective in the reduction of lattice thermal conductivity, and overall improvement of the figure of merit, through *Cmcm*-like phonon scattering.

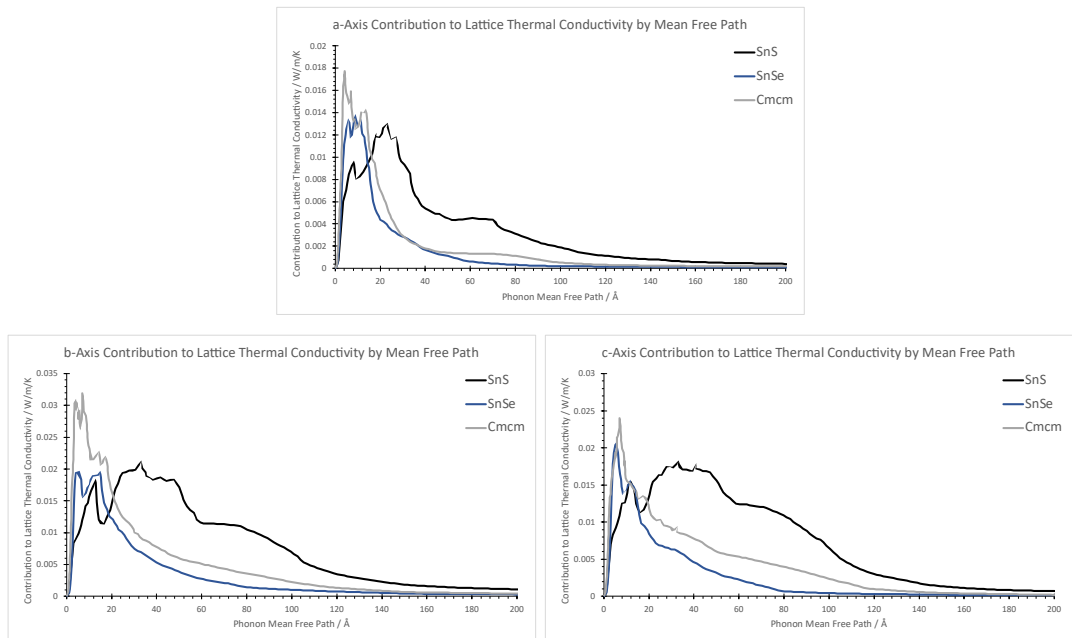


Figure 3.22: The phonon contribution to the lattice thermal conductivity at 300 K by their mean free path, shown along the *Pnma*-a/*Cmcm*-b (above), *Pnma*-b/*Cmcm*-c (lower left) and *Pnma*-c/*Cmcm*-a (lower right) axes

Phonon Lifetimes

As shown in Fig. 3.9, the low frequency phonon modes are the main contributors to the lattice thermal conductivity and lowering the strength of these modes is a necessary step in decreasing the lattice thermal conductivity. In Fig. 3.23, the phonon lifetimes of the low frequency modes (below 2 THz) are plotted. The difference between *Pnma*-SnS and *Pnma*-

SnSe are clear in the flatter ascent and more concentrated phonon lifetime spread. This effect is even more prominent when comparing the lifetime plots of *Pnma*-SnS and *Cmcm*-SnS, where the *Cmcm* phase has very a very low and narrow band of phonon modes. However, the fact that *Pnma*-SnSe has a lower lattice thermal conductivity than *Cmcm*-SnS in spite of a similar mean free path contribution and higher low-frequency phonon lifetimes shows that whilst this is an important aspect, it is not the sole contributor to the lattice thermal conductivity, and other factors are involved in the disruption of heat transport through the *Pnma*-SnSe lattice.

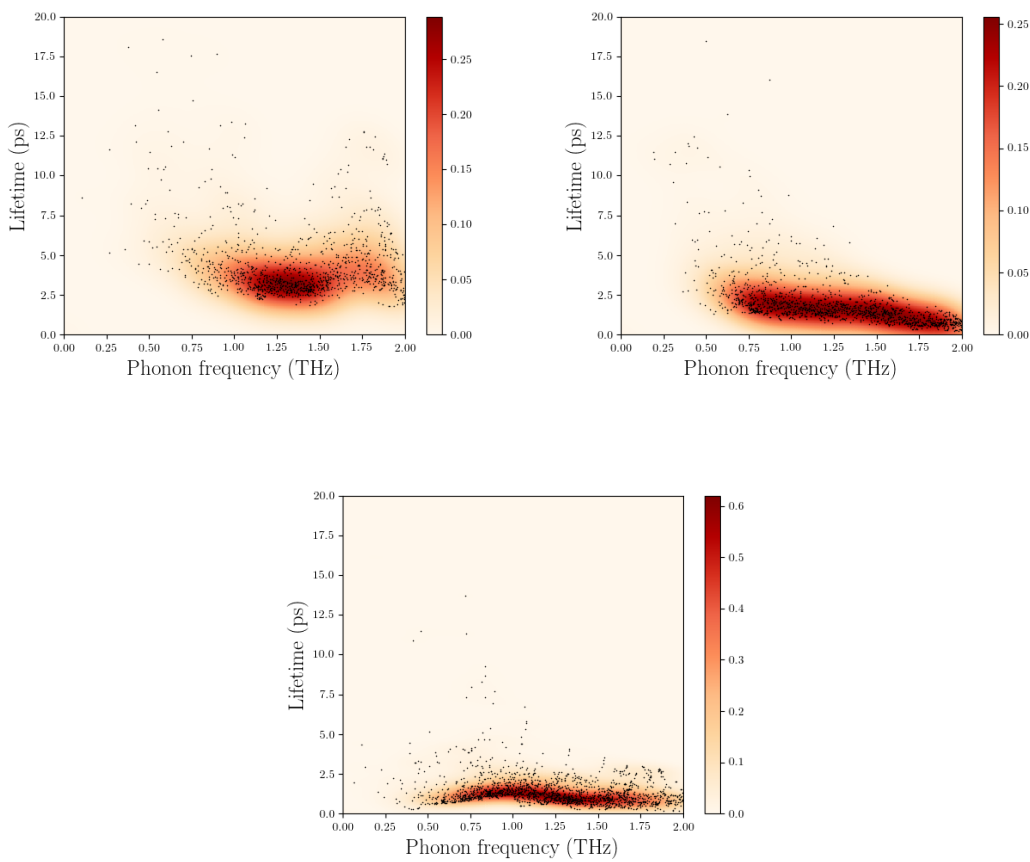


Figure 3.23: Phonon lifetimes of *Pnma*-SnS (upper left), *Pnma*-SnSe (upper right), and *Cmcm*-SnS (lower middle)

Phonon Group Velocities

The reason for the difference in the lattice thermal conductivities of *Pnma*-SnSe and *Cmcm*-SnS can be seen in the group velocities of the phonon modes of the two materials. In Fig. 3.24 the group velocities by frequency of phonon modes are plotted against the phonon frequency, showing the larger group velocities of the *Cmcm* phase. It is this increase in phonon velocities which give rise to the increased lattice thermal conductivity of *Cmcm*-SnS, which works against the mean free path reduction.

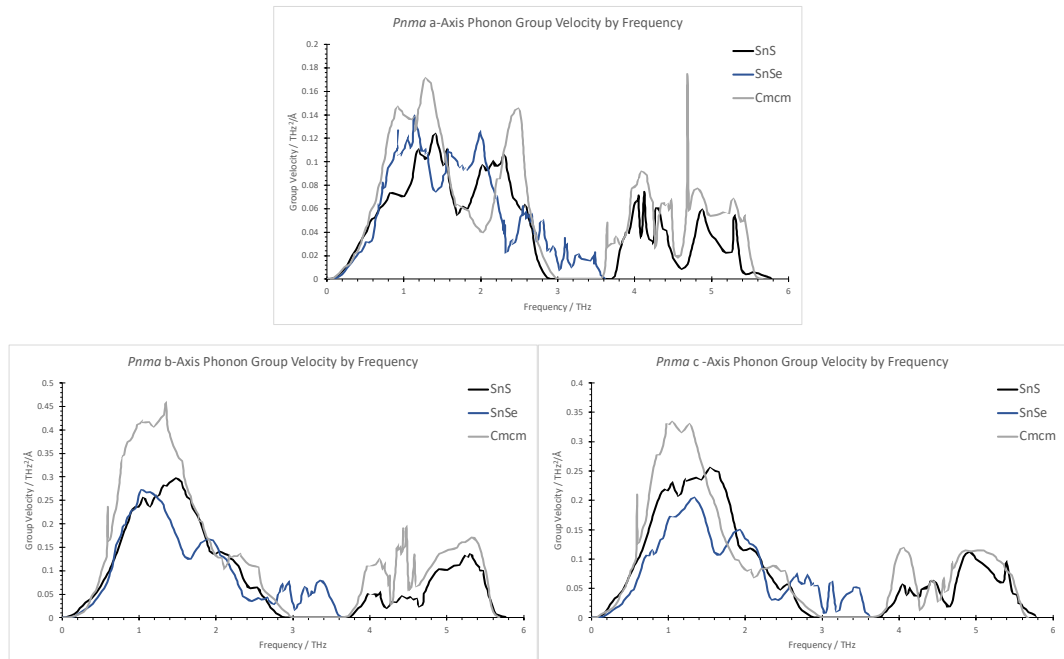


Figure 3.24: Group velocities of phonon modes by frequency, along the *Pnma*-a/*Cmcm*-b (above), *Pnma*-b/*Cmcm*-c (lower left) and *Pnma*-c/*Cmcm*-a (lower right) axes

The group velocities shown in Fig. 3.24 also show agreement with the calculated lattice thermal conductivities when comparing *Cmcm*-SnS to *Pnma*-SnSe, where the relatively similar lattice thermal conductivities across the layers are highlighted by the similar levels in the group velocities, and the larger disparity in the lattice thermal conductivities of the in-layer axes can be seen in the larger group velocities of the *Pnma*-b and *Pnma*-c axes. The total group velocities for each structure across the entire frequency range, resolved by cartesian directions x, y, and z, are shown below:

	X	Y	Z
<i>Pnma</i> -SnS	0.24303	0.51925	0.46133
<i>Pnma</i> -SnSe	0.20491	0.37799	0.30117
<i>Cmcm</i> -SnS*	0.33741	0.75565	0.53466

Table 3.1: Total group velocities, give in $\text{THz}^2\text{A}^{-1}$, separated by cartesian direction.

**Cmcm* shown to correspond to its *Pnma* axes, i.e. *Cmcm* x-axis is presented in the z-axis column., *Cmcm* y-axis in the x-axis column, and *Cmcm* z-axis in the y-axis column.

3.3.3 - Figure of Merit

At 300, 500 and 750 K

With the lattice thermal conductivity and the electronic properties obtained, the full figure of merit can be determined. Shown as a function of the chemical potential, μ , the strongest axes below and above the Fermi level (*Pnma* X and *Cmcm* Y above the Fermi level, *Pnma* Y and *Cmcm* Z below) are shown at each temperature. This highlights that a low temperature *Cmcm* phase would have a stronger figure of merit than it's corresponding *Pnma* structure with a much lower need for doping, with acceptable figure if merits seen significantly closer to the Fermi-level. However, this effect is less pronounced at higher temperatures, where *Cmcm* is more stable.

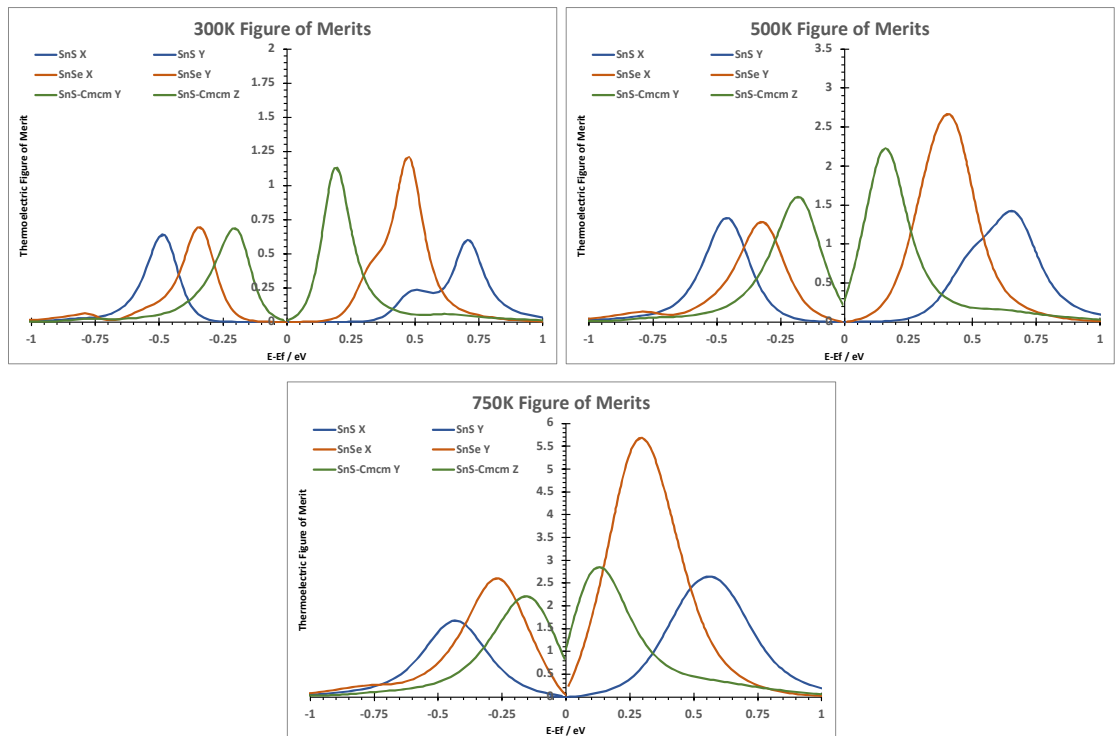


Figure 3.24: Full figure of merits of the three materials at 300 K (upper left), 500 K (upper right) and 750 K (lower middle)

Across the temperature range 300 K to 750 K

When applied to a thermoelectric device, the single-temperature efficiencies are less important than the efficiency across the temperature range. With a hot and a cold side, the material used will need to retain a high figure of merit across the device. The efficiencies of *Pnma*-SnS, SnSe and *Cmcm*-SnS are shown below, using the average values of the 300, and 500 K figures of merit, shown against μ , and the 300, 500 and 750 K figures of merit, also against μ . This again highlights the strength of *Pnma*-SnSe as a thermoelectric material, but also shows that a more *Cmcm*-like phase would improve the suitability of the materials across the temperature range by not only improving the maximal *p*- and *n*-type figure of merits compared to *Pnma*-SnS, but also bringing these maxima to more easily achievable doping levels. It can also be seen that the benefits from the *Cmcm* structure are felt most strongly at the lower temperature range, with the largest difference between the peaks, and less when the temperature range is increased.

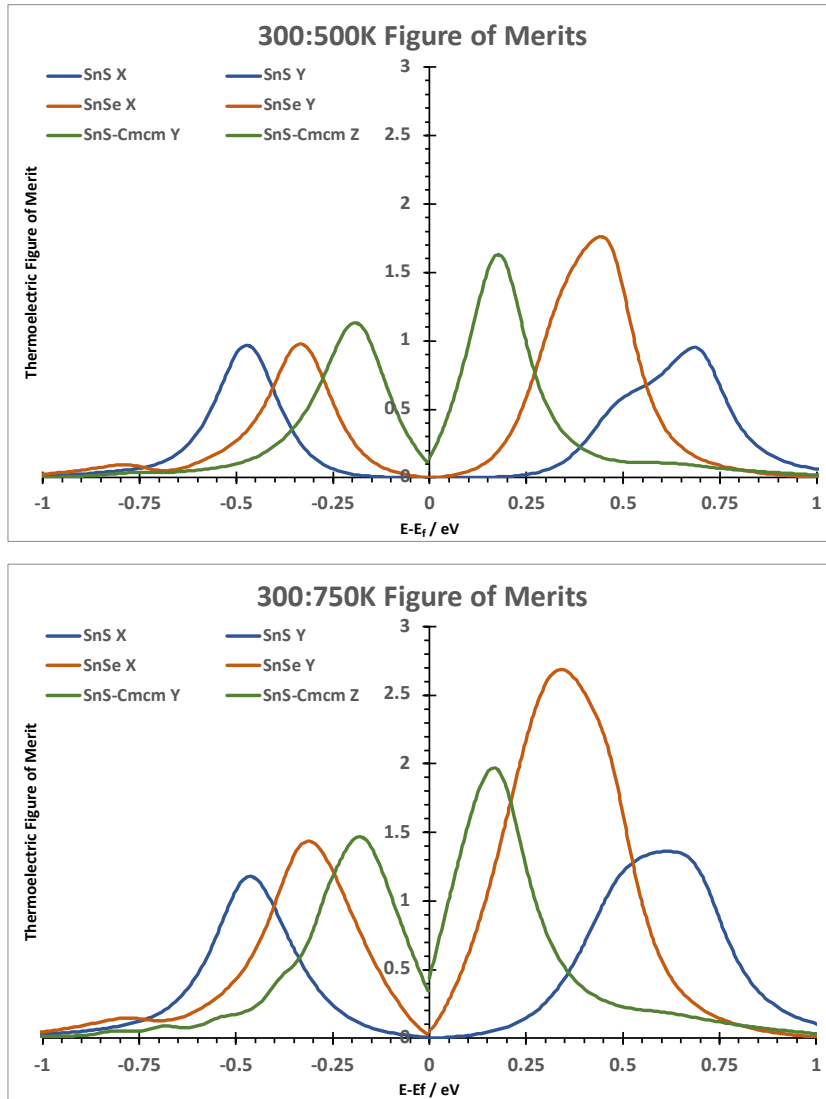


Figure 3.25: The averaged figure of merits of 300 and 500 K (above), and 300, 500 and 750 K (below), across the chemical potential range $E_f \pm 1$

The values of the figure of merits at 300, 500 and 750 K, resolved by maxima in the two doping regions, are shown in Tables 3.1, 3.2 and. 3.3 below

	300K		500K		750K	
	<i>n</i> -type	<i>p</i> -type	<i>n</i> -type	<i>p</i> -type	<i>n</i> -type	<i>p</i> -type
SnS	0.604	0.641	1.423	1.333	2.644	1.678
SnSe	1.212	0.696	2.667	1.285	5.686	2.602
<i>Cmcm</i>	1.136	0.688	2.229	1.607	2.852	2.213

Table 3.1: Maximum figures of merit at 300, 500 and 700 K

The peak maxima from the curves in Fig. 3.25 are presented below in Table 3.2, along with the data for the averaged high temperature figure of merits (500 and 750 K), separated into the *n*-type (*Pnma* x and *Cmcm* y) and *p*-type (*Pnma* y and *Cmcm* z) directions.

	300K:500K		300K:750K		500K:750K	
	<i>n</i> -type	<i>p</i> -type	<i>n</i> -type	<i>p</i> -type	<i>n</i> -type	<i>p</i> -type
SnS	0.95	0.97	1.36	1.18	1.93	1.49
SnSe	1.76	0.98	2.69	1.44	3.80	1.87
<i>Cmcm</i>	1.63	1.13	1.98	1.47	2.51	1.89

Table 3.2: The figures of merit across the temperature ranges, at the optimal chemical potential of each doping region

Fig. 3.25 and the corresponding data are the averaged figure of merits at fixed μ values. As such, a peak that shifts relative to the Fermi level would show a lower averaged figure of merit. The data for the maximum averaged figure of merits across a temperature range independent of μ is shown below in Table 3.3.

	300K:500K		300K:750K		500K:750K	
	<i>n</i> -type	<i>p</i> -type	<i>n</i> -type	<i>p</i> -type	<i>n</i> -type	<i>p</i> -type
SnS	1.013	0.987	1.557	1.218	2.034	1.506
SnSe	1.940	0.990	3.189	1.527	4.177	1.943
<i>Cmcm</i>	1.682	1.148	2.072	1.503	2.540	1.910

Table 3.3: The figure of merit maxima across the temperature ranges, with optimal chemical potential at each individual temperature

3.4 - Summary

3.4.1 - Lattice Thermal Conductivities

Correct Ordering of Pnma Lattice Thermal Conductivities

There have been a number of *ab initio* attempts to accurately calculate the lattice thermal conductivities, but the complexities involved have often given rise to issues such as an incorrect ordering of the SnS and SnSe *Pnma* structures. Due to the larger mass of the selenium atom, it is expected, and observed in experimental data, for *Pnma*-SnSe to exhibit a lower lattice thermal conductivity than *Pnma*-SnS. However, it has been noted that some calculations on these materials produce an inverse ordering, with *Pnma*-SnS showing a lower lattice thermal conductivity than its SnSe counterpart^[14]. This is not the case in this work, and the *Pnma* structures show good agreement with experimental data in both scale and sequence through the use of the xTB tight-binding approximation, resulting in a far clearer picture of the vibrational modes of the structure.

Understanding the Phonon Pathway Disruptions

For effective design of thermoelectric materials, an understanding as to the methods and modes of phonon disruption is paramount. The focus on lower frequency phonon modes as the major heat carriers is highlighted by the calculation of the contribution to lattice thermal conductivity by frequency, where the acoustic phonons showed significantly higher contributions to the lattice thermal conductivity compared to the contributions from the optical phonons (Fig. 3.8).

The evaluation of the difference in phonon lifetimes of these low frequency modes gives a solid base for understanding why *Pnma*-SnSe hold such a low lattice thermal conductivity, with lifetimes in the low frequency region significantly lower than those of *Pnma*-SnS (Fig. 3.23). This is also shown in the mean free path contributions to the lattice thermal conductivity (Fig. 3.22) where the axis resolved curves show considerable decreases in the contribution of long mean free paths to the lattice thermal conductivity in *Pnma*-SnSe compared to *Pnma*-SnS

However, the comparison of the phonon lifetimes and mean free paths of *Pnma*-SnSe to *Cmcm*-SnS with respect to the lattice thermal conductivities of these materials indicated that this is not the sole effect on the heat transport. This can be seen in the plots of the group velocities of the phonon frequencies (Fig. 3.24) where *Cmcm* structure shows larger group velocities than *Pnma*-SnSe, especially in the in-layer axes, which correspond to the largest difference in lattice thermal conductivity between *Pnma*-SnSe and *Cmcm*-SnS.

From the lattice thermal conductivities, and from the evaluations of phonon lifetimes, mean free paths and group velocities, the transformation from *Pnma* to *Cmcm* is shown to be particularly effective in phonon scattering, mitigated slightly by higher phonon group velocities. This overall trend presents the *Cmcm* as a good theoretical optimum in implementing structural changes in the tin chalcogenide structures.

3.4.2 - Electronic Suitability

Although the focus in achieving high thermoelectric efficiency of SnX materials is in the lowering of the lattice thermal conductivity, the electronic suitability of the material cannot be ignored. Any enhancement of phonon scattering modes obtained through structural changes must be insured to not seriously hamper the electronic conductivity or Seebeck coefficient, or the gains made will be negated.

In the *Pnma*-SnS and SnSe structures, the main difference is the superiority of the Seebeck coefficient (SnS) or electrical conductivity (SnSe). The a-axis power factors across the chemical potential range follow very similar paths and peaks, whereas the b and c axes show a much greater electronic suitability of *Pnma*-SnS. Therefore, the increase in the figure of merit of *Pnma*-SnSe is confirmed to be through the decrease in lattice thermal conductivity. The *Cmcm*-SnS electronic characterisation showed particularly low Seebeck coefficients, but very high electronic conductivities, and whilst the power factors indicated the same cross-layer favouring of *n*-type, and in-layer favouring of *p*-type figure of merit, the difference was less pronounced than in the *Pnma* power factors.

Ultimately the strong electronic properties of SnS and SnSe, and their structural similarity give a good indication that any mixed structure will share these properties, and whilst the *Cmcm*-like structure holds promise for the lattice thermal conductivity it indicates a lowering of electronic suitability that could harm the figure of merit.

References

- [1] H. Wang, Z. M. Gibbs, Y. Takagiwa and G. J. Snyder, "Tuning Bands of PbSe for Better Thermoelectric Efficiency," *Energy & Environmental Science*, vol. 7, pp. 804-811, 2014.
- [2] S. N. Girard, J. He, X. Zhou, D. Shoemaker, C. M. Jaworski, C. Uher, V. P. Dravid, J. P. Heremans and M. G. Kanatzidis, "High Performance Na-doped PbTe–PbS Thermoelectric Materials: Electronic Density of States Modification and Shape-Controlled Nanostructures," *Journal of the American Chemical Society*, vol. 133, no. 41, pp. 16588-16597, 2011.
- [3] M. Zebarjadi, K. Esfarjani, M. S. Dresselhaus, Z. F. Ren and G. Chen, "Perspectives on Thermoelectrics: From Fundamentals to Device Applications," *Energy & Environmental Science*, vol. 5, pp. 5147-5162, 2012.
- [4] S. Li, X. Li, Z. Ren and Q. Zhang, "Recent Progress Towards High Performance of Tin Chalcogenide Thermoelectric Materials," *Journal of Materials Chemistry A*, vol. 6, pp. 2432-2448, 2018.
- [5] T. Chattopadhyay, J. Pannetier and H. G. von Schnering, "Neutron Diffraction Study of the Structural Phase Transition in SnS and SnSe," *Journal of Physics and Chemistry of Solids*, vol. 47, no. 9, pp. 879-885, 1986.
- [6] K. Persson, *Materials Data on SnS (SG:62) by Materials Project*, Lawrence Berkeley National Lab, 2014.
- [7] K. Persson, *Materials Data on SnSe (SG:62) by Materials Project*, Lawrence Berkeley National Lab, 2014.
- [8] W. Albers, C. Haas and F. van der Maesen, "The Preparation and the Electrical and Optical Properties of SnS Crystals," *Journal of Physics and Chemistry of Solids*, vol. 15, no. 3-4, pp. 306-310, October 1960.
- [9] A. K. Deb and V. Kumar, "Bandgap Engineering in Semiconducting One to Few Layers of SnS and SnSe," *Physica Status Solidi B*, vol. 254, pp. 1-8, 2016.
- [10] W. He, D. Wang, J.-F. Dong, Y. Qiu, L. Fu, Y. Feng, Y. Hao, G. Wang, J. Wang, C. Liu, J.-F. Li, J. He and L.-D. Zhao, "Remarkable Electron and Phonon Band Structures Lead to a High Thermoelectric Performance $ZT > 1$ in Earth-Abundant and Eco-Friendly SnS Crystals," *Journal of Materials Chemistry A*, vol. 6, no. 21, pp. 10048-10056, 2018.
- [11] L.-D. Zhao, G. Tan, S. Hao, J. He, Y. Pei, H. Chi, H. Wang, S. Gong, H. Xu, V. P. Dravid, C. Uher, G. J. Snyder, C. Wolverton and M. G. Kanatzidis, "Ultrahigh power factor and thermoelectric performance in hole-doped single-crystal SnSe," *Science*, vol. 351, no. 6269, pp. 141-144, 2015.
- [12] S. Hao, V. P. Dravid, M. G. Kanatzidis and C. Wolverton, "Research Update: Prediction of High Figure of Merit Plateau in SnS and Solid Solution of (Pb,Sn)S," *APL Materials*, vol. 4, no. 10, p. 104505, 2016.
- [13] H. Wu, K. Peng, B. Zhang, X. N. Gong, Z. Z. Feng, X. M. Zhang, M. Xi, X. M. Yan, Y. S. Zhang, G. Y. Wang, X. Lu and X. Y. Zhou, "Realizing High Thermoelectricity in Polycrystalline SnS via Manipulating Fermi Surface Anisotropy and Phonon Dispersion," *Materials Today Physics*, vol. 14, pp. 100221-100231, 2020.
- [14] J. M. Skelton, L. A. Burton, A. J. Jackson, F. Oba, S. C. Parker and A. Walsh, "Lattice dynamics of the tin sulphides SnS₂, SnS and Sn₂S₃: vibrational spectra and thermal transport," *Physical Chemistry Chemical Physics*, no. 19, pp. 12452-12465, 2017.
- [15] P. G. Klemens, "Theory of Lattice Thermal Conductivity: Role of Low-Frequency Phonons," *International Journal of Thermophysics*, vol. 2, pp. 55-62, 1981.

- [16] D. A. Broido, M. Malorny, G. Birner, N. Mingo and D. A. Stewart, "Intrinsic Lattice Thermal Conductivity of Semiconductors from First Principles," *Applied Physics Letters*, vol. 91, no. 23, p. 231922, 2007.
- [17] J. M. Skelton, L. A. Burton, S. C. Parker, A. Walsh, C.-E. Kim, A. Soon, J. Buckeridge, A. A. Sokol, C. R. A. Catlow, A. Togo and I. Tanaka, "Anharmonicity in the High-Temperature Cmcm Phase of SnSe: Soft Modes and Three-Phonon Interactions," *Physical Review Letters*, vol. 117, no. 7, p. 075502, 2016.
- [18] R. Guo, X. Wang, Y. Kuang and B. Huang, "First Principles Study of Anisotropic Thermoelectric Transport Properties of IV-VI Semiconductor Compounds SnSe and SnS," *Physical Review B*, vol. 92, no. 11, p. 115202, 2015.
- [19] L.-D. Zhao, S.-H. Lo, Y. Zhang, H. Sun, G. Tan, C. Uher, C. Wolverton, V. P. Dravid and M. G. Kanatzidis, "Ultralow Thermal Conductivity and High Thermoelectric Figure of Merit in SnSe Crystals," *Nature*, vol. 508, pp. 373-377, 2014.
- [20] Q. Tan, L.-D. Zhao, J.-F. Li, C.-F. Wu, T.-R. Wei, Z.-B. Xing and M. G. Kanatzidis, "Thermoelectrics with Earth Abundant Elements: Low Thermal Conductivity and High Thermopower in Doped SnS," *Journal of Materials Chemistry A*, vol. 2, no. 41, pp. 17302-17306, 2014.
- [21] Asfandiyar, B. Cai, L.-D. Zhao and J.-F. Li, "High Thermoelectric Figure of Merit $ZT > 1$ in SnS Polycrystals," *Journal of Materiomics*, vol. 6, no. 1, pp. 77-85, 2020.
- [22] H. Wu, X. Lu, G. Wang, K. Peng, H. Chi, B. Zhang, Y. Chen, C. Li, Y. Yan, L. Guo, C. Uher, X. Zhou and X. Han, "Sodium-Doped Tin Sulfide Single Crystal: A Nontoxic Earth-Abundant Material with High Thermoelectric Performance," *Advanced Energy Materials*, vol. 8, no. 20, p. 1800087, 2018.
- [23] E. K. Chere, Q. Zhang, K. Dahal, F. Cao, J. Mao and Z. Ren, "Studies on Thermoelectric Figure of Merit of Na-doped p-type Polycrystalline SnSe," *Journal of Materials Chemistry A*, vol. 4, no. 5, pp. 1848-1854, 2016.
- [24] H. Wiedemeier and F. J. Csilag, "The Thermal Expansion and High Temperature Transformation of SnS and SnSe," *Zeitschrift für Kristallographie*, vol. 149, pp. 17-30, 1979.
- [25] K. Persson, *Materials Data on SnS (SG:63) by Materials Project*, Lawrence Berkeley National Lab, 2016.
- [26] A. R. H. F. Ettema, R. A. de Groot, C. Haas and T. S. Turner, "Electronic Structure of SnS Deduced from Photoelectron Spectra and Band-Structure Calculations," *Physical Review B*, vol. 46, no. 12, pp. 7363-7373, 1992.
- [27] B.-Z. Sun, Z. Ma, C. He and K. Wu, "Enhanced Thermoelectric Performance of Layered SnS Crystals: The Synergetic Effect of Temperature and Carrier Concentration," *RSC Advances*, vol. 5, pp. 56382-56390, 2015.

Chapter 4:

Uniform Layering

With the aim to reduce the lattice thermal conductivity of the SnX system, and with the understanding that a lowered phonon lifetime is a key pathway to this goal, the use of the existing structural layering was seen as a strong avenue of approach. The layers would have to be electronically compatible, such that the electronic conductivity is not greatly disrupted by the boundaries between the layers, but still providing a strong enough lattice distortion to reduce the phonon lifetimes and dampen the lattice thermal conductivity. The effectiveness of alloying SnS and SnSe has been shown by the improvement of the figure of merit of SnS through alloying with SnSe to $\text{SnS}_{0.2}\text{SnSe}_{0.8}$ from 0.15 to 0.64^[1] and from 0.19 to 0.82 W/m/K^[2] at 823 K. It has also been shown that the layering of SnS with TiS_2 can greatly reduce the lattice thermal conductivities of the in-layer direction, $\text{TiS}_2 \approx 1.7$ W/m/K and $(\text{SnS})_{1.2}(\text{TiS}_2)_2 \approx 1.0$ W/m/K at 300 K, as well as the cross-layer directions, $\text{TiS}_2 \approx 1.4$ W/m/K and $(\text{SnS})_{1.2}(\text{TiS}_2)_2 \approx 0.4$ W/m/K at 300 K^[3].

As shown in previous work with PbSe/PbTe layering^[4], the layer thickness can show a non-linear relationship to lattice thermal conductivity, where a finer layering does not necessarily produce the lowest heat transport. Through the interlayering of *Pnma*-SnS and *Pnma*-SnSe boundary edges were added to the system to reduce the heat transport via boundary scattering effects, but with the aim to keep the electronic suitability at a good level such that the power factor peaks are comparable with those of *Pnma*-SnS and SnSe.

As such, three structures were initially prepared with varying layer thickness, SnS/SnSe (1:1-*Pmn2*₁), 2SnS/2SnSe (2:2-*Pm*) and 3SnS/3SnSe (3:3-*Pmn2*₁), and their electronic and heat transport properties examined.

4.1 – SnS/SnSe, 2SnS/2SnSe and 3SnS/3SnSe

4.1.1 - Electronic Properties

Characterisation

The SnS/SnSe (1:1), 2SnS/2SnSe (2:2) and 3SnS/3SnSe (3:3) retained GeS-type (B16) derived structures, (1:1 and 3:3 SG *Pmn2*₁, 2:2 SG *Pm*). Their crystal structures were relaxed with Quantum Espresso using a GGA-PBE exchange-correlation functional, the relaxed lattice parameters were: $a = 11.6023$ Å, $b = 4.1105$ Å, $c = 4.5357$ Å, (1:1-*Pmn2*₁); $a = 23.1432$ Å, $b = 4.1104$ Å, $c = 4.5344$ Å, (2:2-*Pm*); and $a = 34.6994$ Å, $b = 4.1111$ Å, c

= 4.5378 Å, (3:3- $Pmn2_1$). These data are presented below in Table 4.1 with the previous lattice parameters and space groups.

	$a / \text{Å}$	$b / \text{Å}$	$c / \text{Å}$	SG
SnS($Pnma$)	11.4455	4.0240	4.4481	$Pnma$
SnSe	11.7834	4.2054	4.5638	$Pnma$
SnS($Cmcm$)	11.8044*	4.1187*	4.1166*	$Cmcm$
1:1	11.6023	4.1105	4.5357	$Pmn2_1$
2:2	23.1432 (11.5716**)	4.1104	4.5344	Pm
3:3	34.6994 (11.5665**)	4.1111	4.5378	$Pmn2_1$

Table 4.1: Cell lengths and resultant space groups of the uniformly interlayered structures, with the previous calculated structures shown for comparison

* $Cmcm$ axes represented as orthorhombic and aligned to the $Pnma$ axis directions

**2:2 and 3:3 relative a axis lengths

If the averaged interlayer cell length of SnS and SnSe is given as $a_0 = 11.6089 \text{ Å}$, the ratios of a/a_0 are 0.9994 for 1:1- $Pmn2_1$, 1.9936 for 2:2- Pm and 2.9890 for 3:3- $Pmn2_1$, showing good retention of the cross-layer length. The axial ratios can also be compared to the base materials: for 1:1- $Pmn2_1$ $b/a = 0.35$ and $c/a = 0.39$; for 2:2- Pm $b/(a/2) = 0.36$ and $c/(a/2) = 0.39$; and for 3:3- $Pmn2_1$ $b/(a/3) = 0.36$ and $c/(a/3) = 0.39$. These are comparable to $b/a = 0.35$ and $c/a = 0.39$ for SnS, and $b/a = 0.36$ and $c/a = 0.39$ for SnSe.

The electronic band structures of the layered structures (Fig. 4.2) all show strong similarities to the SnS and SnSe band structures along the highest valence and lowest conduction band, retaining the two valence band maxima and two conduction band minima in the Y- Γ -Z pathway and the deep well formed by the valence band along the U-R-T-Z pathway. There is also a separation of bands at the S and R points, shown most clearly in 1:1- $Pmn2_1$, and a separation along the X-S path in the top valence band. As the layer thickness increases, a new conduction band minimum is also formed along the X-S path reaching the level of the global conduction band minimum in the 3:3- $Pmn2_1$ structure.

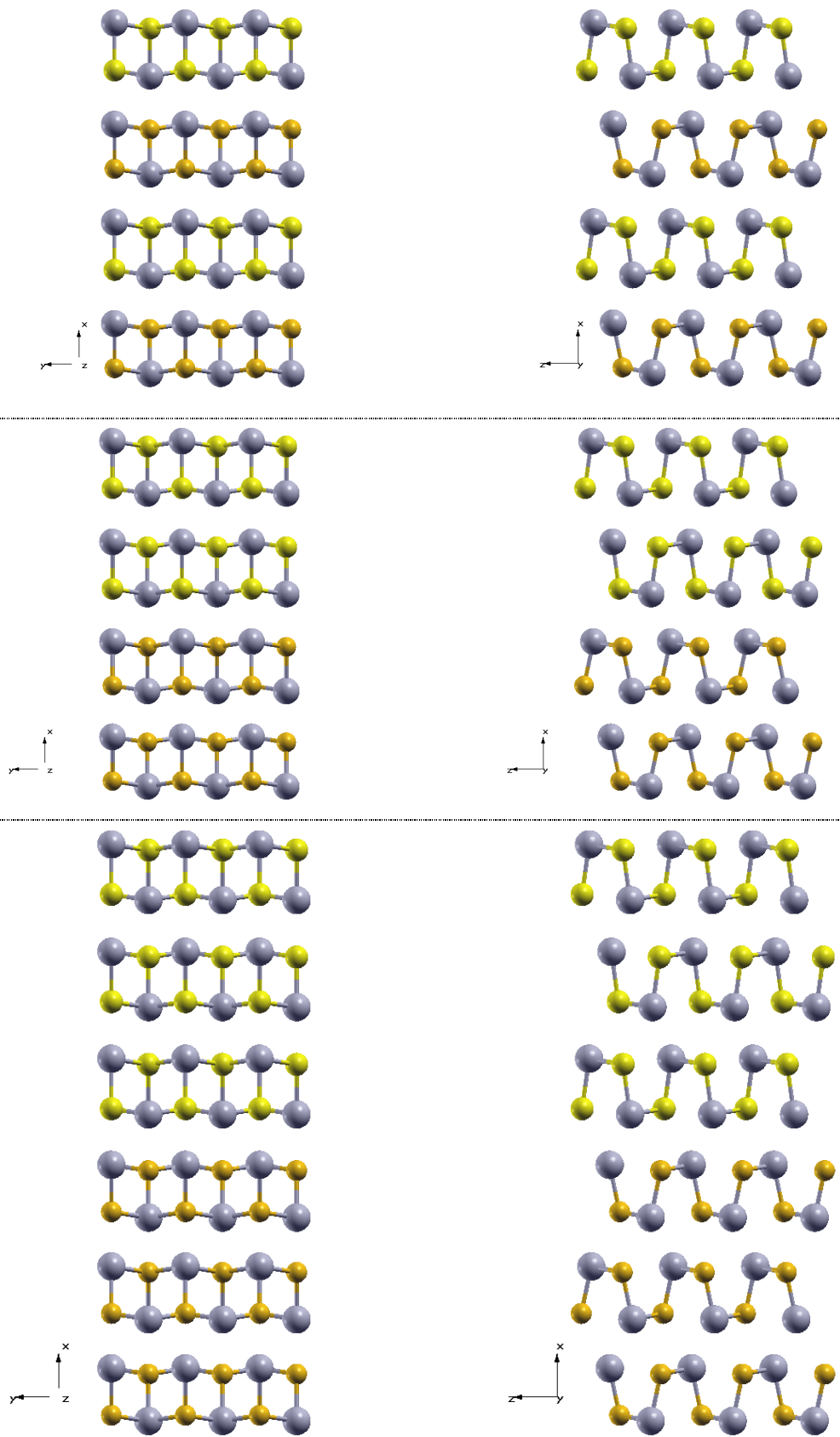


Figure 4.1: The layered structures viewed along the c (left) and b (right) axes.
 1:1- $Pmn2_1$ (above), 2:2- Pm (middle), and 3:3- $Pmn2_1$ (below)

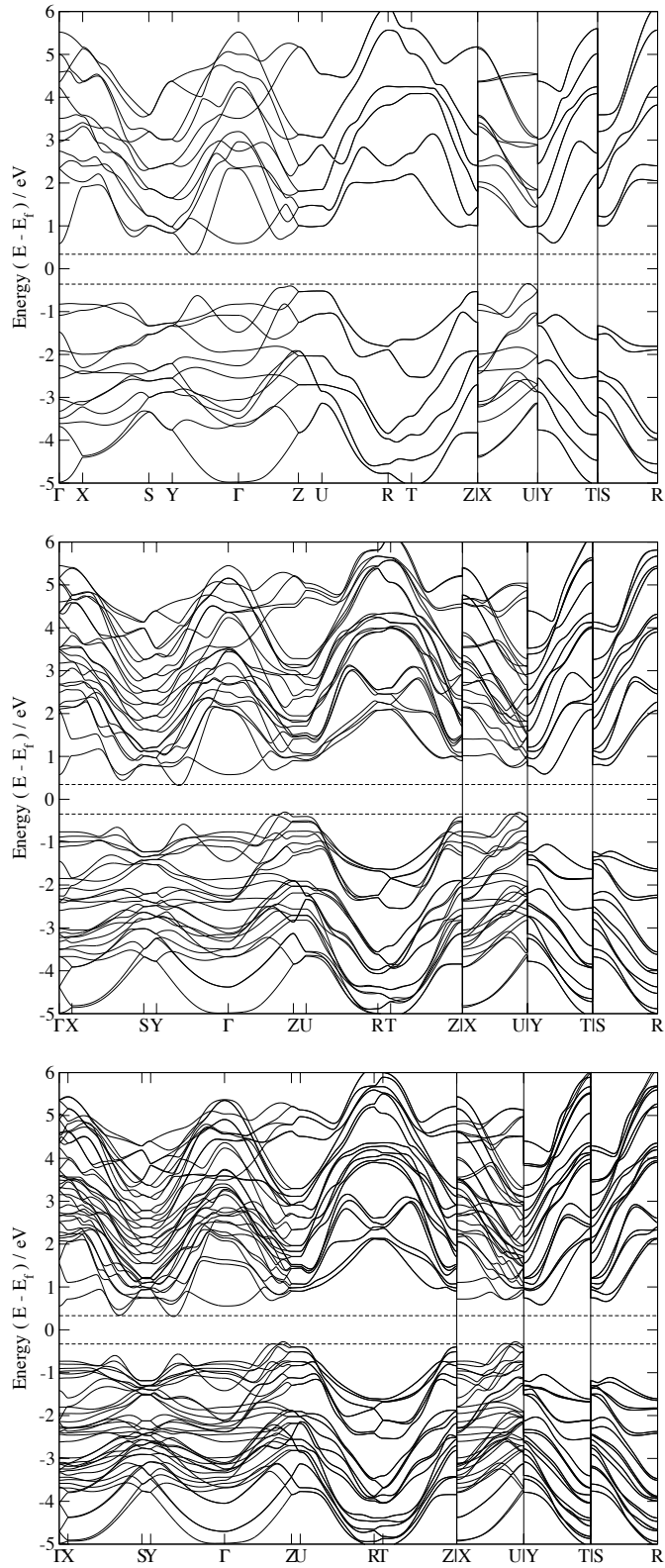


Figure 4.2: 1:1- $Pmn2_1$ (above), 2:2- Pm (middle) and 3:3- $Pmn2_1$ (below) electronic band structures calculated with Wannier90

The direct band gaps are 1.14 eV for 1:1- $Pmn2_1$, 1.07 eV for 2:2- Pm and 1.03 eV for 3:3- $Pmn2_1$. The indirect band gaps are 0.73 eV for 1:1- $Pmn2_1$, 0.69 eV for 2:2- Pm and 0.66 eV for 3:3- $Pmn2_1$. With the exclusion of the 1:1- $Pmn2_1$ direct band gap, these all show the mixed nature of the interlayered structures, with band gaps between those of $Pnma$ -SnS (1.08 eV direct and 0.95 eV indirect) and $Pnma$ -SnSe (0.86 eV direct and 0.61 eV indirect).

BoltzWann

The Seebeck tensor and the electronic conductivity tensor were calculated from the BoltzWann module of Wannier90 using the semiclassical Boltzmann transport equation and plotted in Fig. 4.3. These data showed a greater axial anisotropy than the $Pnma$ structures. The Seebeck coefficient showed a trend to more negative values in the a axis compared to the b and c axes, indicating a stronger n -type nature. The Seebeck coefficients also exhibited a split in the μ value corresponding to a doping shift, a visual leftwards shift in the curve. This leads to a more n -type intrinsic Seebeck coefficient in the a axis, and p -type in the b and c axes. This shift shows strong similarities to the $Cmcm$ -SnS electronic data, indicating the layered structures are taking an electronic structure more in line with a $Pnma/Cmcm$ intermediate.

Regarding the magnitude of the curves, the Seebeck coefficients of the 1:1- $Pmn2_1$ structure were 1033, 1183 and 1164 $\mu\text{V/K}$ in the p -doping region along the x, y and z axes, and -832, -818 and -823 $\mu\text{V/K}$ in the n -doping region, for 2:2- Pm , the Seebeck maxima were 927, 1061 and 1023 in the p -doping region and -1134, -986 and -1000 in the n -doping region, and for 3:3- $Pmn2_1$ the Seebeck maxima were 868, 1003 and 966 $\mu\text{V/K}$ in the p -doping region and -1062, -938 and -950 $\mu\text{V/K}$ in the n -doping region. These values showed large reduction from the $Pnma$ -SnS Seebeck coefficients ($S_{\text{max}} \approx \pm 1500 \mu\text{V/K}$) but were comparable to the $Pnma$ -SnSe values ($S_{\text{max}} \approx \pm 1000 \mu\text{V/K}$). The electrical conductivity minima in the 1:1- $Pmn2_1$ structure were 180, 1347 and 1101 $\mu\text{S/cm}$ in the x, y and z axes respectively, in the 2:2- Pm the electrical conductivity minima were 284, 4250 and 3459 $\mu\text{S/cm}$, and in 3:3- $Pmn2_1$ the minima were 131, 7725 and 6708 $\mu\text{S/cm}$. These electrical conductivity minima were far larger than $Pnma$ -SnS ($\sigma_{\text{min}} = 3\text{-}10 \mu\text{S/cm}$) and whilst smaller than the $Pnma$ -SnSe x direction minima ($\sigma_{\text{min}}(x) = 1349 \mu\text{S/cm}$), they were far larger in the b and c axes for the 2:2- Pm and 3:3- $Pmn2_1$ structures than the $Pnma$ -SnSe minima along these directions ($\sigma_{\text{min}}(yz) \approx 3500 \mu\text{S/cm}$).

However, it is noted that the electronic conductivities show less smooth curves near the top of their values when compared to the $Pnma$ structures, resulting in less steep ascent of the

electronic conductivity from the Fermi level and ultimately harming the electronic suitability in these regions

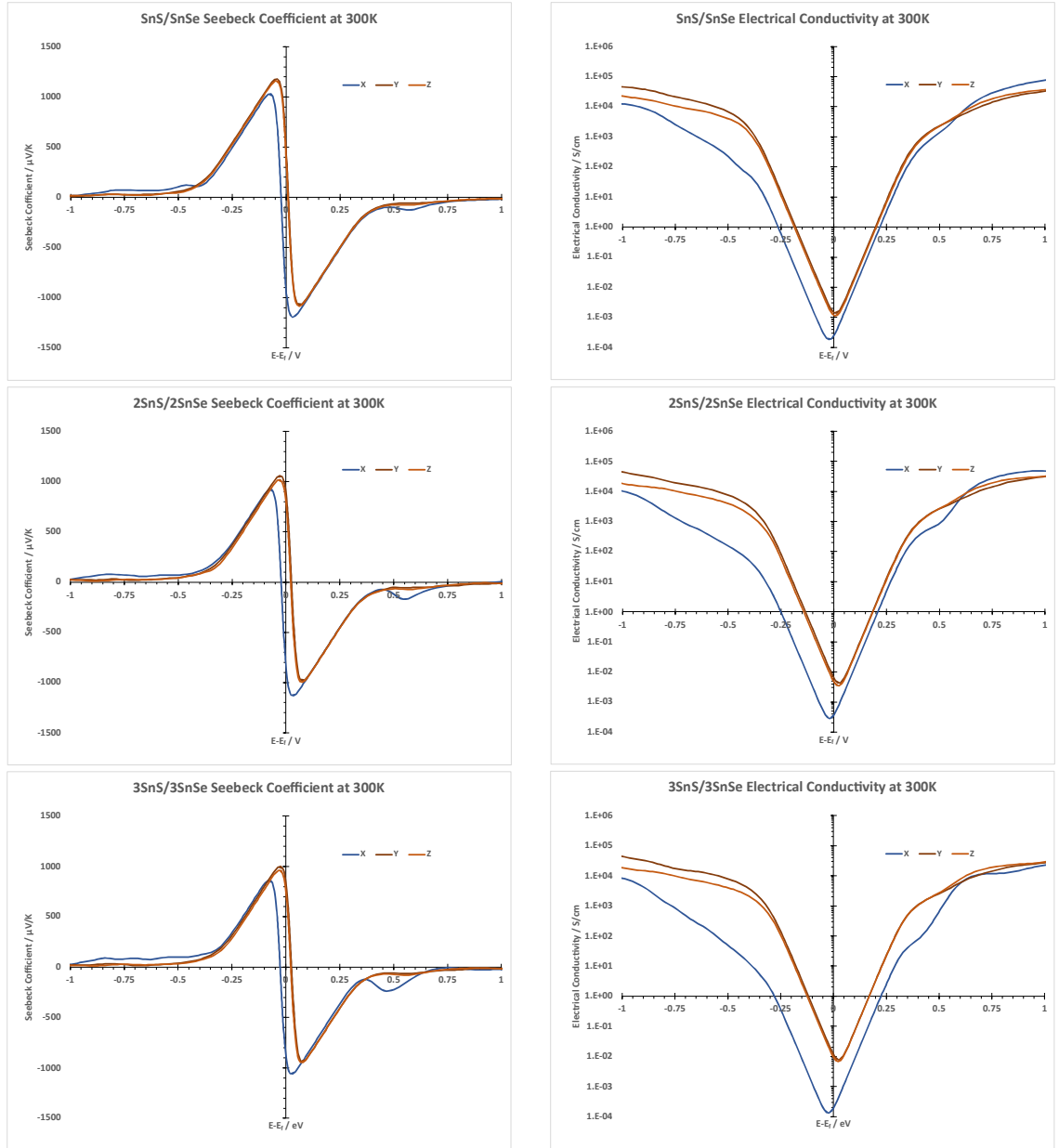


Figure 4.3: 1:1- $Pmn2_1$ (top), 2:2- Pm (middle) and 3:3- $Pmn2_1$ (bottom) Seebeck Coefficient and Electrical Conductivity across μ values ± 1 eV from the Fermi level at 300 K.

Power Factors

The power factors of the layered compounds are shown in Fig. 4.9, along with the *Pnma* structures for comparison. These plots indicate a lowering in the *p*-type electrical suitability of the layered materials, but the *n*-type electrical suitability remains at similar levels to the *Pnma*-SnS and SnSe structures.

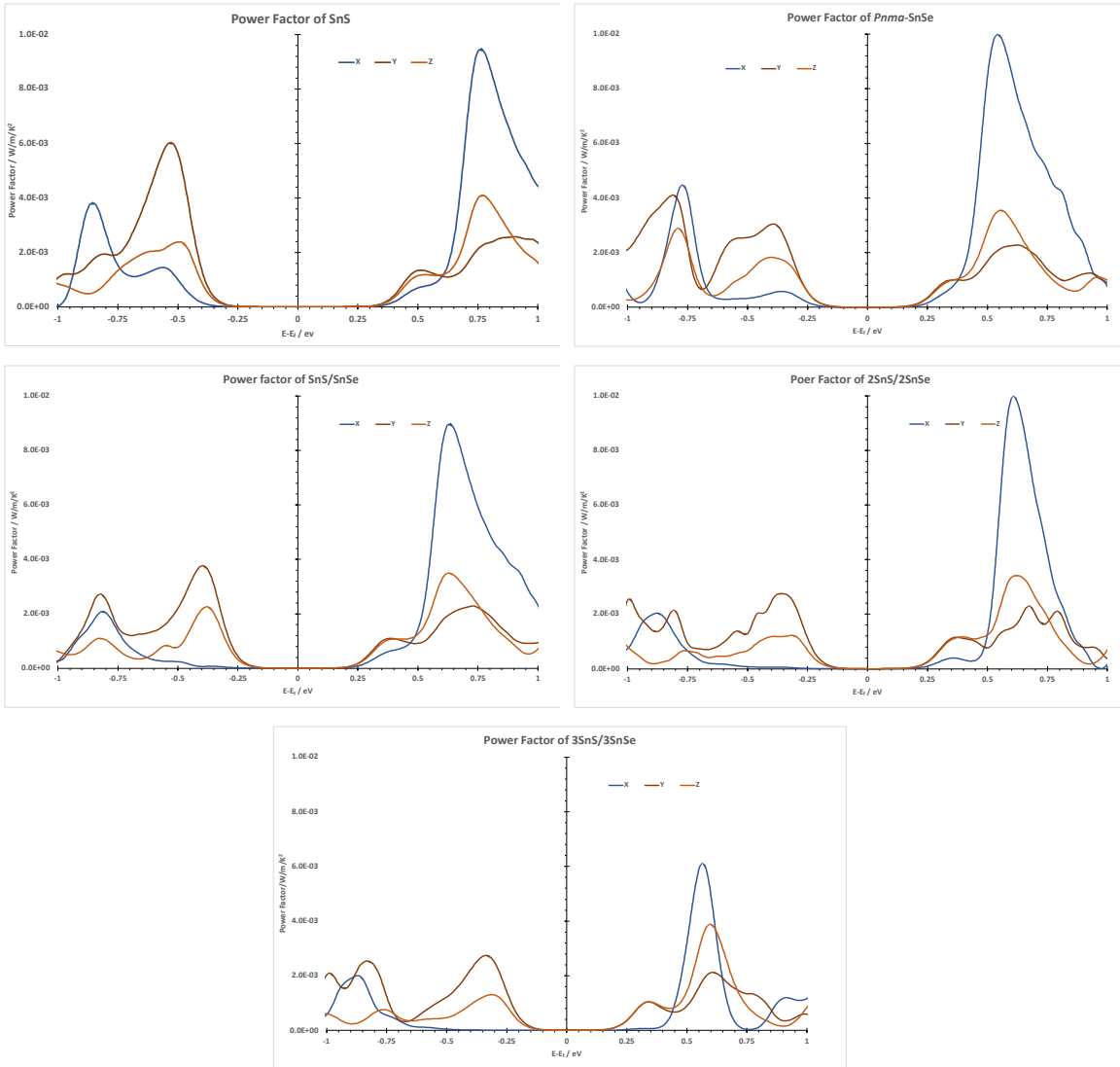


Figure 4.9: The Power Factors of *Pmna*-SnS (upper left), *Pnma*-SnSe (upper right), 1:1-*Pmn2*₁ (middle left), 2:2-*Pm* (middle right), and 3:3-*Pmn2*₁ (lower middle) across the chemical potential range $E_f \pm 1$

4.1.2 - Phononic Properties

Characterisation

Using the xTB methodology within CP2K, the relaxed structures were obtained, with lattice parameters of $a = 10.5555 \text{ \AA}$, $b = 3.8734 \text{ \AA}$, $c = 3.8211$ for 1:1-*Pmn2*₁; $a = 21.1558 \text{ \AA}$, $b = 3.8688 \text{ \AA}$, $c = 3.8239$ for 2:2-*Pm*; and $a = 31.7481 \text{ \AA}$, $b = 3.8683 \text{ \AA}$, $c = 3.8227$ for 3:3-*Pmn2*₁. As with the *Pnma* structures, these are shorter cell lengths than the QE relaxed lengths, and showed a slight flip in lengths of the b and c axes. This can be seen as an effect of the axial strain produced by the interlayering scheme which restricts the zig-zag nature of the c axis, and bringing the layer closer to a *Cmcm*-like configuration, which also shows lower c (*Pnma*-b) axis lengths than b (*Pnma*-c) when relaxed through CP2K. Whilst this axis length flip is not seen in the relaxed cell parameters of the QE structures, the significant enhancement of the electrical conductivities could be an indication of this process as it aligns with the very high electronic conductivity of the *Cmcm* phase, and previous QE should not be seen as the definitively “true” method, as calculations on interlayering of SnS and SnS₂ have indicated that tight binding better estimates the band gap of the SnS and SnS₂ bulk structures^[5].

Phonon Dispersion

The phonon dispersion spectra show the characteristic properties established in the *Pnma*-SnS and *Pnma*-SnSe spectra, including the linear dispersion of phonon bands along the Γ -X, Γ -Y and Γ -Z paths, with less linearity in the larger supercells as the increased number of atoms in the unit cell introduce more phonon bands below the main branch. The low frequency points along the Cartesian directions are also lowered in the larger structures, with values of 0.4475, 1.0395 and 0.9185 THz for the X, Y and Z points of 1:1-*Pmn2*₁, 0.2445, 0.8920 and 0.7834 THz for 2:2-*Pm*, and 0.1448, 0.7495 and 0.6948 THz for 3:3-*Pmn2*₁, showing strong phonon mode softening from the layering motifs. Each structure also shows no clear band gap, as the *Pnma*-SnSe optical band takes its place within the band gap of the *Pnma*-SnS.

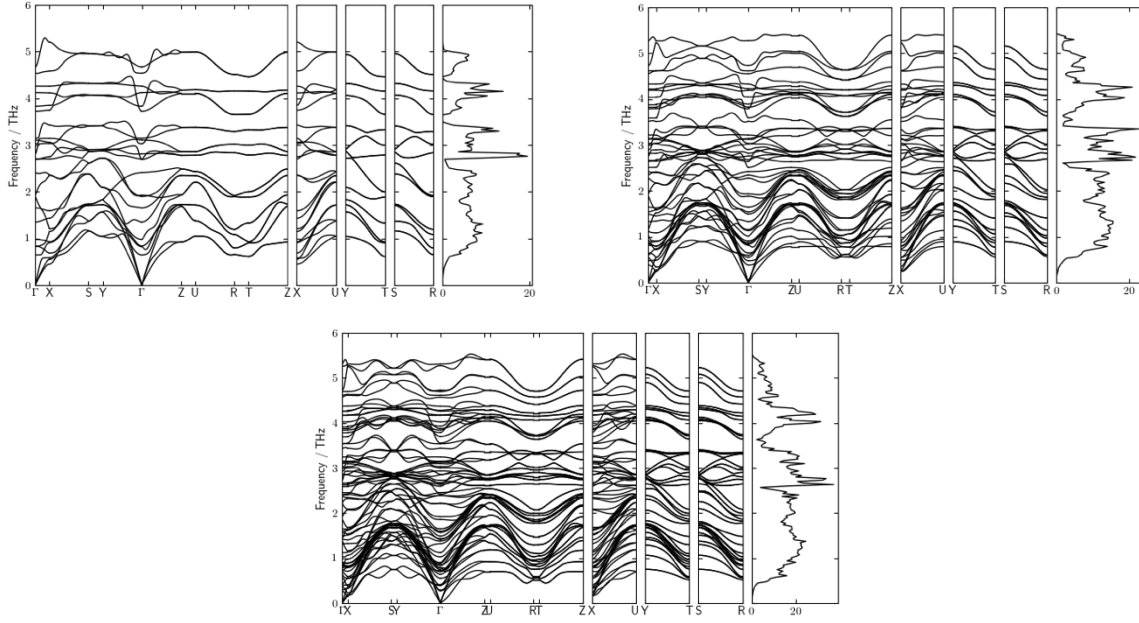


Figure 4.4: Phonon dispersion spectra given in THz, calculated through Phonopy using CP2K/xTB for force calculation, for 1:1- $Pmn2_1$ (upper left) 2:2- Pm (upper right) and 3:3- $Pmn2_1$ (lower middle)

Lattice Thermal Conductivity

As the unit cell increases, the computational demand for the force calculation on the unit cell significantly increases. As such, the supercell sizes were adjusted for the 2:2- Pm and 3:3- $Pmn2_1$ lattice thermal conductivity calculations in line with their unit cell enlargement. 1:1- $Pmn2_1$ was calculated on a 3x3x3 supercell with a 4x8x8 supercell for second order interactions, as with the $Pnma$ structures, but the 2:2- Pm supercell sizes were reduced to 2x3x3 and 3x6x6 for third and second order interactions, and the 3:3- $Pmn2_1$ was reduced further to 1x3x3 and for third order interactions and 2x4x4 for the second. The choice of the second order supercell size in 3:3- $Pmn2_1$ was such that the a-axis was still increased from the third order, but the b- and c-axes increased less than in the other structures, such that the computational cost was still in a reasonable range.

The lattice thermal conductivity values of the 1:1- $Pmn2_1$ layered material at 300K are 0.3466, 0.9102 and 0.7630 W/m/K, with an averaged isotropic lattice thermal conductivity of 0.6733 W/m/K. These values are lowered from $Pnma$ -SnS, but notably higher than $Pnma$ -SnSe (0.3374, 0.7726 and 0.5652 W/m/K). The lattice thermal conductivity values of the 2:2- Pm layered material at 300K are 0.2257, 0.7180 and 0.5945 W/m/K, with an averaged isotropic lattice thermal conductivity of 0.5127 W/m/K. And the lattice thermal conductivity values of the 3:3- $Pmn2_1$ layered material at 300K are 0.1371, 0.5969 and 0.5091 W/m/K,

with an averaged isotropic lattice thermal conductivity of 0.4144 W/m/K. The 2:2-*Pm* and 3:3-*Pmn*₂ lattice thermal conductivity values are greatly reduced from the SnS and the SnSe, and are a strong indication of the validity of the interlayering approach in disrupting the heat transport across the material, and the trend of decreasing thermal conductivity as the layer thickness increases shows that there is a balance to be found, rather than simply aiming for the thinnest layers possible.

These lattice thermal conductivities place amongst the lowest seen in recent literature, comparable to other computational work from 0.13 to 0.17 W/m/K at 300 K^[6, 7, 8], and below recent experimental measurements of low lattice thermal conductivity materials of 0.19 W/m/K at 300 K^[9].

These sandwiched structures also show a greater degree of anisotropy in the lattice thermal conductivities of the cross-layer to intralayer average ratio. Where *Pnma*-SnS had a ratio of 0.45 and *Pnma*-SnSe had a ratio of 0.50, the layered species have ratios of 0.41, 0.27 and 0.25, for 1:1-*Pmn*₂, 2:2-*Pm* and 3:3-*Pmn*₂ respectively. This is expected to some extent, as the layering would undoubtedly affect the cross-layer direction to a greater degree than the intralayer, but the effect on the intralayer lattice thermal conductivity is not insignificant and the more *Cmcm*-like nature of the layers is clearly influencing the heat transport along these axes, with the reduction of all three axial lattice thermal conductivities. This can be explained by the strain imposed on the intralayer bonding by the cross-layer interactions, and this effect can be seen in conjunction with the dramatic increase seen in the electrical conductivities along the b and c axes of the 2:2-*Pm* and 3:3-*Pmn*₂ as a further reinforcement of the systems movement to a more symmetric in-layer motif. However the low *a*/(*bc*) ratio of the 1:1-*Pmn*₂ indicate the ineffectiveness of single layers in disrupting phonon transport through the layers or affecting the in-layer structure to the extent that the thicker layering is shown to.

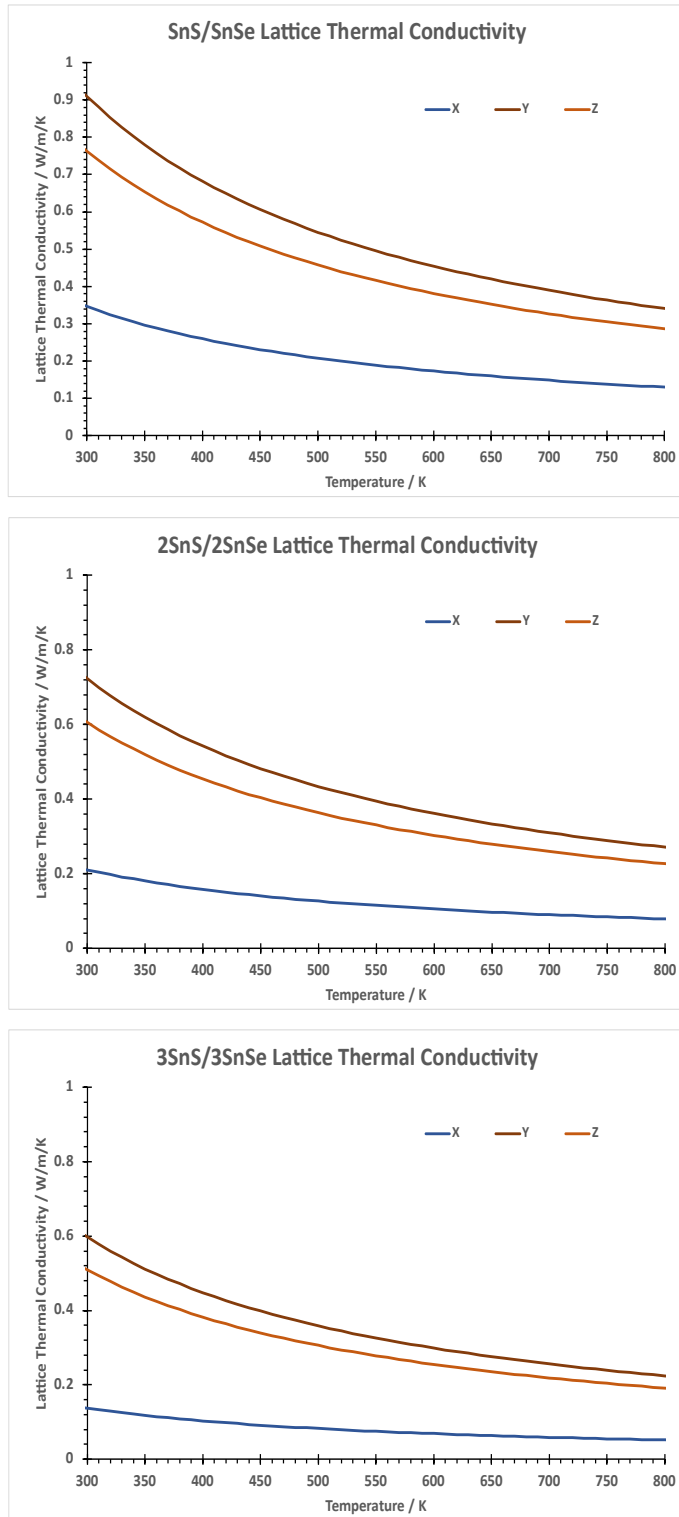


Figure 4.5: Lattice thermal conductivity, κ_{latt} , along the a , b and c axes as a function of temperature for 1:1- $Pmn2_1$ (top), 2:2- Pm (middle) and 3:3- $Pmn2_1$ (bottom)

The lattice thermal conductivities are shown with the *Pnma*-SnS and *Pnma*-SnSe structures in Fig. 4.6, separated into the cross-layer direction and the averaged intralayer direction. The 1:1-*Pmn2*₁ follows a very similar path to SnSe in the layering direction as the temperature increases but shows a larger lattice thermal conductivity across the range in the intralayer direction. This indicates that at such low layer thickness the boundary scattering is ineffective, and the structural changes have an adverse effect upon the phonon disruption within the layers, facilitating the heat transport. The 2:2-*Pm* and 3:3-*Pmn2*₁ structures, however, show significant reductions in the layered direction's lattice thermal conductivity, where the added homologue boundaries have successfully disrupted the phonon pathways and reduced movement of heat carriers. There is also a decrease in the lattice thermal conductivity in the intralayer direction, albeit less dramatically.

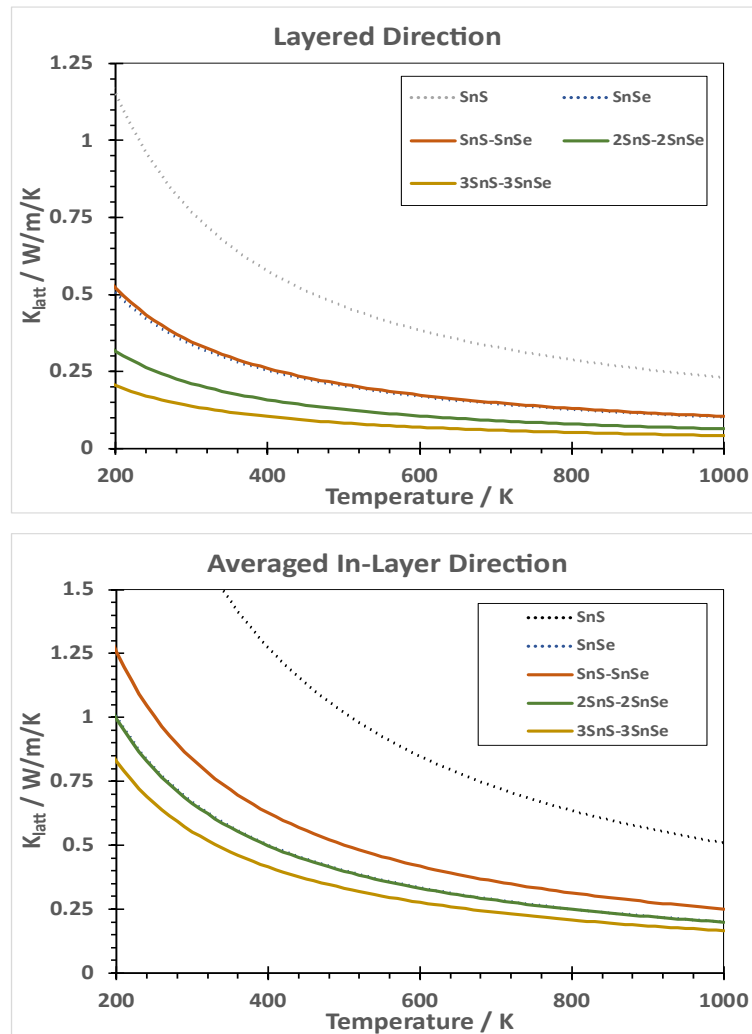


Figure 4.6: The lattice thermal conductivities of the layered direction, *a* (above), and the averaged intralayer direction, *b* and *c* in *Pnma* (below)

Phonon Lifetimes

As with the *Pnma* and *Cmcm* structures, the phonon lifetimes of the mode frequencies were evaluated. These all showed similarly low lifetimes at low temperatures when compared to the *Pnma* lifetime plots, and a slight decrease in the lowest edge can be seen as you move from 1:1-*Pmn2₁* to 2:2-*Pm* to 3:3-*Pmn2₁*, indicating the further lowering of the lifetimes of the low-frequency phonon modes through phonon scattering.

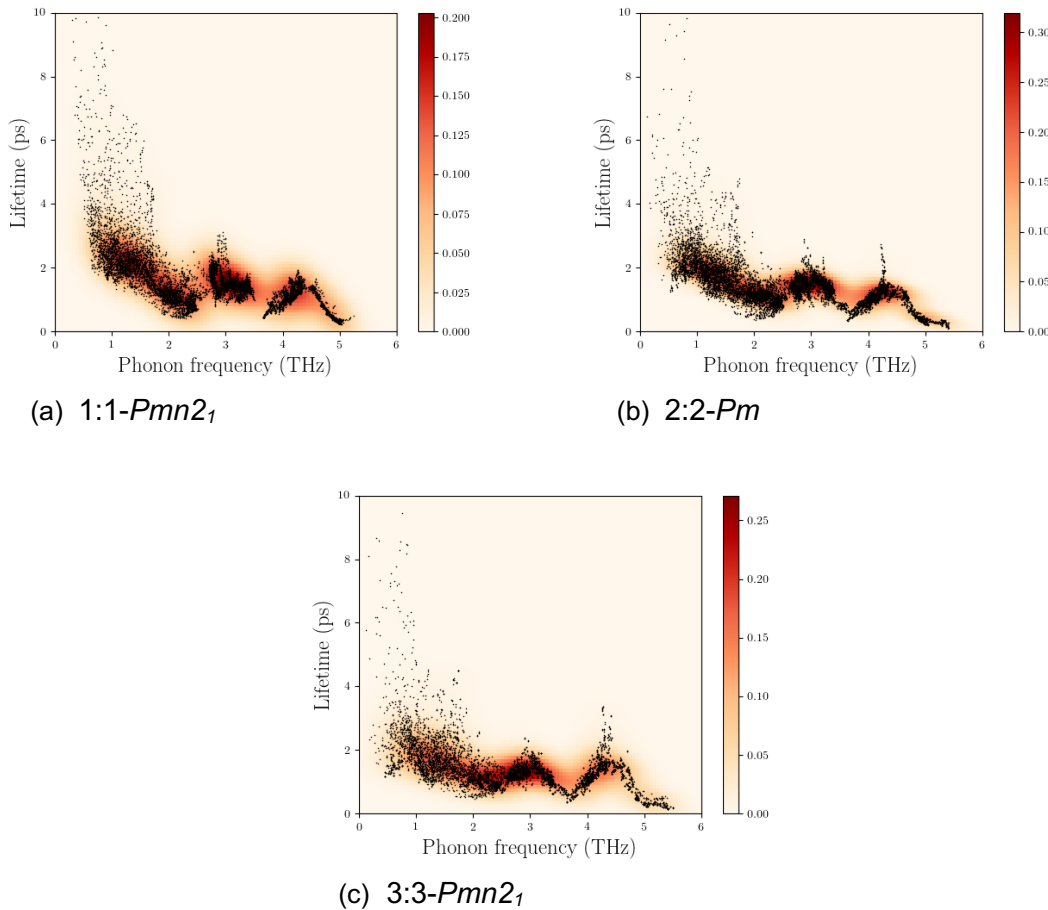
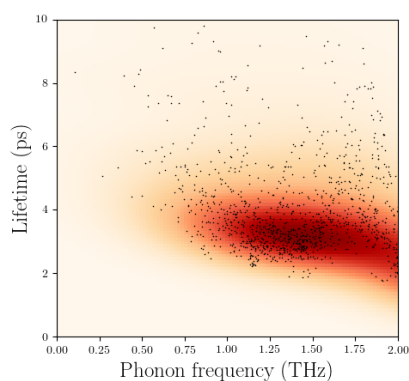


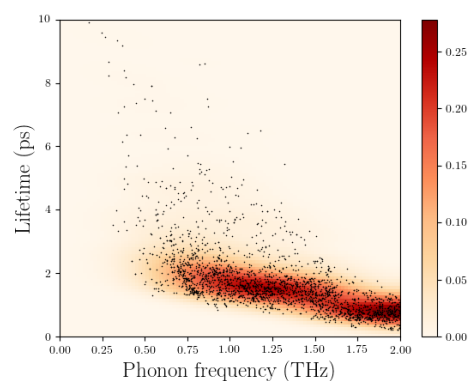
Figure 4.7: The lifetimes of phonons by phonon mode frequency for 1:1-*Pmn2₁* (upper left) and 2:2-*Pm* (upper right) and 3:3-*Pmn2₁*. The heatmap indicates regions of greater concentration of phonon modes. Note the lower maximum y-axis (10 ps) compared to the *Pnma* and *Cmcm* plots (20 ps) in Figures 3.9 and 3.18.

In Fig. 4.8, the phonon lifetimes of the low frequency modes (below 2 THz) are plotted alongside the low frequency modes of *Pnma*-SnS and SnSe. The closer images in the low frequency region show the sequence of lattice thermal conductivity much more clearly,

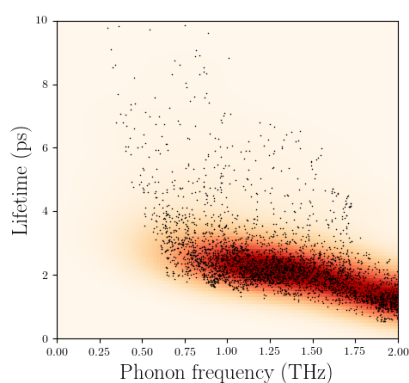
with *Pnma*-SnS having the more obvious higher and more spread phonon lifetimes, 1:1-*Pmn2₁* showing lifetimes falling in between the *Pnma* phases slightly above *Pnma*-SnSe, and 2:2-*Pm* and 3:3-*Pmn2₁* having the lowest phonon lifetimes.



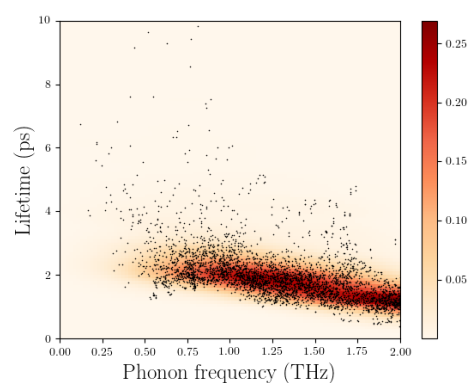
(a) *Pnma*-SnS



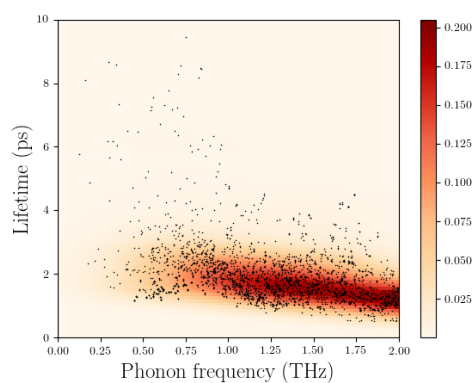
(b) *Pnma*-SnSe



(c) 1:1-*Pmn2₁*



(d) 2:2-*Pm*



(e) 3:3-*Pmn2₁*

Figure 4.8: Phonon lifetimes of (a) *Pnma*-SnS, (b) *Pnma*-SnSe, (c) 1:1-*Pmn2₁*, (d) 2:2-*Pm* and (e) 3:3-*Pmn2₁*

Phonon Mean Free Paths

The phonon mode contribution to lattice thermal conductivity by mean free path showed the significant reduction of long-range phonon modes in the transport of heat through the layered axis of the layered materials, as seen in Fig. 4.9. This effect is shown in the 1:1- $Pmn2_1$ structure in the reduction of the broad, long-range peak exhibited by $Pnma$ -SnS, but larger contributions are shown when compared to the $Pnma$ -SnSe curve above 15 Å, showing the ineffectiveness of single layers in significant boundary scattering. The 2:2- Pm and 3:3- $Pmn2_1$ structures also show reduction even below that of $Pnma$ -SnSe, however with all mean free path lengths showing smaller contributions. This reduction in the contributions of long mean free path phonons give strong evidence of the layering effect on the lattice, with the boundary scattering clearly effective in reducing heat transport across the boundaries created by the interlayered regions.

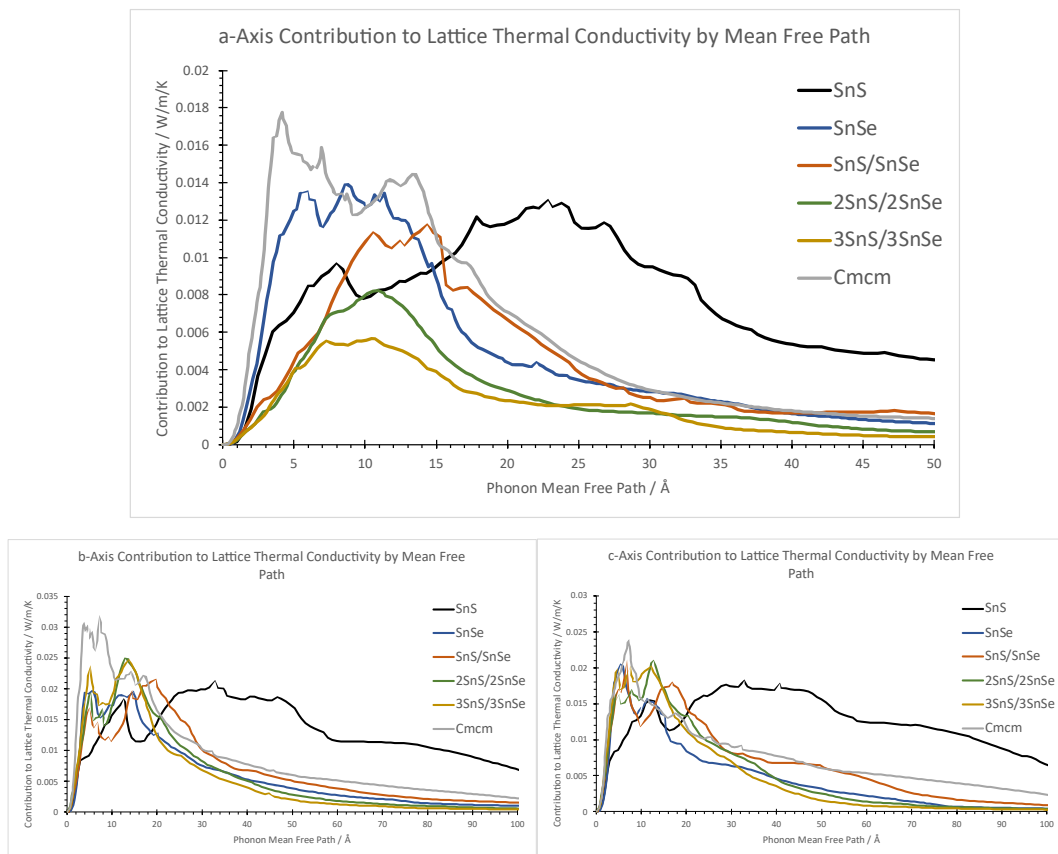


Figure 4.9: The phonon contribution to the lattice thermal conductivity at 300 K by their mean free path

The intra-layer directions also show reduced lattice thermal conductivity contributions from high mean free path phonon modes with respect to the *Pnma*-SnS and resulted in curves closer to *Pnma*-SnSe with only slightly decreased contributions in the long-range phonon modes, shown clearest in the 35-80 Å region. Whilst this could be enough to account for the relatively minor reduction in the c axis lattice thermal conductivity, the reduction in the b axis was somewhat larger. It can therefore be assumed that this reduction does not come solely through the scattering of long-range phonons as seen in the cross-layering direction.

The fact that the mean free path is only a partial explanation of the decrease in lattice thermal conductivity is seen in Fig. 4.10, where the mean free path values corresponding to the largest contribution to the cross-layer (*Pnma*-a, *Cmcm*-b) lattice thermal conductivity are plotted for each system and compared to the full lattice thermal conductivities of these directions. These are ordered such that the mean free path increases from left to right, and shows the 2:2-*Pm* and 3:3-*Pmn*2₁ sitting in a central position, rather than at the lowest mean free paths end.

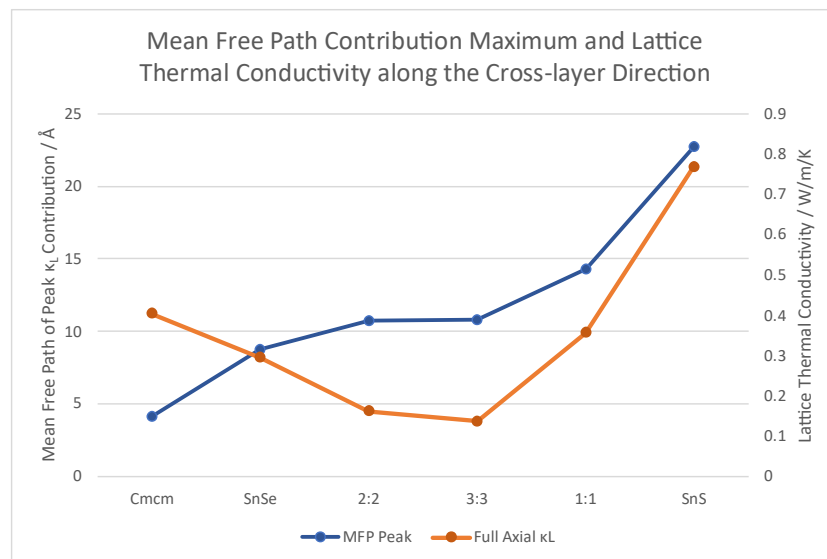


Figure 4.10: The mean free path values corresponding to the maximum contribution to the cross-layer lattice thermal conductivity, shown alongside the full lattice thermal conductivity for the cross-layer axis.

Also of note in the layered axis mean free path contributions (Fig. 4.9) is the lowering of low mean free path contributions, which would not be expected from scattering effects alone.

All three interlayered materials showed similar linearity in their mean free path contributions from 0-5 Å, with more gradual slopes than those of *Pnma*-SnS, *Pnma*-SnSe and *Cmcm*-SnS, in a region where boundary scattering is notably less effective.

Phonon Group Velocities

This effect can be attributed to the softer phonon modes present along the Γ -X pathway, resulting in lower phonon group velocities as seen in Fig. 4.10. All layered structures show strong reduction in group velocities in the layered direction compared to *Pnma*-SnS and *Pnma*-SnSe. There is also shown a slight decrease in group velocities of the interlayered structures along the *Pnma* *b* axis compared to *Pnma*-SnSe, which can explain the drop in lattice thermal conductivity along that axis. The *Pnma* *c* axis direction does not show a similar lowering of the group velocities, where the lattice thermal conductivity reduction is small and can be explained solely by the small mean free path contribution reduction alone.

From the phonon mean free paths, phonon lifetimes and phonon group velocities, a strong picture can be built as to the effect of the interlayering of SnS and SnSe, providing both extrinsic scattering effects and intrinsic phonon mode softening effects.

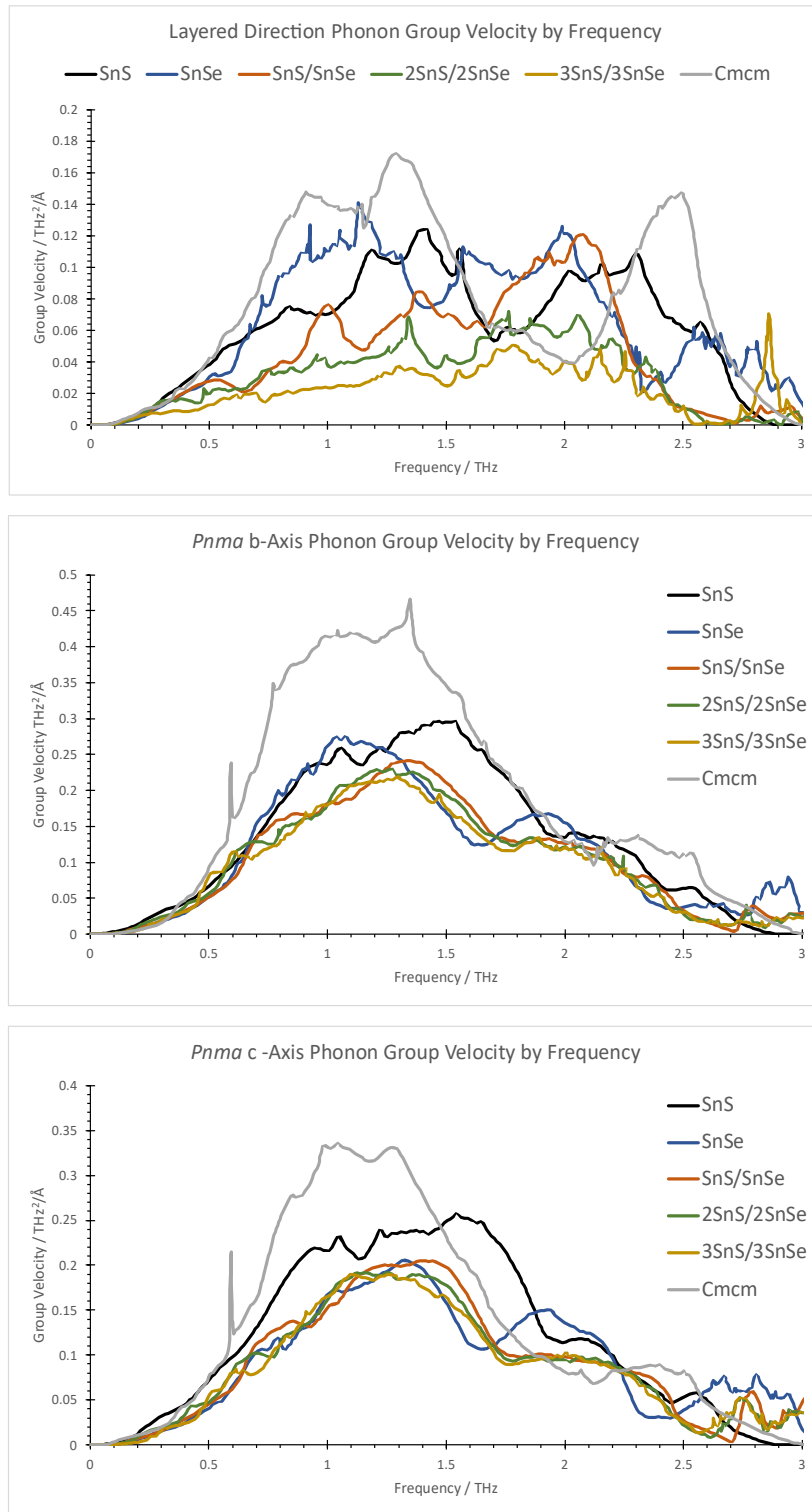


Figure 4.10: Group velocities of acoustic phonons along the layered direction (above), *Pnma*-b/*Cmcm*-c axis (middle), and *Pnma*-c/*Cmcm*-a axis (below)

4.1.3 - Full Figure of Merit

The full figure of merit was obtained as with the *Pnma* and *Cmcm* structures.

At 300 K

As the layered structures have no current experimental data to align to, the relaxation times were assumed to be equal to the average relaxation time of the *Pnma* structures. As such the 300K relaxation times for 1:1-*Pmn2*₁, 2:2-*Pm*, and 3:3-*Pmn2*₁ were all assumed to be $\tau = 22.5288$ fs. This assumption could have strong effects on the obtained figure of merits if the interlayered structures are found to have relaxation times significantly deviating from this baseline, where longer relaxation times will result in generally higher figure of merits, but lower relaxation times would result in lower figure of merits. The exact determination of the relaxation times would therefore be optimal but is outside the scope of this work.

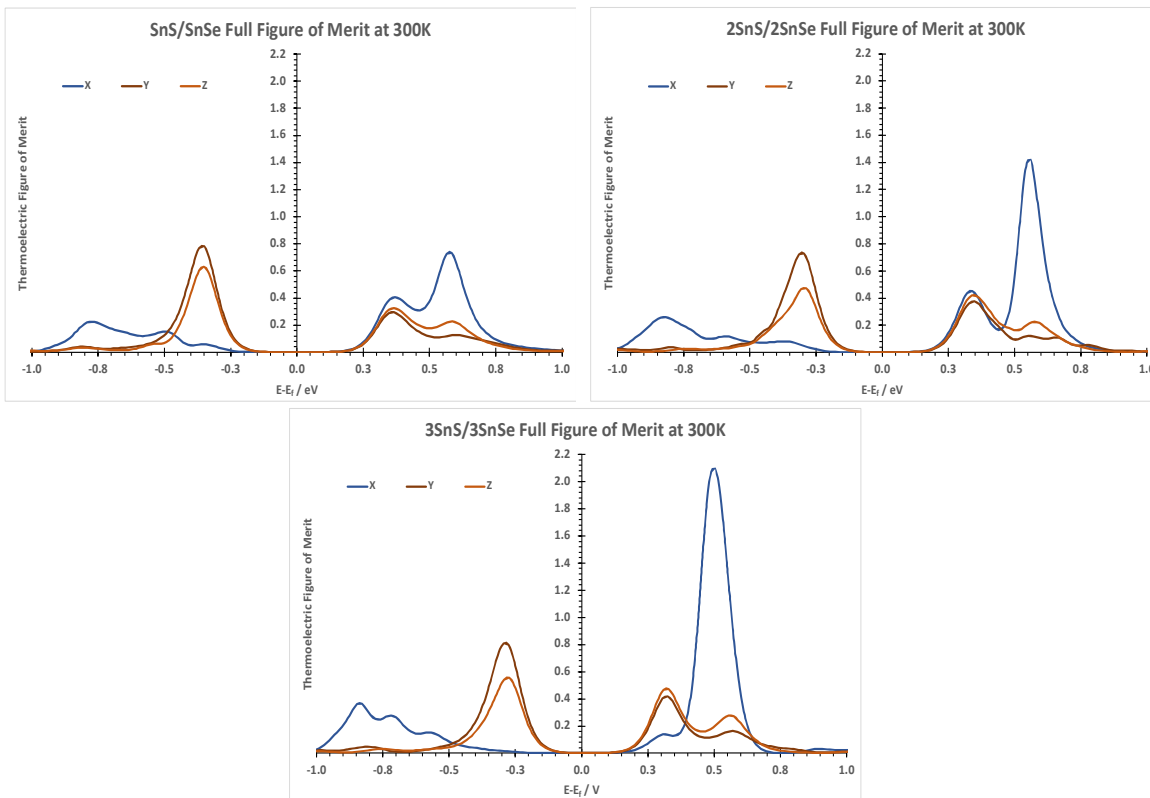


Figure 4.11: Figure of merits of 1:1-*Pmn2*₁ (upper left), 2:2-*Pm* (upper right), and 3:3-*Pmn2*₁ (lower middle) across the chemical potential range $E_f \pm 1$ eV, for each axis

Whilst the electronic conductivity was seen to be lower in the mixed layered structures compared to SnSe, the significantly lower lattice thermal conductivities allow the figure of

merits of the 2:2- Pm and 3:3- $Pmn2_1$ to reach far higher maxima in both the cross-layer and intralayer directions. The 3:3- $Pmn2_1$ a-axis figure of merit in particular showed a significant improvement, reaching a maximum of $zT = 2.1$.

At 300, 500 and 750 K

The relaxation time of these layered materials at 300 K is set to $\tau = 22.5288$ fs, at 500 K, $\tau = 9.9740$ fs, and at 750 K, $\tau = 5.2816$ fs. These are taken as the averages of the $Pnma$ -SnS and $Pnma$ -SnSe relaxation times for the given temperature, with the interlayered structure relaxation times assumed to be entirely dependent on the relaxation times of the constituent layers.

As the temperature increases from 300 K to 500 K up to 750 K, the dominance of n -type over p -type is once again enhanced in these sandwich structures. Both the 2:2- Pm and 3:3- $Pmn2_1$ show very strong figure of merit in the n -doped regions, with all structures exhibiting very similar p -doped region figures of merit. The maxima shifts towards the Fermi level at higher temperatures are still present, with the effect less pronounced in the 3:3- $Pmn2_1$ structure than the 1:1- $Pmn2_1$ or 2:2- Pm .

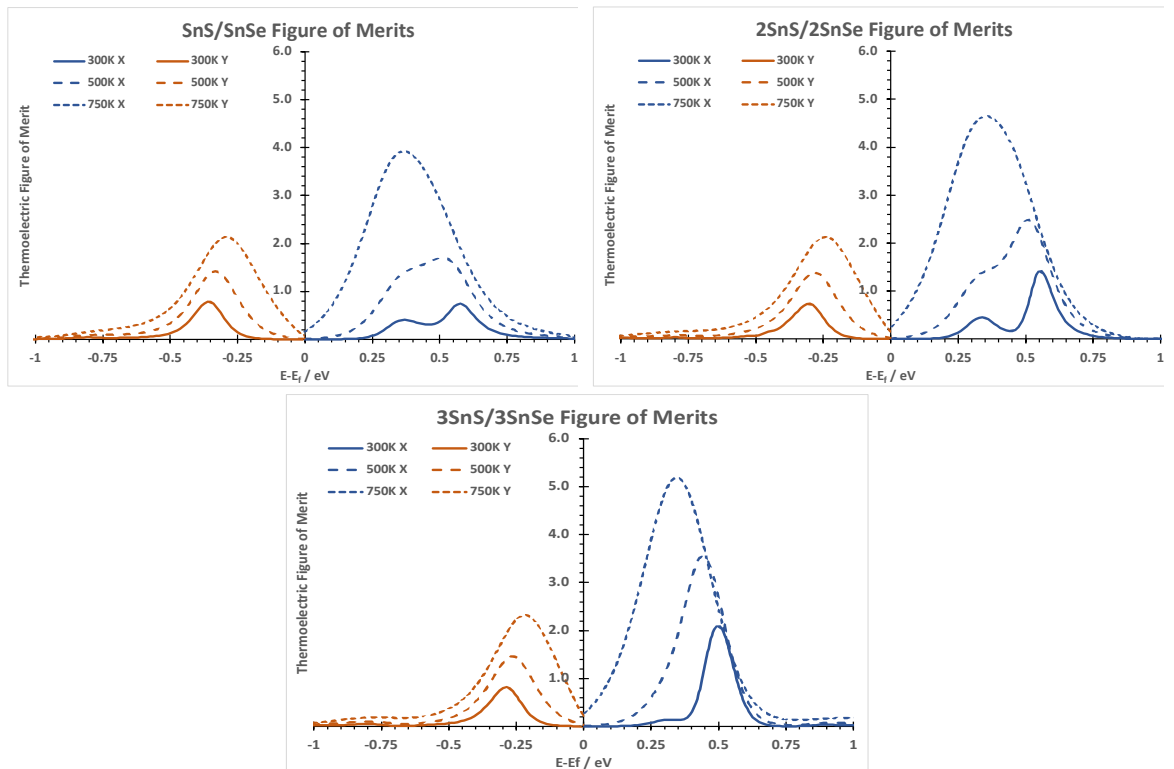


Figure 4.13: Figure of merits across chemical potentials for 300, 500 and 750 K
Y-axis values are used for below the Fermi level and X-axis values are used for above

As above, the full zT is calculated from the lattice thermal conductivities and electronic properties and plotted as a function of μ , with the strongest axes below and above the Fermi level shown at each temperature. At 300 K, the 2:2- Pm phase is shown to have a higher n -type maxima than the $Pnma$ -SnSe, and both the 1:1- $Pmn2_1$ and 2:2- Pm structures have higher p -type maxima. This improvement is lessened at higher temperatures, and at 750 K $Pnma$ -SnSe has increased above the peak of the 2:2- Pm curve. This is to be expected as the lattice thermal conductivity has a greater influence on the full thermal conductivity at low temperatures. The electronic thermal conductivity is shown to be lower at lower temperatures by the Wiedemann-Franz Law, where the electronic thermal conductivity is proportional to the temperature and electronic conductivity $\kappa_e \propto \sigma T$. The lattice thermal conductivity is conversely shown to be higher at low temperatures as seen in Fig. 4.5. These combine to give a much larger κ_L/κ_e ratio at low temperatures. Nonetheless 2:2- Pm remains competitive in both the n - and p -doping regions.

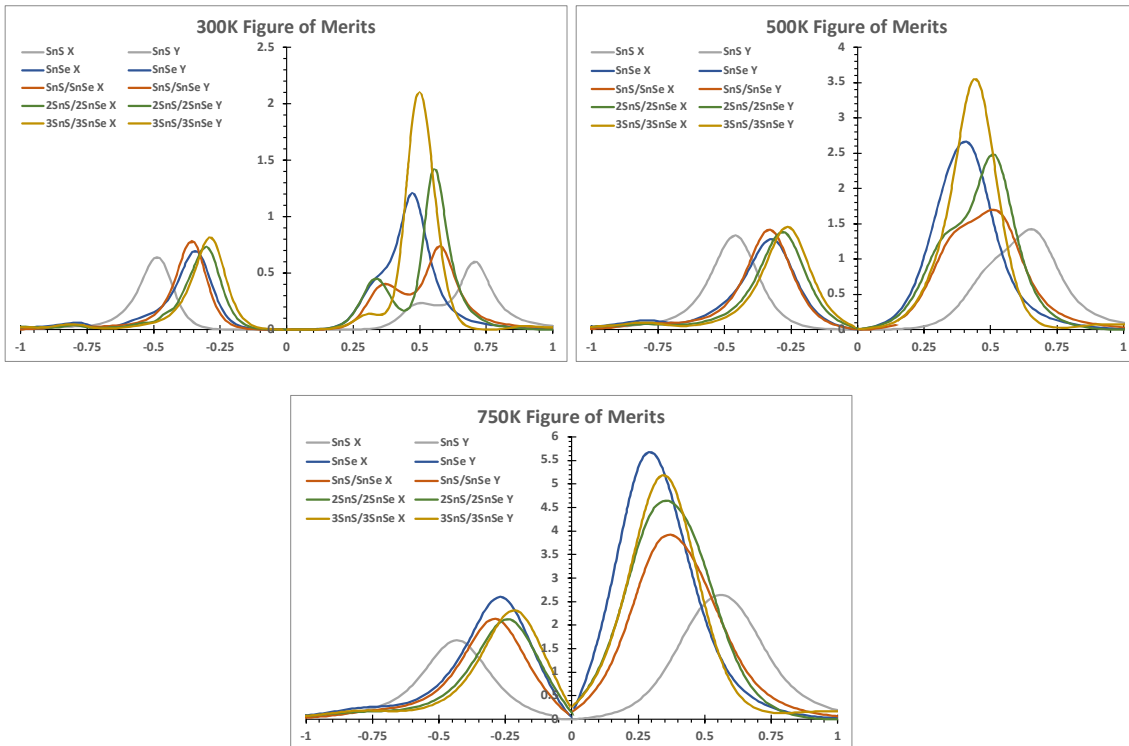


Figure 4.12: Full figure of merits of the $Pnma$ and layered materials at 300 K (upper left), 500 K (upper right) and 750 K (lower middle)

Across a Temperature Range

The figure of merits of *Pnma*-SnS, SnSe, and the layered structures are shown below, using the average values of the 300, 500 and 750 K figures of merits, shown against μ . The competitive nature of these layered materials can be seen here, with the 2:2-*Pm* *p*-doped peak close to the *Pnma*-SnSe, and the 3:3-*Pmn*2₁ peak above that of *Pnma*-SnSe in both *n*- and *p*-doping regions. As for the doping levels required to obtain these values, the *Pnma*-SnSe shows figure of merits above both the 2:2-*Pm* and the 3:3-*Pmn*2₁ figure of merits in the *n*-doping region until reaching the $E_f+0.3$ eV doping level, at which point the 3:3-*Pmn*2₁ shows larger figure of merits. However, the *p*-doping region shows figure of merits above those of *Pnma*-SnSe until $E_f-0.3$ eV, indicating a lower level of doping needed for improved thermoelectric efficiency.

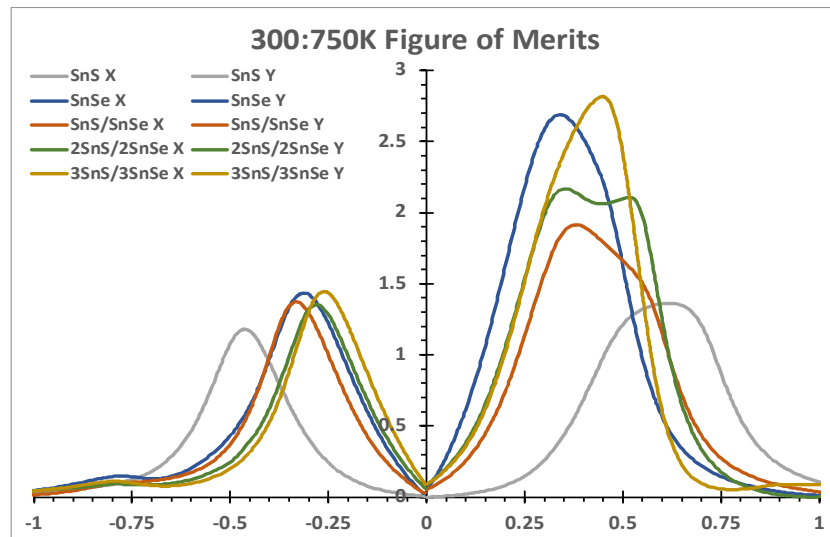


Figure 4.14: The averaged figure of merits of 300, 500 and 750 K, across the chemical potential range $E_f \pm 1$

The averaged values of the 300 K and 500 K figure of merits are shown in Fig. 4.15. This highlights the significant improvement in low-temperature thermoelectric efficiency brought by the 3:3 layering, with a significant improvement over *Pnma*-SnSe seen by a peak figure of merit 0.8 above the SnSe peak (3:3-*Pmn*2₁ 2.56, *Pnma*-SnSe 1.76). As with the 300:750K figure of merits, the *p*-doped region indicates a much lower doping level required than for *Pnma*-SnSe, as well as peak values of 1.05 and 1.12 for 2:2-*Pm* and 3:3-*Pmn*2₁ respectively, above those of *Pnma*-SnSe (0.98).

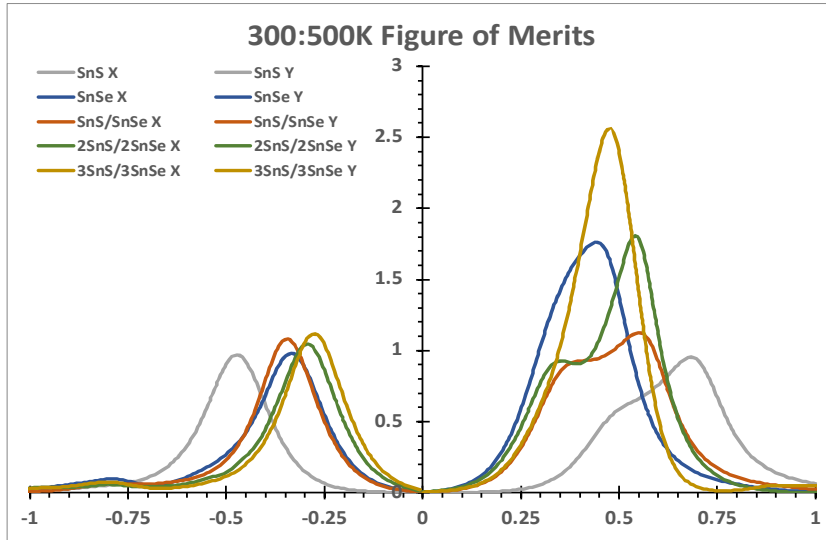


Figure 4.15: The averaged figure of merits of 300 and 500 K, across the chemical potential range $E_f \pm 1$

The peak values in each two doping regions for the structures at 300, 500 and 750 K, and for the averaged values across temperatures, are given below in Tables 4.2, 4.3, and 4.4 with the largest figure of merits in each column indicated in bold.

	300K		500K		750K	
	<i>n</i> -type	<i>p</i> -type	<i>n</i> -type	<i>p</i> -type	<i>n</i> -type	<i>p</i> -type
SnS	0.60	0.64	1.42	1.33	2.64	1.68
SnSe	1.21	0.70	2.67	1.29	5.69	2.60
<i>Cmcm</i>	1.14	0.69	2.23	1.61	2.85	2.21
1:1	0.74	0.79	1.70	1.42	3.93	2.14
2:2	1.43	0.74	2.49	1.38	4.65	2.13
3:3	2.11	0.82	3.56	1.46	5.19	2.32

Table 4.2: Figure of merit maxima at the given temperatures

	300K:500K		300K:750K		500K:750K	
	<i>n</i> -type	<i>p</i> -type	<i>n</i> -type	<i>p</i> -type	<i>n</i> -type	<i>p</i> -type
SnS	0.95	0.97	1.36	1.18	1.93	1.49
SnSe	1.76	0.98	2.69	1.44	3.80	1.87
<i>Cmcm</i>	1.63	1.13	1.98	1.47	2.51	1.89
1:1	1.13	1.08	1.91	1.37	2.67	1.73
2:2	1.81	1.05	2.17	1.35	3.05	1.72
3:3	2.56	1.12	2.82	1.45	3.90	1.83

Table 4.3: Figure of merit maxima at fixed chemical potentials across the temperature ranges.

Whereas Table 4.3 gives the maximum figure of merits with the chemical potential fixed across temperatures, Table 4.4 below shows the maximum figure of merits if the optimal chemical potential is chosen individually at each temperature.

	300K:500K		300K:750K		500K:750K	
	<i>n</i> -type	<i>p</i> -type	<i>n</i> -type	<i>p</i> -type	<i>n</i> -type	<i>p</i> -type
SnS	1.01	0.99	1.56	1.22	2.03	1.51
SnSe	1.94	0.99	3.19	1.53	4.18	1.94
<i>Cmcm</i>	1.68	1.15	2.07	1.50	2.54	1.91
1:1	1.22	1.10	2.12	1.45	2.81	1.78
2:2	1.96	1.06	2.86	1.42	3.57	1.76
3:3	2.83	1.14	3.62	1.53	4.38	1.89

Table 4.4: Maximal averaged figure of merits of the given temperature range, with optimal μ values for each individual temperature.

The figure of merits provided give a clear picture of the effectiveness of the interlayering on the thermoelectric properties of SnS and SnSe. At low temperatures, the layered structures are shown to improve upon the SnSe, with all structures outperforming in the *p*-doping region and 3:3-*Pmn2₁* outperforming in the *n*-doping region. The low temperature improvement is clear as well, whereas the *Pnma*-SnSe figure of merits remain above the

interlayered structures at 750 K. As the *Cmcm*-SnS shows the greatest improvement on *Pnma*-SnS at the lower temperatures, so do the interlayered structures show their largest improvements over *Pnma*-SnSe. This can be seen as another indication of the *Cmcm*-like nature of the interlayered structures and the benefits that this brings.

4.2 - Summary

4.2.1 - Lattice Thermal Conductivities

Effective Reduction of the Heat Transport

The lattice thermal conductivities of the sandwich-layer structures give a clear and pronounced benefit to the disruption of the heat transport in not only the layering direction, but also within the layers themselves. This reduction in lattice thermal conductivity is highly pronounced in the 2:2- Pm and 3:3- $Pmn2_1$ systems, and with the trend of larger layering thickness leading to lower lattice thermal conductivity further exploration of larger layer thickness is needed to determine the optimum.

Reduction of the Phonon Lifetimes and Mean Free Paths

The heatmap of phonon lifetimes by phonon mode frequencies (Fig. 4.8) give a clear explanation for the decrease in the lattice thermal conductivity. The disruption of low frequency phonon modes through the layering boundaries is shown to severely disrupt the transport of heat carriers throughout the material. This is reinforced through the significant reduction of long mean free path contributions to lattice thermal conductivity, as seen in the Fig. 4.9

Softened Phonon Modes and the Reduction of Group Velocities

The long-range phonon scattering is to be expected in a system with additional lattice boundaries, but the reduction of the lattice thermal conductivity is also shown to be further enhanced through intrinsic phonon structure changes, namely the softening of low-frequency phonon modes, which in turn greatly reduce the phonon group velocities. This two-factor influence on the heat transport through intrinsic and extrinsic effects make this material engineering approach a significant step in the further reduction of the lattice thermal conductivity of tin chalcogenide thermoelectrics.

4.2.2 - Electronic Suitability

The power factors in Fig. 4.9 make clear that the phonon scattering caused by the layered boundaries does not seriously impede the electronic properties of the 1:1- $Pmn2_1$ or 2:2- Pm species. The 3:3- $Pmn2_1$ structure does see a reduction in the maximal power factor due largely to a slower increase in electronic conductivity from the Fermi level. Overall, the electronically similar component layers are shown to allow for efficient charge transport

through the artificial barriers. The figure of merits also confirm this, with strong zT values shown for all structures in low and high temperature conditions, and the reduction in maximal power factor is show to not decrease the efficiency of the $3:3-Pmn2_1$ species significantly enough to outweigh the lattice benefits provided.

4.2.3 - Full Figure of Merit

Competitive Nature

The $2:2-Pm$ structure showed very low lattice thermal conductivity values, and respectable Seebeck and electronic conductivity values. This combination led to good maximal figure of merits at the three temperatures considered, in the same region as the SnSe figure of merits. The $3:3-Pmn2_1$ species far surpassed this, with a lower lattice thermal conductivity and, in spite of a lower power factor, a significant improvement in the full figure of merit, and a higher maximal figure of merit across the temperature range.

Low Temperature Efficiency

In thermoelectric usage, low temperature efficiency is highly important. Many thermoelectric materials show strong figure of merits, but low temperature efficiency is harder to achieve and more beneficial in application. Therefore, the improvement in the figure of merit at low temperatures shown by the $3:3-Pmn2_2$ structure is highly significant. The greater figure of merit improvement at low temperatures is shared by both the $2:2-Pm$ and the $3:3-Pmn2_1$ and can be compared to the larger low-temperature figure of merits of the $Cmcm$ -SnS structure, again indicating the influence of $Cmcm$ -like nature in the improved figure of merits.

Ultimately this low temperature improvement shows that not only can the layering improve the general efficiency of the material, but it does so specifically in the temperature region most desired for new thermoelectric breakthroughs and most applicable to their current use.

References

- [1] Asfandiyar, T.-R. Wei, Z. Li, F.-H. Sun, Y. Pan, C.-F. Wu, M. U. Farooq, H. Tang, F. Li, B. Li and J.-F. Li, "Thermoelectric SnS and SnS-SnSe Solid Solutions Prepared by Mechanical Alloying and Spark Plasma Sintering: Anisotropic Thermoelectric Properties," *Scientific Reports*, vol. 7, p. 43262, 2017.
- [2] Y.-M. Han, J. Zhao, M. Zhou, X.-X. Jiang, H.-Q. Leng and L.-F. Li, "Thermoelectric Performance of SnS and SnS–SnSe Solid Solution," *Journal of Materials Chemistry A*, vol. 3, no. 8, pp. 4555-4559, 2015.
- [3] C. Wan, Y. Wang, N. Wang, W. Norimatsu, M. Kusunoki and K. Koumoto, "Intercalation: Building a Natural Superlattice for Better Thermoelectric Performance in Layered Chalcogenides," *Journal of Electronic Materials*, vol. 40, no. 5, pp. 1271-1280, 2011.
- [4] D. Selli, D. Donadio and S. Leoni, "PbTe/PbSe Thermoelectric Nanocomposites: The Impact of Length Modulations on Lowering Thermal Conductivity," *Zeitschrift für Anorganische und Allgemeine Chemie*, p.e202200048, 2022.
- [5] T. Lorenz, J.-O. Joswig and G. Seifert, "Combined SnS@SnS₂ Double Layers: Charge Transfer and Electronic Structure," *Semiconductor Science and Technology*, vol. 29, p. 064006, 2014.
- [6] J. Gu, L. Huang and S. Liu, "Ultralow Lattice Thermal Conductivity and High Thermoelectric Performance of Monolayer KCuTe: A First Principle Study," *RSC Advances*, vol. 9, no. 62, pp. 36301-36307, 2019.
- [7] M. Sajjad, Q. Mahmood, N. Singh and J. A. Larsson, "Ultralow Lattice Thermal Conductivity in Double Perovskite Cs₂PtI₆: A Promising Thermoelectric Material," *ASC Applied Energy Materials*, vol. 3, no. 11, pp. 11293-11299, 2020.
- [8] M. Sajjad, N. Singh, S. Sattar, S. De Wolf and U. Schwingenschlögl, "Ultralow Lattice Thermal Conductivity and Thermoelectric Properties of Monolayer TI₂O," *ASC Applied Energy Materials*, vol. 2, no. 5, pp. 3004-3008, 2019.
- [9] B. Koley, A. Lakshan, P. R. Raghuvanshi, C. Singh, A. Bhattacharya and P. P. Jana, "Ultralow Lattice Thermal Conductivity at Room Temperature in Cu₄TiSe₄," *Agewandte Chemie International Edition*, vol. 60, no. 16, pp. 9106-9113, 2020.

Chapter 5:

Asymmetric Layering

The use of uniform stacking of *Pnma*-SnS and SnSe showed a strong improvement in the thermoelectric figure of merit through the reduction of heat transport by phonon scattering and softening. However, in reaching such a large reduction in lattice thermal conductivity the electronic suitabilities of the materials were diminished, with the strong power factors of the base materials weakened through the addition of boundaries into the lattice structure. The next step was therefore to attempt to find a compromise between these two positions to best utilise the scattering and softening modes without disruption of the electronic transport properties.

With the assumption that electronic transport across SnS-SnSe boundaries is the cause of the drop in power factor, a new exploration of materials with unequal component layers was undertaken. The structures chosen were SnS/2SnSe, 2SnS/SnSe, SnS/3SnSe and 3SnS/SnSe. Due to the stacking nature of the *Pnma* layers, the 1:2 and 2:1 species required three *Pnma* unit cell lengths in the *a* axis, whereas the 3:1 and 1:3 species only required 2 *Pnma* unit cell lengths. The need for this is seen in Fig. 5.1a, where in the zigzag motif along the *c* axis flips leading direction, such that in the 2:1 and 1:2 species the inserted layers would be incorrect if only 3 layers (1.5 *Pnma* unit cells) were used.

5.1 – SnS/2SnSe, 2SnS/SnSe, SnS/3SnSe and 3SnS/SnSe

5.1.1 - Electronic Properties

Characterisation

The SnS/2SnSe (1:2), 2SnS/SnSe (2:1), SnS/3SnSe (1:3) and 3SnS/SnSe (3:1) retained GeS-type (B16) derived structures, (SG *Pm*). Their crystal structures were relaxed with Quantum Espresso using a GGA-PBE exchange-correlation functional, the relaxed lattice parameters were: $a = 34.9325 \text{ \AA}$, $b = 4.1415 \text{ \AA}$, $c = 4.5501 \text{ \AA}$, (1:2-*Pm*); $a = 34.5690 \text{ \AA}$, $b = 4.0804 \text{ \AA}$, $c = 4.5146 \text{ \AA}$, (2:1-*Pm*); $a = 23.3417 \text{ \AA}$, $b = 4.1568 \text{ \AA}$, $c = 4.5526 \text{ \AA}$, (1:3-*Pm*); $a = 22.9832 \text{ \AA}$, $b = 4.0655 \text{ \AA}$, $c = 4.4984 \text{ \AA}$, (3:1-*Pm*). These values are collected in Table 5.1, with the values obtained in the previous calculations also given for reference.

If the averaged interlayer cell length of SnS and SnSe is given as $a_0 = 11.6089 \text{ \AA}$, the ratios of a/a_0 are 3.0091 for 1:2-*Pm*, 2.9778 for 2:1-*Pm*, 2.0107 for 3:1-*Pm*, and 1.9798 for 1:3-*Pm*, showing good retention of the relative cross-layer (*a*) axis length. The axial ratios can

also be compared to the base materials: for 1:2-*Pm* $b/(a/3) = 0.36$ and $c/(a/3) = 0.39$; for 2:1-*Pm* $b/(a/3) = 0.35$ and $c/(a/3) = 0.39$; for 1:3-*Pm* $b/(a/2) = 0.36$ and $c/(a/2) = 0.39$, and for 3:1-*Pm* $b/(a/2) = 0.35$ and $c/(a/2) = 0.39$. These are comparable to $b/a = 0.35$ and $c/a = 0.39$ for SnS, and $b/a = 0.36$ and $c/a = 0.39$ for SnSe.

	a / Å	b / Å	c / Å	SG
SnS(<i>Pnma</i>)	11.4455	4.0240	4.4481	<i>Pnma</i>
SnSe	11.7834	4.2054	4.5638	<i>Pnma</i>
SnS(<i>Cmcm</i>)	11.8044*	4.1187*	4.1166*	<i>Cmcm</i>
1:1	11.6023	4.1105	4.5357	<i>Pmn2₁</i>
2:2	23.1432 (11.5716**)	4.1104	4.5344	<i>Pm</i>
3:3	34.6994 (11.5665**)	4.1111	4.5378	<i>Pmn2₁</i>
1:2	34.9325 (11.6442**)	4.1415	4.5501	<i>Pm</i>
2:1	34.5690 (11.5230**)	4.0804	4.5146	<i>Pm</i>
1:3	23.3417 (11.6709**)	4.1568	4.5526	<i>Pm</i>
3:1	22.9832 (11.4916**)	4.0655	4.4984	<i>Pm</i>

Table 5.1: Cell lengths and resultant space groups of the asymmetrically interlayered structures, with the previous calculated structures shown for comparison

**Cmcm* axes represented as orthorhombic and aligned to the *Pnma* axis directions

**2:2 and 3:3 relative a axis lengths

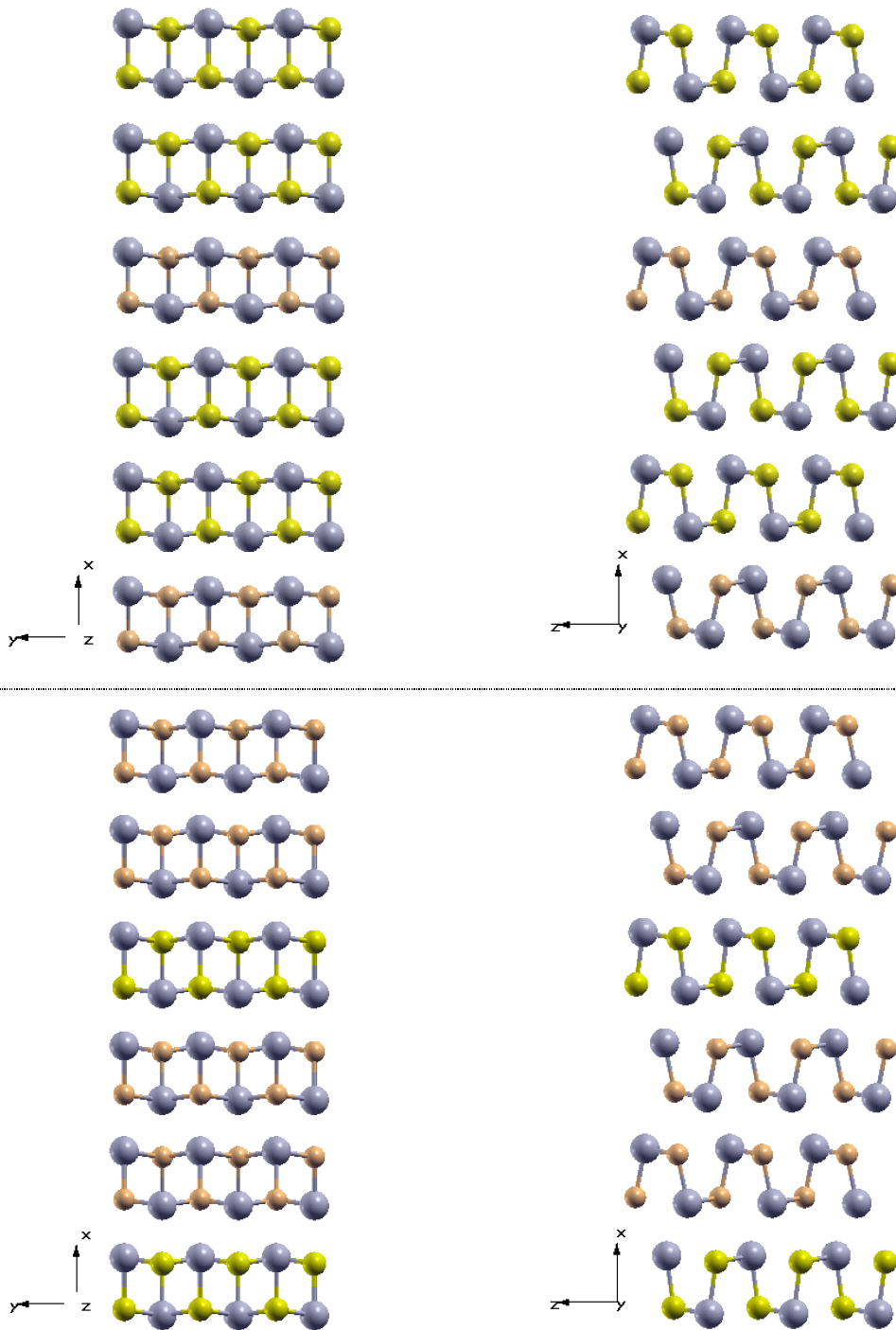


Fig 5.1a: The layered structures viewed down the c (left) and b (right) axes.
 Above: SnS/2SnSe (1:2-*Pm*) Below: 2SnS/SnSe (2:1-*Pm*)

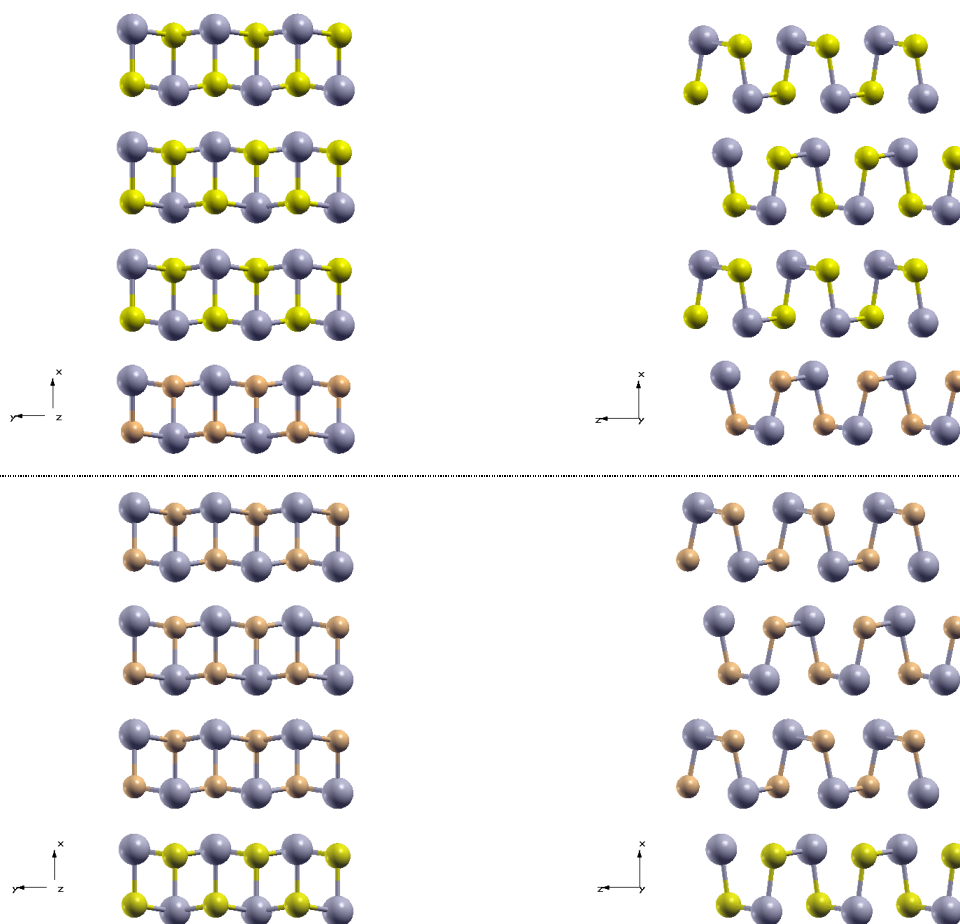


Figure 5.1b: The layered structures viewed down the c (left) and b (right) axes.
 Above: SnS/3SnSe (3:1-*Pm*) Below: 3SnS/SnSe (3:1-*Pm*)

The electronic band structures of the layered structures (Fig. 5.2) all show strong similarities to the SnS and SnSe band structures along the highest valence and lowest conduction bands. Whilst the band structures retain the two valence band maxima and two conduction band minima in the Y- Γ -Z pathway, the maximum along the Γ -Z is increased higher than the Γ -Y. The separation of bands at the S and R points that was present in the uniformly layered structures is also present in these asymmetric layer band structures. Also of note is the lowering of the conduction band minima along the X-S pathway to such a level that it is almost in line with the overall conduction band minima.

The direct band gaps are 1.064 eV for 1:2-*Pm*, 1.083 eV for 2:1-*Pm*, 1.033 eV for 1:3-*Pm*, and 1.083 eV for 3:1-*Pm*. The indirect band gaps are 0.590 eV for 1:2-*Pm*, 0.685 eV for 2:1-*Pm*, 0.562 eV for 1:3-*Pm*, and 0.677 eV for 3:1-*Pm*.

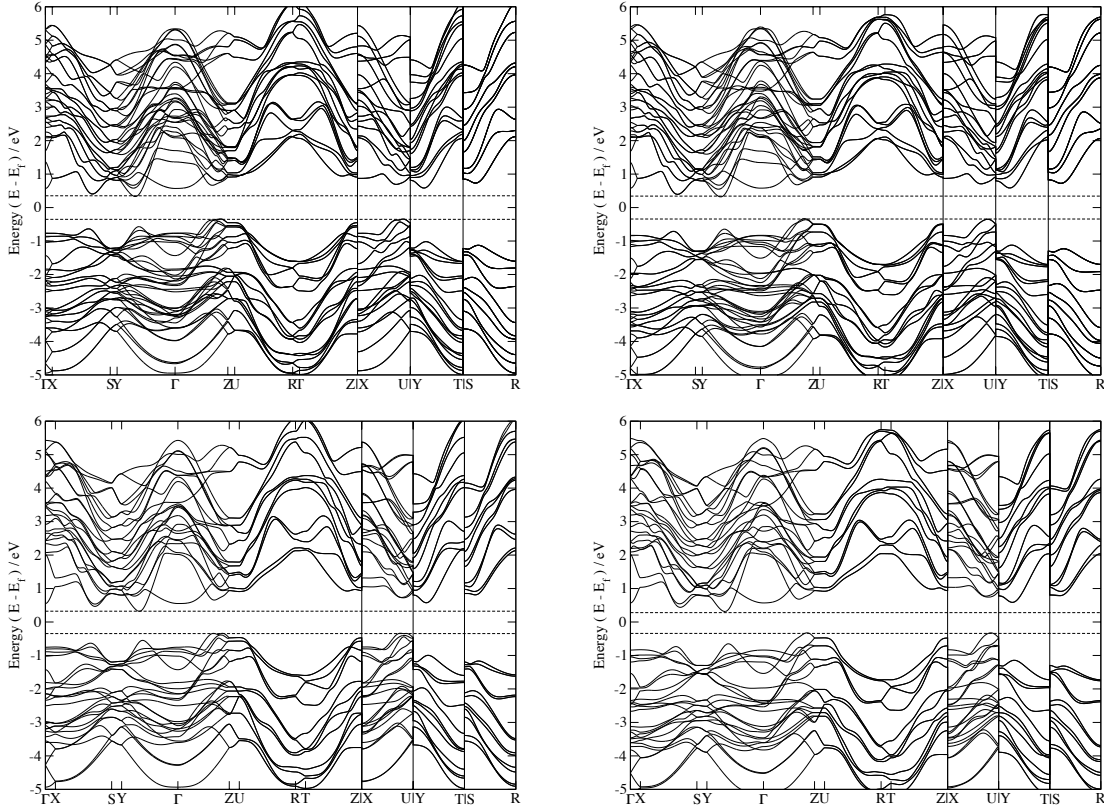


Figure 5.2: 1:2-*Pm* (upper left), 2:1-*Pm* (upper right), 1:3-*Pm* (lower left), and 3:1-*Pm* (lower right) electronic band structures calculated with Wannier90

BoltzWann

The Seebeck coefficient and electronic conductivity curves show strong similarity to the curves of the uniformly layered structures, with a similar strong anisotropy in the layered and intralayer directions. The electronic conductivity curve also saw the decrease in *n*-type conductivity for the *a* axis, and slightly strengthened *p*-type Seebeck coefficient. The maxima of the Seebeck curves across the *x*, *y* and *z* directions were: 1087, 1157 and 1136 $\mu\text{V/K}$ in the *p*-doping region and -1159, -1043 and -1063 $\mu\text{V/K}$ in the *n*-doping region of 1:2-*Pm*; 941, 1118 and 1094 $\mu\text{V/K}$ in the *p*-doping region and -1141, -1040 and -1053 $\mu\text{V/K}$ in the *n*-doping region for 2:1-*Pm*; 1021, 1131 and 1111 $\mu\text{V/K}$ in the *p*-doping region and -1141, -1040 and -1053 $\mu\text{V/K}$ in the *n*-doping region for 1:3-*Pm*; and 751, 757 and 744 $\mu\text{V/K}$ in the *p*-doping region and -1235, -1010 and -1024 $\mu\text{V/K}$ in the *n*-doping region for 3:1-*Pm*. All structures showed similar Seebeck coefficients to the uniformly layered structures and to *Pmna*-SnSe.

The minima of the electrical conductivity curves across the x, y and z directions were: 208, 1983 and 1471 $\mu\text{S}/\text{cm}$ in 1:2-*Pm*; 286, 2283 and 1832 $\mu\text{S}/\text{cm}$ in 2:1-*Pm*; 208, 1983 and 1471 $\mu\text{S}/\text{cm}$ in 1:3-*Pm*; and 99, 3480 and 2721 $\mu\text{S}/\text{cm}$ in 3:1-*Pm*. Whilst these values are generally similar to the uniformly layered structures, the electrical conductivity values show a steeper slope moving away from the Fermi level in the layered direction than seen in the 2:2-*Pm* and 3:3-*Pmn*₂₁ structures.

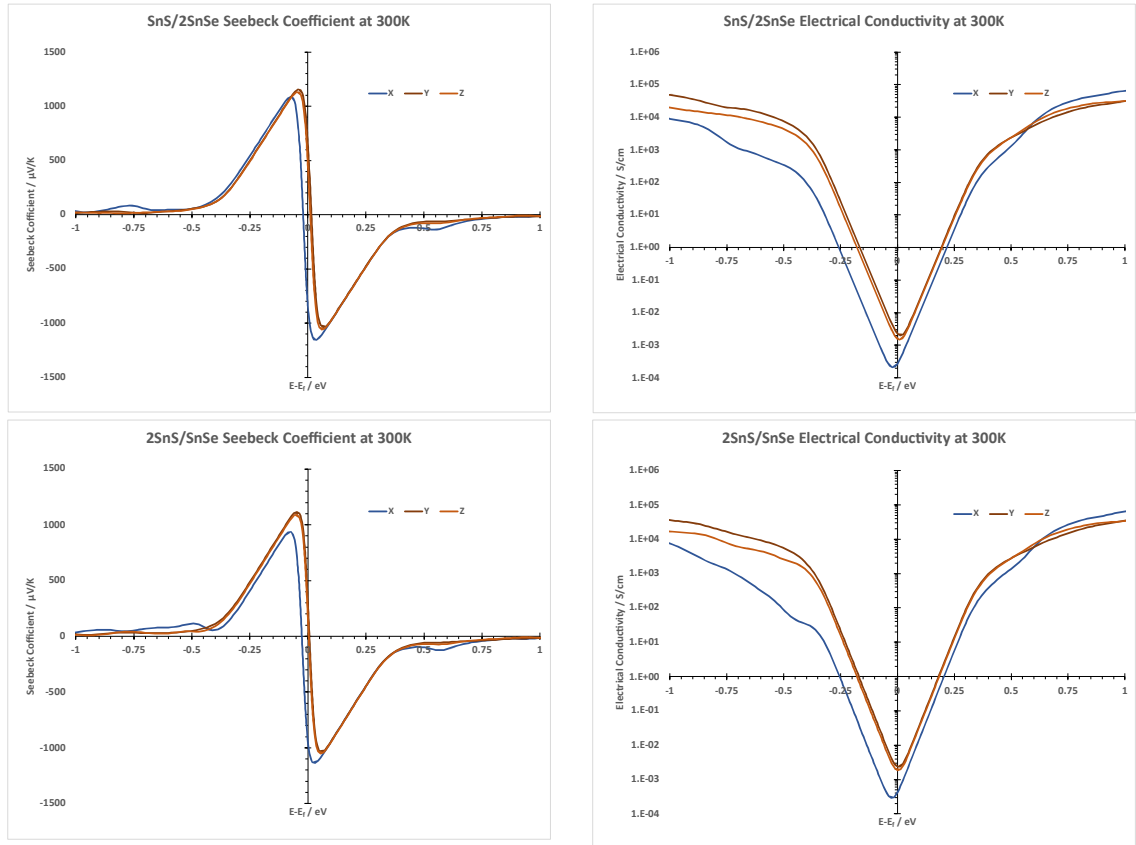


Figure 5.3a: 1:2-*Pm* (above), 2:1-*Pm* (below), Seebeck Coefficient and Electrical Conductivities across μ values ± 1 eV from the Fermi level at 300 K.

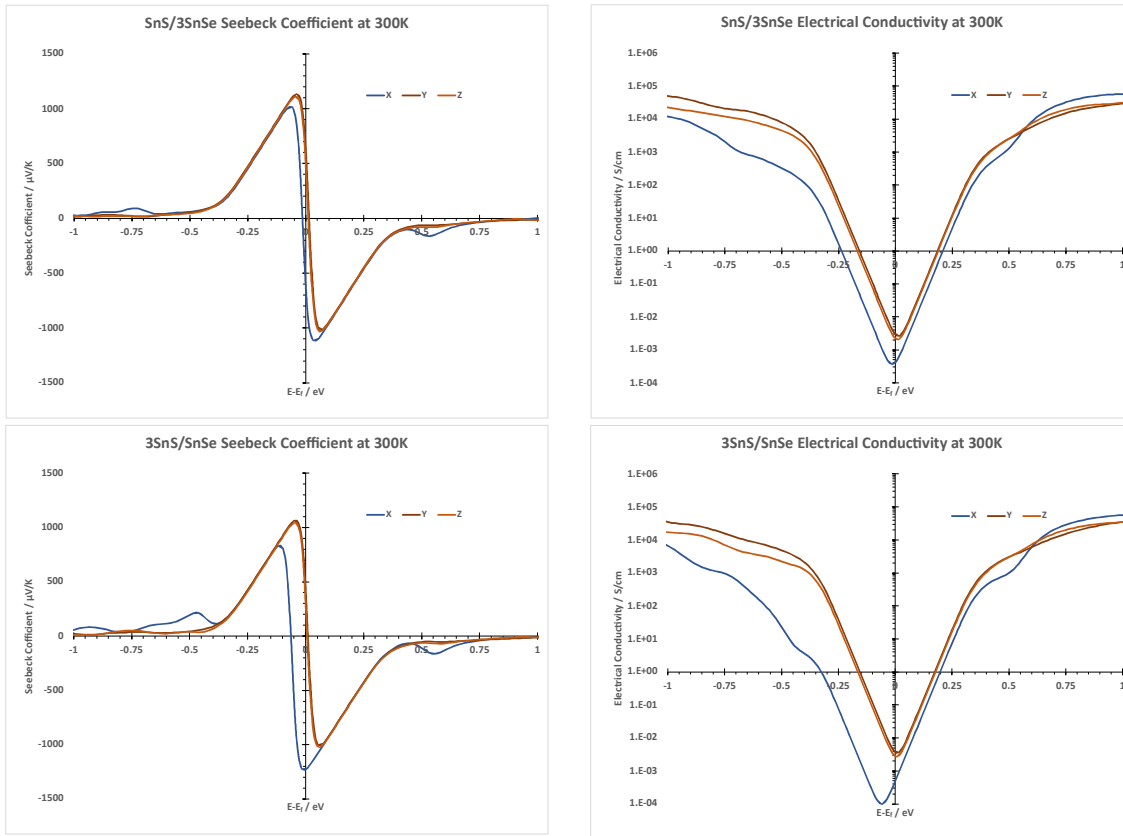


Figure 5.3b: 1:3-*Pm* (above), and 3:1-*Pm* (below) Seebeck Coefficient and Electrical Conductivities across μ values ± 1 eV from the Fermi level at 300 K.

Power Factor

The power factors for the asymmetric layering structures were overall satisfactory when compared to the *Pnma* structures. The electronic performance of all variants were maintained well in the *n*-doping region, with the all structures reaching peak values of over 8 mW/m/K^2 . The 1:3-*Pm* and 3:1-*Pm* structures showed very strong peak power factors of over 10 mW/m/K^2 in the *n*-doping region, reaching similar levels to *Pnma*-SnSe and the 2:2-*Pm* peaks. The 1:2-*Pm* and 1:3-*Pm* also saw slight increases in the *p*-doping region near-Fermi maxima to values above that of *Pnma*-SnSe, indicating a shift in the *p*-type electronic suitability not seen in the uniformly layered stacking structures.

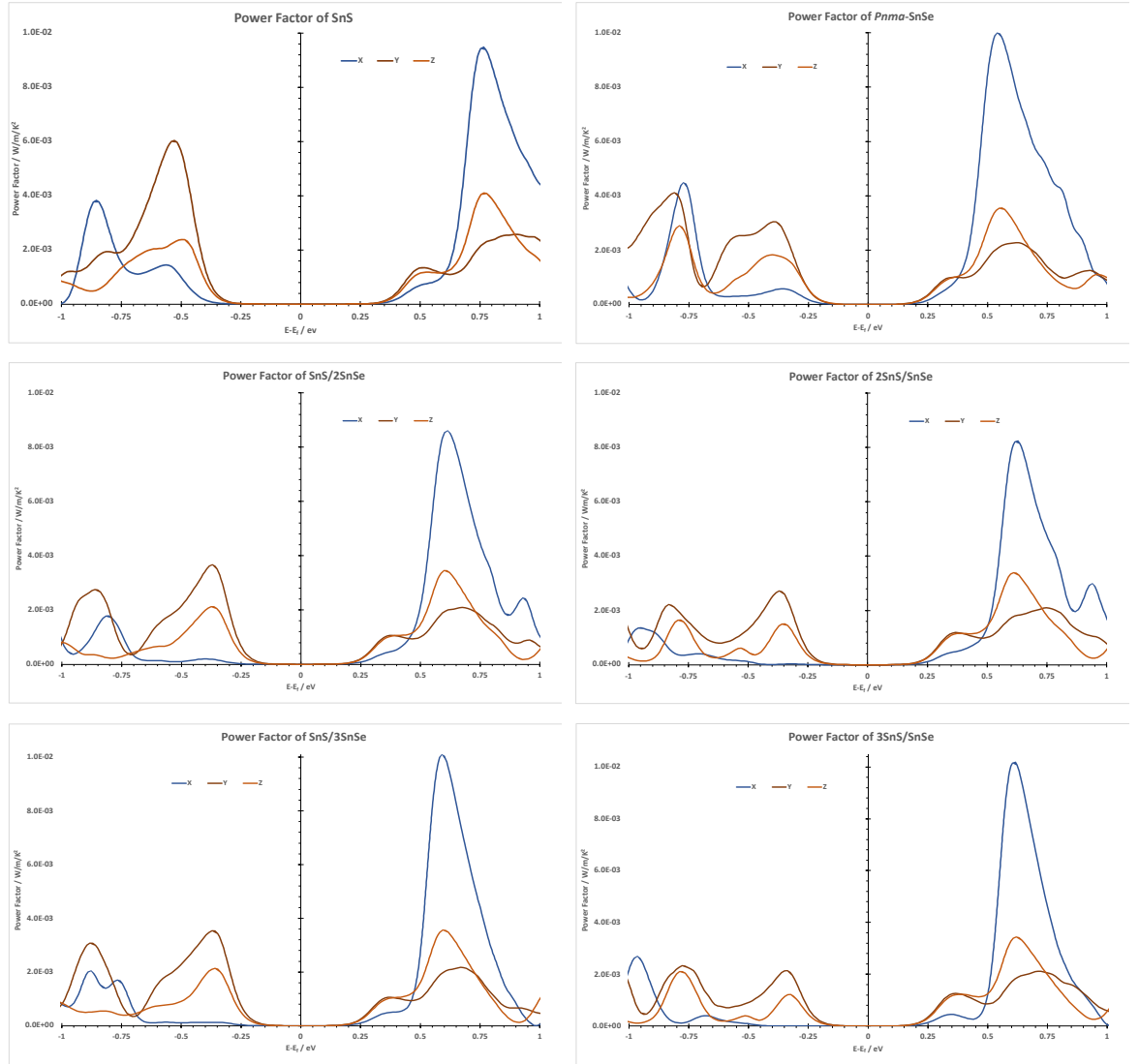


Figure 5.4: The Power Factors of *Pnma*-SnS (upper left), *Pnma*-SnSe (upper right), 1:2-*Pm* (middle left), 2:1-*Pm* (middle right), 1:3-*Pm* (lower left) and 3:1-*Pm* (lower right) across the chemical potential range $E_f \pm 1$ eV

5.1.2 - Phononic Properties

Characterisation

Using the xTB methodology within CP2K, the relaxed structures were obtained, with lattice parameters of $a = 31.8558 \text{ \AA}$, $b = 3.8759 \text{ \AA}$, $c = 3.8730$ for 1:2-*Pm*; $a = 31.5234 \text{ \AA}$, $b = 3.8742 \text{ \AA}$, $c = 3.7630$ for 2:1-*Pm*; $a = 21.2893 \text{ \AA}$, $b = 3.8845 \text{ \AA}$, $c = 3.8911$ for 1:3-*Pm*; $a = 21.8982 \text{ \AA}$, $b = 3.8926 \text{ \AA}$, $c = 3.7200$ for 3:1-*Pm*. It is again noted the change in shortest cell length, where for the 1:2-*Pm*, 2:1-*Pm* and 3:1-*Pm* structures the c axes are shorter than the b , the reverse of the *Pnma* b/c cell length order, but in line with the *Cmcm* ordering $a > b > c$.

Phonon Dispersion

The phonon dispersion spectra show most of the features established in the previous chapters, with the notable reintroduction of a band gap in 3:1-*Pm* species at approximately 3.5 THz. The lowest band frequencies at the special points X, Y and Z are: 0.1719, 0.9167 and 0.8120 THz for 1:2-*Pm*; 0.2040, 1.0414 and 0.9067 THz for 2:1-*Pm*; 0.2391, 0.8567 and 0.7804 THz for 1:3-*Pm*; and 0.2812, 0.9818 and 0.7788 THz for 3:1-*Pm*. This indicates that the band softening along the a-axis still occurs in these asymmetric layering structures, with the greatest effect seen in the 1:2-*Pm* structure, and a large anisotropy in band softening in the 2:1-*Pm* structure, where the b and c axes show much higher frequencies than the a, with the frequencies in the b and c axes above those of all other asymmetric structures.

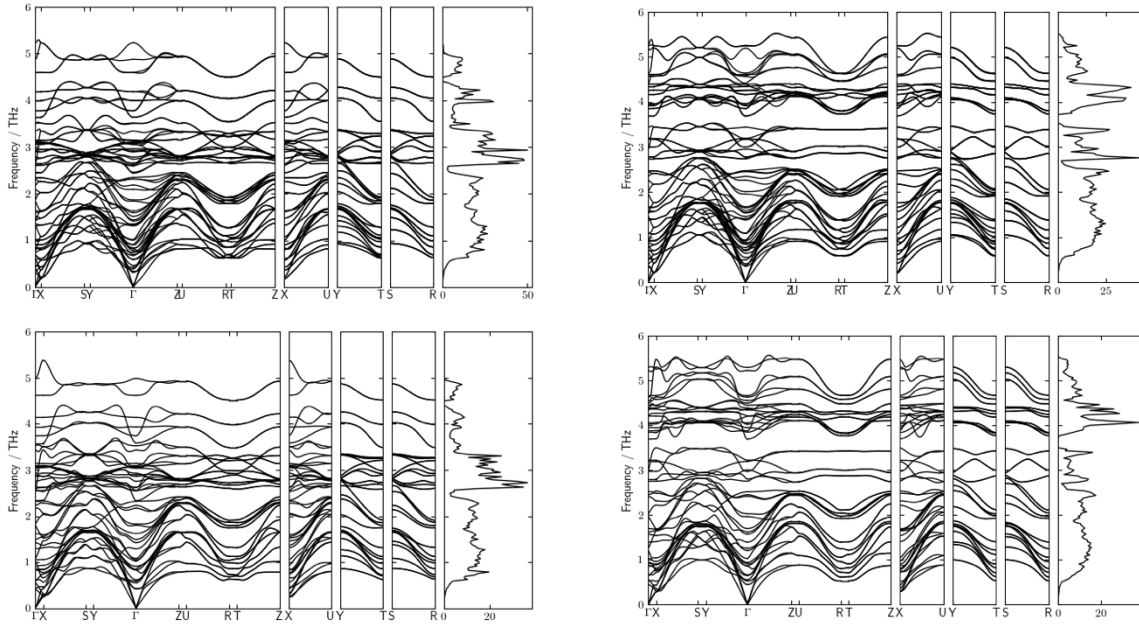


Figure 5.5: Phonon dispersion spectra given in THz, calculated through Phonopy using CP2K/xTB for force calculation, for 1:2-*Pm* (upper left), 2:1-*Pm* (upper right), 1:3-*Pm* (lower left), and 3:1-*Pm* (lower right)

Lattice Thermal Conductivity

The lattice thermal conductivity values of the 1:2-*Pm* layered material at 300K are 0.2433, 0.6257 and 0.5336 W/m/K for the a b and c axes respectively, with an averaged isotropic lattice thermal conductivity of 0.4676 W/m/K. For 2:1-*Pm* the values are 0.3324, 0.9017

and 0.7176 W/m/K, and 0.6506 Wm/K, for 1:3-*Pm*, 0.2010, 0.6079 and 0.5252 W/m/K, and 0.4447 W/m/K, and for 3:1-*Pm*, 0.2348, 0.8872 and 0.7149 W/m/K, and 0.6123 W/m/K.

These values show improvements over the *Pnma*-SnSe lattice thermal conductivities (0.3374, 0.7726 and 0.5652 W/m/K), but at lesser degrees to the 2:2-*Pm* and 3:3-*Pmn*₂ species. This can be seen as another affect of the lattice thermal conductivities dependence on layer thickness, as all species have either single SnS or SnSe layers, which seem to be less effective in disrupting the lattice phonon transport. The anisotropy of the 3:1-*Pm* species is also notable, with the intralayer axes exhibiting far larger lattice thermal conductivities compared to the cross-layer than in the other structures. The ratios of the cross-layer and averaged intralayer lattice thermal conductivities for the asymmetric layering species are 0.42 (1:2-*Pm*), 0.41 (2:1-*Pm*), 0.35 (1:3-*Pm*) and 0.29 (3:1-*Pm*).

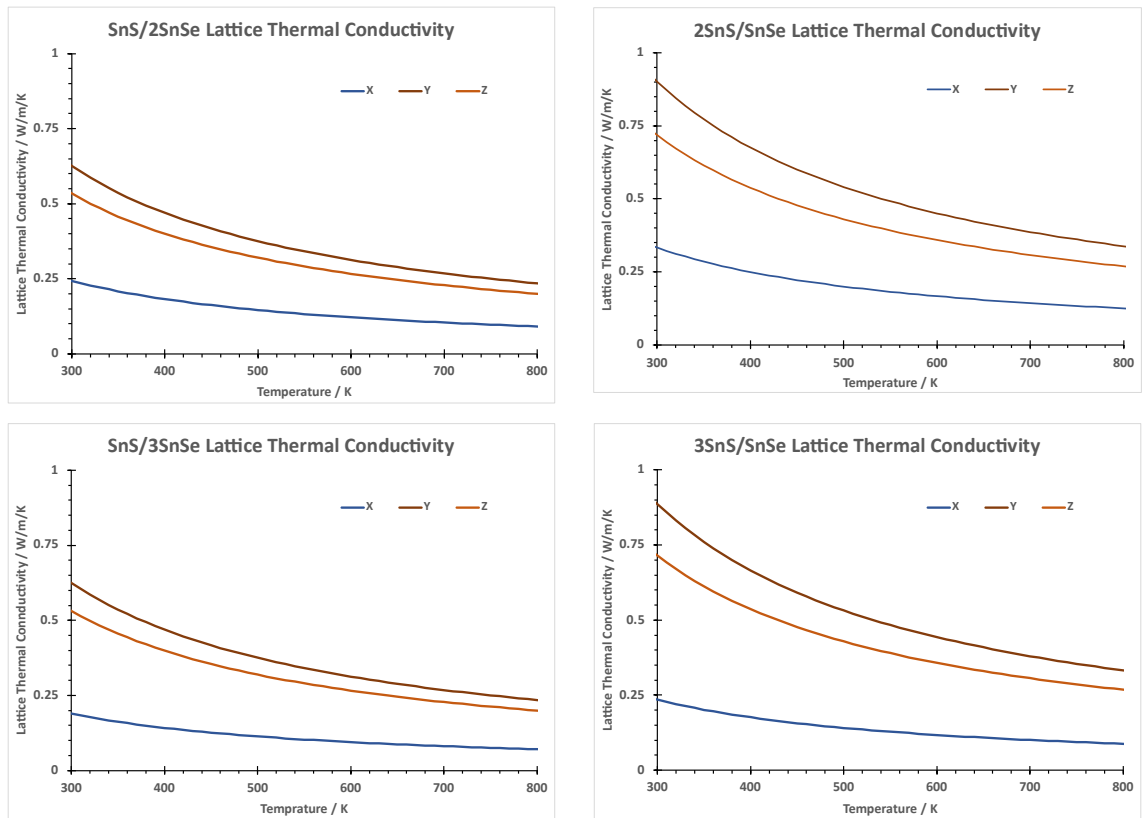


Figure 5.6: Lattice thermal conductivity, κ_{latt} , along the a, b and c axes as a function of temperature for 1:2-*Pm* (upper left), 2:1-*Pm* (upper right) and 1:3-*Pm* (lower left) and 3:1-*Pm* (lower right)

The lattice thermal conductivities are shown in Fig. 5.7, separated into the cross-layer direction and the averaged intralayer direction and with comparison to the previously obtained lattice thermal conductivities.

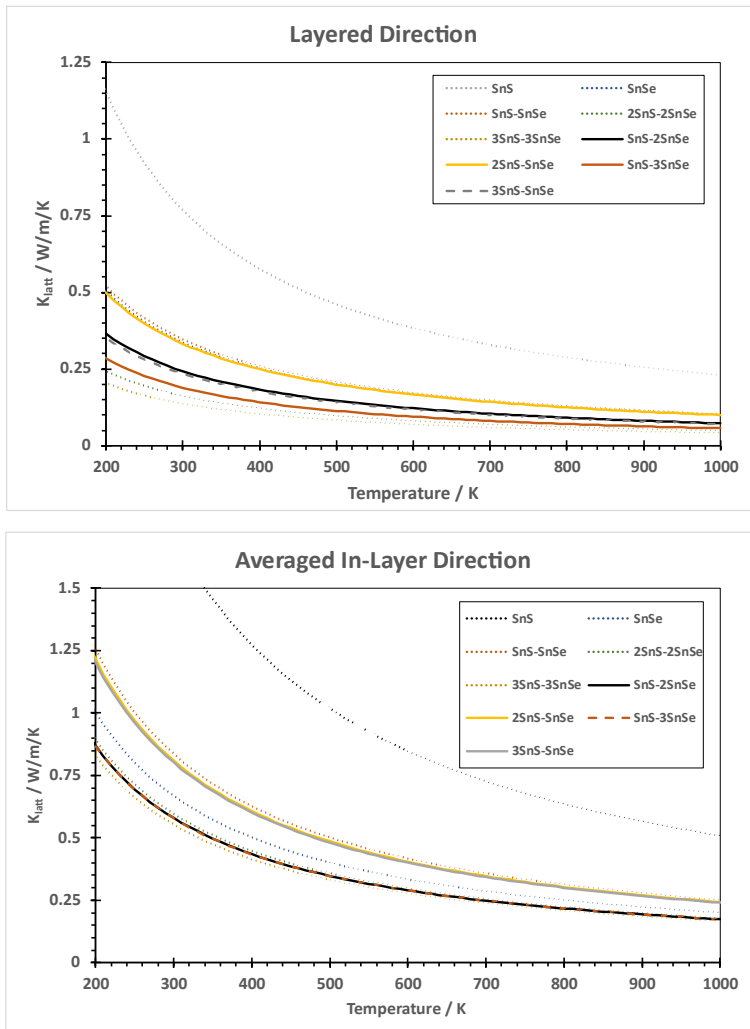
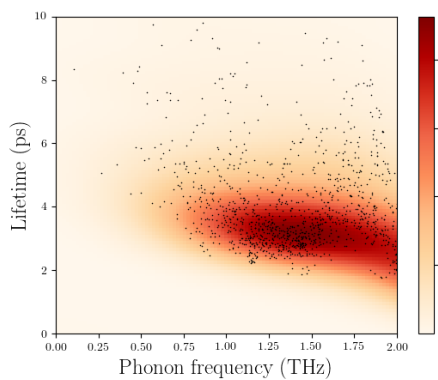


Figure 5.7: The lattice thermal conductivities of the layered direction, a (above), and the averaged intralayer direction, b and c (below), with previous calculations shown as dotted lines, and 1:3-*Pm* layered and 3:1-*Pm* in-layer shown as a dashed line so as not to obscure 1:2-*Pm*

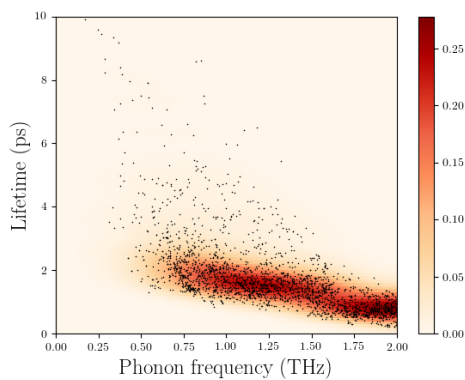
Phonon Lifetimes

The plots of the phonon lifetimes by mode frequency show similar characteristics to the uniform layered species, excepting that due to the imbalance in S/Se ratio the 1:2 and 1:3 structures showed fewer phonon modes in the 4-5 THz region and denser hotspots in the 2.5-3.5 THz region. The lower frequency of these 2.5-3.5 THz phonon modes indicates a

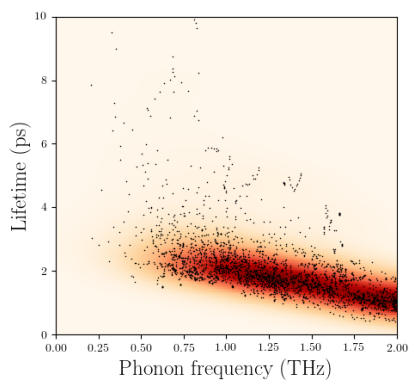
decreased lifetimes in the low-frequency region compared to *Pnma*-SnS, with the 1:2-*Pm* and 1:3-*Pm* heatmaps showing slightly lower lifetimes than the 2:1-*Pm* or 3:1-*Pm*.



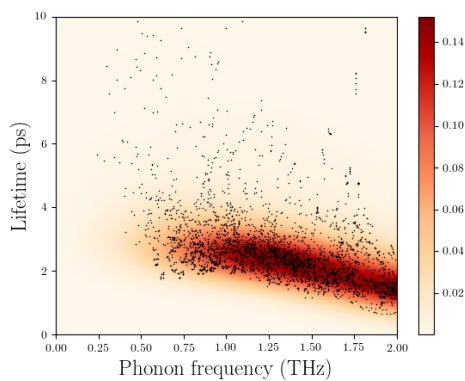
(a) *Pnma*-SnS



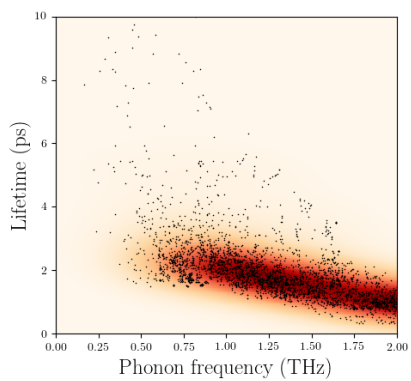
(b) *Pnma*-SnSe



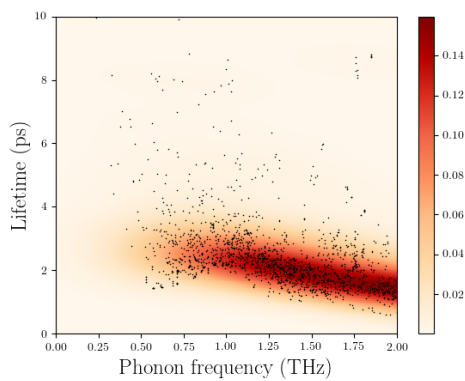
(c) 1:2-*Pm*



(d) 2:1-*Pm*



(e) 1:3-*Pm*



(f) 3:1-*Pm*

Figure 5.9: Phonon lifetimes of *Pnma*-SnS (a), *Pnma*-SnSe (b) 1:2-*Pm* (c), 2:1-*Pm* (d), 1:3-*Pm* (e), and 3:1-*Pm* (f)

Phonon Mean Free Paths¹

The asymmetric layered structures continued to show the reduction in long mean free path phonon contribution to lattice thermal conductivity present in the uniformly layered structures, with 1:2-*Pm* and 1:3-*Pm* presenting a axis mean free path contributions below *Pnma*-SnSe across the range.

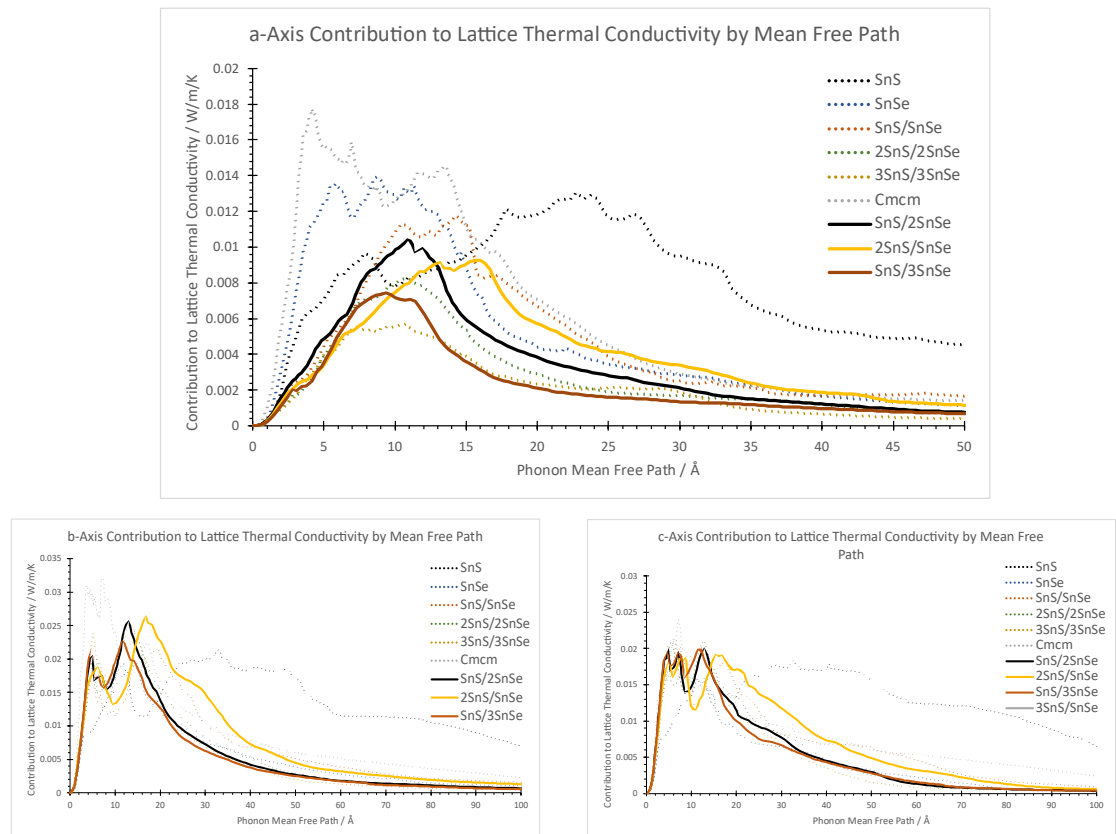


Figure 5.10: The phonon contribution to the lattice thermal conductivity at 300 K by their mean free path, resolved to the *Pnma*-a (above), *Pnma*-b (lower left) and *Pnma*-c (lower right) axes

¹ It should be noted that due to systematic errors in the auxiliary code *phono3py-kaccum*'s understanding of the symmetry of the systems, the 3:1-*Pm* structure was unable to be evaluated in terms of its mean free path contribution to lattice thermal conductivity at the time of writing and is therefore excluded from the plots below

The 2:1-*Pm* structure shows the similar mean free path contributions shared by all the interlayered structures from 0 to 10 Å, but exhibits higher contributions from long mean free path length phonon modes, in line with the 1:1-*Pmn2₁* structure and above that of *Pnma*-SnSe. This is also the case in the *b* and *c* axes, with higher contributions in the long-range phonon modes than any of the other interlayered structures. This is to be expected as the 2:1-*Pm* structure had the highest calculated lattice thermal conductivities of the four asymmetric layering species. The 1:2-*Pm* and 1:3-*Pm* structures continue the trend of low long mean free path contributions, however, and the 1:3-*Pm* in particular exhibits very low values in line with its low lattice thermal conductivity.

*Group Velocities*²

The group velocities of the asymmetric layering structures also continue the trend seen in previous calculations, with the curves in Fig. 5.11 fitting well with the 2:2-*Pm* and 3:3-*Pmn2₁* group velocity curves, and in agreement with their low cross-layer phonon frequency modes. This can be seen most clearly in the 0-1.5 THz region of the *a* axis, and the 0-2 THz regions of the *b* and *c* axes. At frequencies above these ranges there is no clear separation between the group velocities of the interlayered structures when compared to the *Pnma* and *Cmcm* group velocities.

² As with the lattice thermal contribution by mean free path data, the 3:1-*Pm* structure was unable to be evaluated in terms of its group velocity by frequency at the time of writing and is therefore excluded from the plots below.

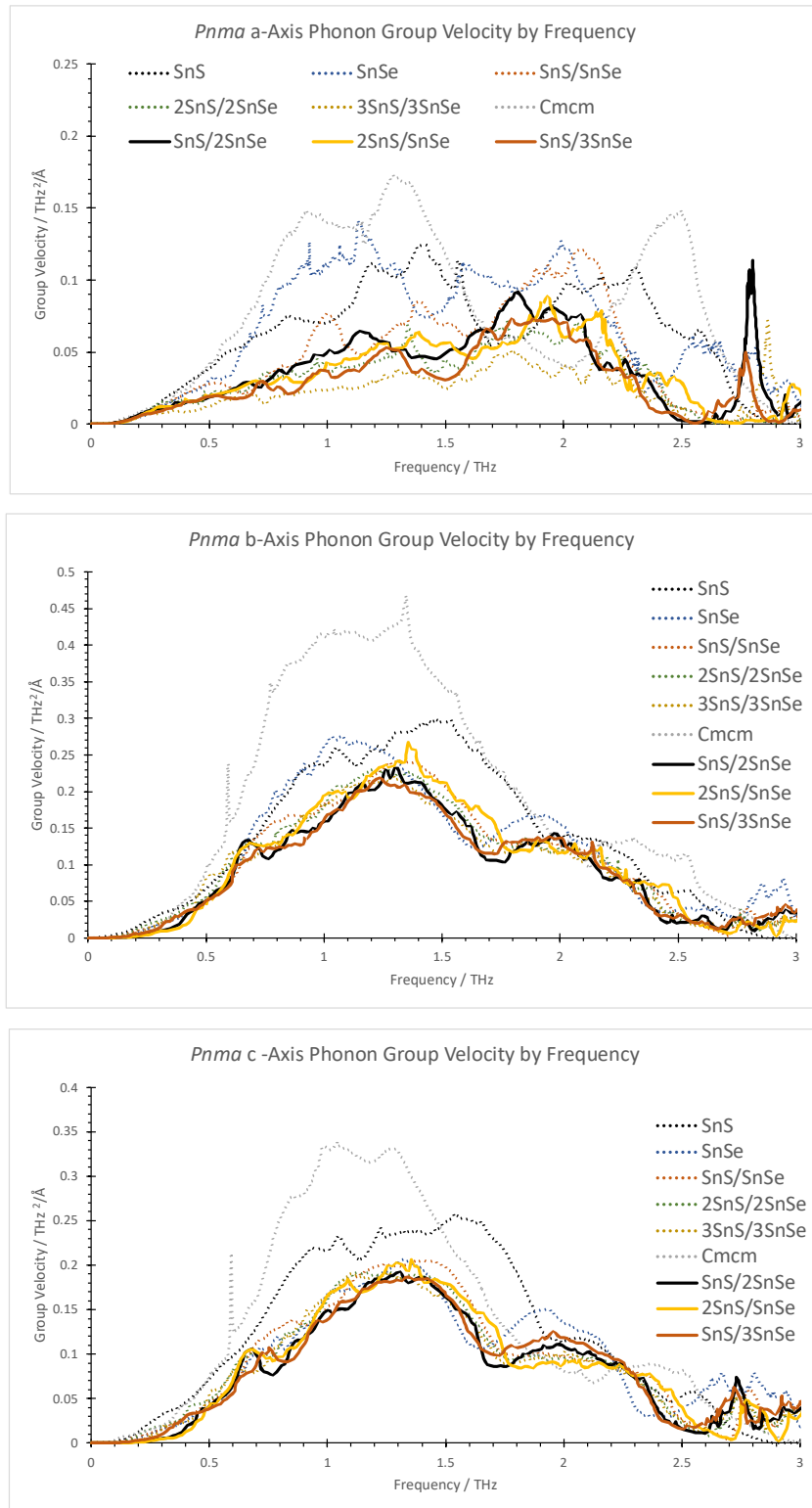


Figure 5.11: Group velocities of acoustic phonons along the layered direction (top), *Pnma*-*b*/*Cmcm*-*c* axis (middle), and *Pnma*-*c*/*Cmcm*-*a* axis (bottom)

5.1.3 - Full Figure of Merit

The full figure of merit was the obtained as with the *Pnma* and *Cmcm* structures.

At 300 K

As with the uniform structures, the relaxation times could not be aligned with experimental data, and thus had to be estimated from the *Pnma* relaxation times. Whilst the uniform layering structures used a simple average, the uneven SnS/SnSe ratio necessitated a weighted average for these structures to account for the differing amount of the constituent *Pmna* base layers in the unit cell such that $\tau_{n:m} = (n\tau_{SnS} + m\tau_{SnSe})/(n + m)$. For example, the 1:3-*Pm* structure is composed of 1 layer of SnS and 3 layers of SnSe, and as so the relaxation time at 300 K was defined as $\tau_{1:3} = (\tau_{SnS} + 3\tau_{SnSe})/4$. This follows the assumption in Chapter 4 that the relaxation time is directly proportional to the relaxation times of the constituent layers. As such the relaxation times at 300 K were taken to be $\tau = 21.7253$ (1:2-*Pm*), $\tau = 23.3323$ (2:1-*Pm*), $\tau = 21.3235$ (1:3-*Pm*) and $\tau = 23.7341$ (3:1-*Pm*).

The full figure of merits of the asymmetric layer structures are shown in Fig. 5.12. Whilst the figure of merits did not reach the peak values seen in 3:3-*Pmn2₁*, the 1:3-*Pm* and 3:1-*Pm* both showed comparable figure of merits to *Pnma*-SnSe, and the 1:2-*Pm* and 1:3-*Pm* structures showed significant improvement in the *p*-type figure of merits relative to the previous structures. This *p*-type improvement comes through a lowering of the b-axis lattice thermal conductivity whilst reaching strong power factors, with peak levels above the *Pnma*-SnSe.

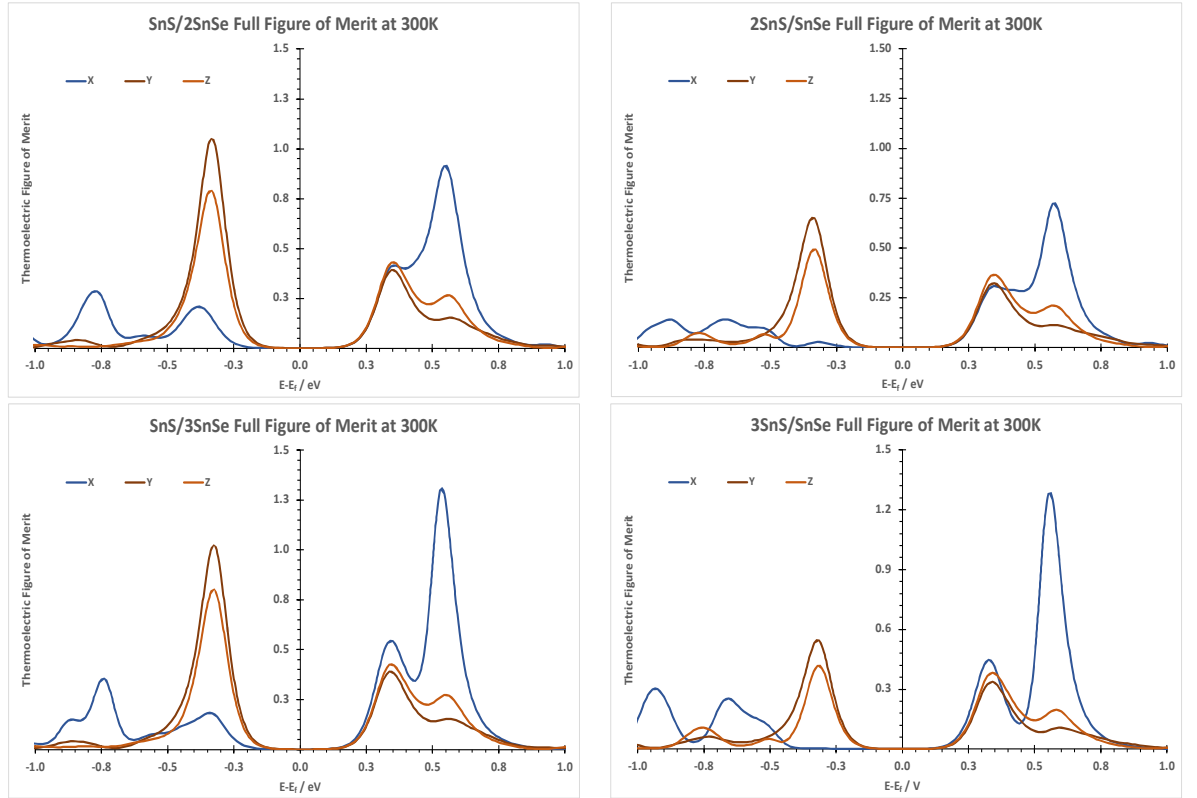


Figure 5.12: Figure of merits of 1:2-*Pm* (upper left), 2:1-*Pm* (upper right), 1:3-*Pm* (lower left), and 3:1-*Pm* (lower right), across the chemical potential range $E_f \pm 1$ eV, for each axis

At 300, 500 and 750 K

The 300, 500 and 750 K relaxation times for these materials are set to the following values determined by the weighted averages of the *Pnma*-SnS and *Pnma*-SnSe relaxation times: for 1:2-*Pm*, $\tau_{300K} = 21.7253$ fs, $\tau_{500K} = 9.1935$ fs, $\tau_{750K} = 5.4541$ fs; for 2:1-*Pm*, $\tau_{300K} = 23.3323$ fs, $\tau_{500K} = 10.7545$ fs, $\tau_{750K} = 5.1090$ fs; for 1:3-*Pm*, $\tau_{300K} = 21.3235$ fs, $\tau_{500K} = 8.8032$ fs, $\tau_{750K} = 5.5403$ fs; for 3:1-*Pm*, $\tau_{300K} = 23.7341$ fs, $\tau_{500K} = 11.448$ fs, $\tau_{750K} = 5.0228$ fs.

1:2-*Pm* and 1:3-*Pm* both showed strong figure of merits in both their *n*- and *p*-doped regions reaching peaks of over 3.8 and 4.8 at 750 K in the *p*- and *n*-doping regions respectively. The 1:2-*Pm* showing strong mid-temperature *p*-type figure of merit, whilst the 1:3-*Pm* structure has strong low and high temperature figure of merits in line with 1:2-*Pm*, but shows little increase from 300 to 500 K. The 750 K *n*-type figures of merit of both 1:2-*Pm* and 1:3-*Pm* show similar levels to 2:2-*Pm* and 3:3-*Pmn*2₁.

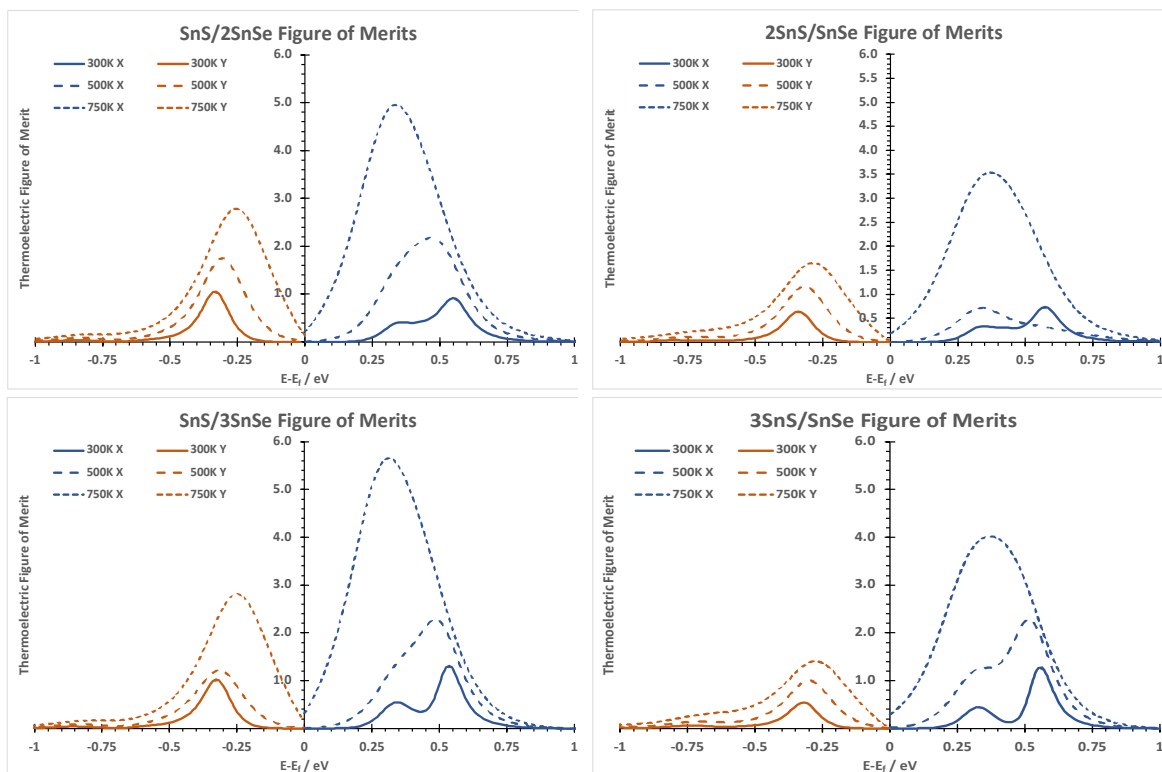


Figure 5.13: Figure of merits across chemical potentials for 300, 500 and 750 K
 Y-axis values are used for below the Fermi level and X-axis values are used for above

Across a Temperature Range

The full figure of merits are shown in Fig. 5.14 as a function of μ , with the axes with the largest below and above the Fermi level shown at each temperature, and the *Pnma*-SnS, *Pnma*-SnSe, 1:1-*Pmn*2₁, 2:2-*Pm* and 3:3-*Pmn*2₁ figure of merits show as dotted lines. These curves show the strong low temperature *p*-type figure of merits of the 1:2-*Pm* and 1:3-*Pm* structures, and good improvement over the *Pnma*-SnSe figure of merits with an increase of more than 50% at 300 K, whilst still showing similar levels to the *Pnma*-SnSe *n*-doping region figure of merit maximum. This *p*-type improvement over the base *Pnma*-SnSe is seen at 750 K as well, with the 2:2-*Pm* structure placing slightly higher at 500 K and the 1:3-*Pm* structure seeing little improvement from 300 to 500 K.

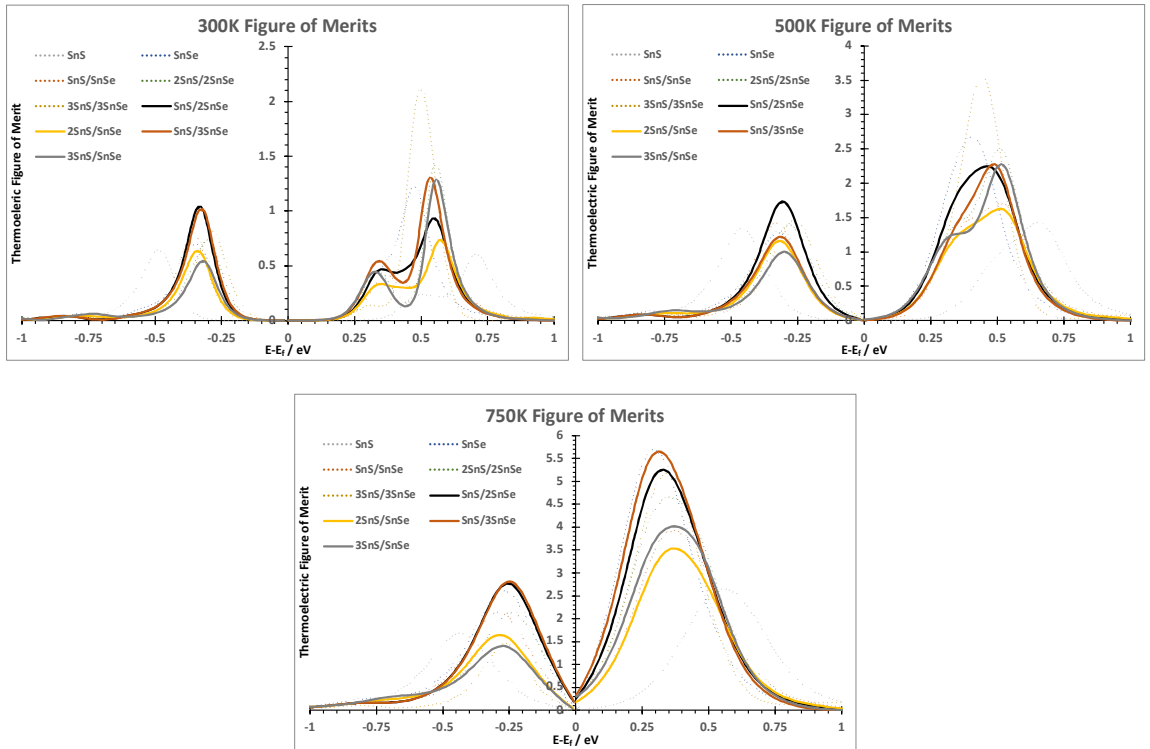


Figure 5.14: Full figure of merits of the asymmetrically layered materials at 300 K (upper left), 500 K (upper right) and 750 K (lower middle)

The figure of merits of the asymmetric layering structures are shown below using the average values of the 300, 500 and 750 K figures of merit, shown against μ . This highlights the strong p -type and n -type figure of merits shown by the 1:2- Pm and 1:3- Pm structures across the temperature range with the 1:2- Pm p -type figure of merits reaching highest peaks of all structures in this work. It should also be noted that the 1:3- Pm structure is less effective in the low temperature range than the full range due to its minimal improvement from 300 to 500 K.

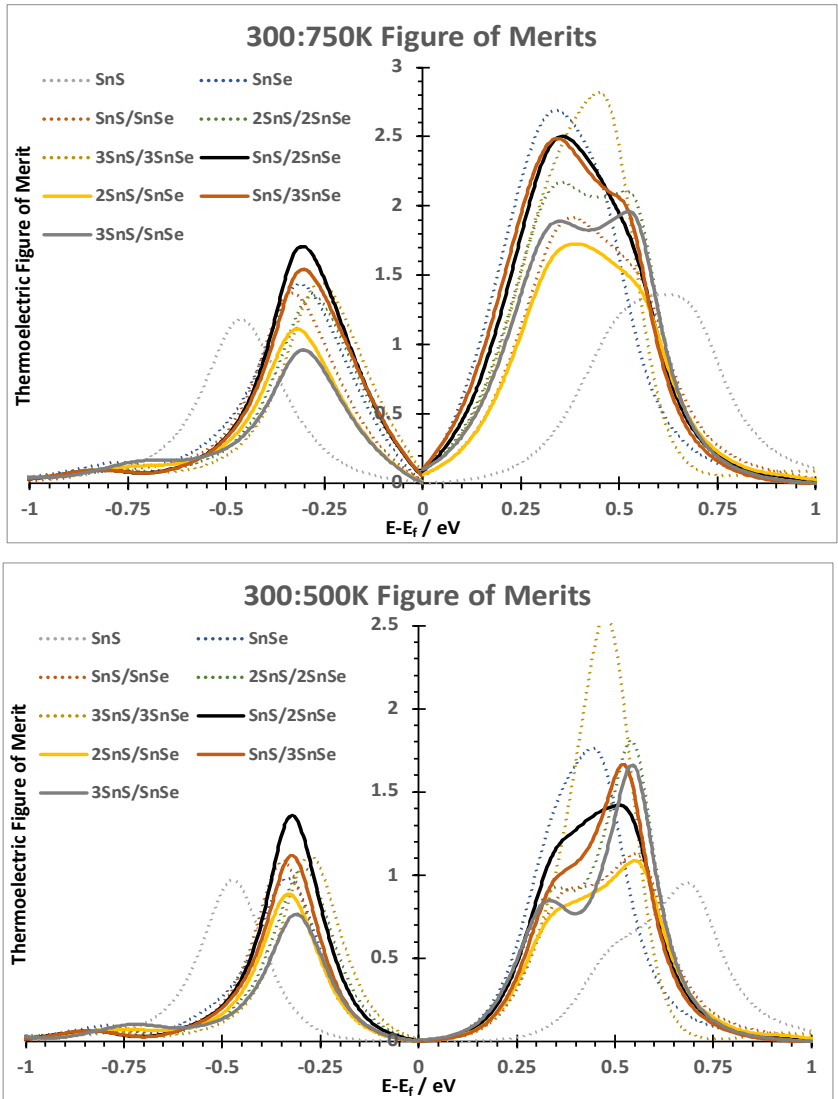


Figure 5.15: The averaged figure of merits of 300, 500 and 750 K and 300 and 500 K

The peaks of this data, as well as all previous figure of merit peaks are presented in Tables 5.2, 5.3 and 5.4. In these tables, the highest figure of merits in a given column are indicated in bold, representing the most effective thermoelectric structure at the given temperature(s) and doping region.

	300K		500K		750K	
	<i>n</i> -type	<i>p</i> -type	<i>n</i> -type	<i>p</i> -type	<i>n</i> -type	<i>p</i> -type
SnS	0.604	0.641	1.423	1.333	2.644	1.678
SnSe	1.212	0.696	2.667	1.285	5.686	2.602
<i>Cmcm</i>	1.136	0.688	2.229	1.607	2.852	2.213
1:1	0.742	0.788	1.701	1.417	3.925	2.135
2:2	1.430	0.736	2.487	1.384	4.649	2.128
3:3	2.106	0.817	3.558	1.458	5.192	2.319
1:2	0.918	1.054	2.172	1.747	4.954	2.786
2:1	0.737	0.639	1.627	1.163	3.537	1.651
1:3	1.302	1.046	2.249	1.246	5.525	2.858
3:1	1.290	0.547	2.278	1.003	4.018	1.405

Table 5.2: Figure of merit maxima at the given temperatures

	300K:500K		300K:750K		500K:750K	
	<i>n</i> -type	<i>p</i> -type	<i>n</i> -type	<i>p</i> -type	<i>n</i> -type	<i>p</i> -type
SnS	0.95	0.97	1.36	1.18	1.93	1.49
SnSe	1.76	0.98	2.69	1.44	3.80	1.87
<i>Cmcm</i>	1.63	1.13	1.98	1.47	2.51	1.89
1:1	1.13	1.08	1.91	1.37	2.67	1.73
2:2	1.81	1.05	2.17	1.35	3.05	1.72
3:3	2.56	1.12	2.82	1.45	3.90	1.83
1:2	1.39	1.37	2.35	1.72	3.32	2.18
2:1	1.09	0.89	1.73	1.11	2.43	1.39
1:3	1.65	1.14	2.43	1.57	3.38	1.94
3:1	1.67	0.77	1.96	0.96	2.72	1.19

Table 5.3: Figure of merit maxima at fixed chemical potentials across the temperature ranges.

	300K:500K		300K:750K		500K:750K	
	<i>n</i> -type	<i>p</i> -type	<i>n</i> -type	<i>p</i> -type	<i>n</i> -type	<i>p</i> -type
SnS	1.013	0.987	1.557	1.218	2.034	1.506
SnSe	1.940	0.990	3.189	1.527	4.177	1.943
<i>Cmcm</i>	1.682	1.148	2.072	1.503	2.540	1.910
1:1	1.221	1.102	2.123	1.446	2.813	1.776
2:2	1.959	1.060	2.855	1.416	3.568	1.756
3:3	2.832	1.137	3.619	1.531	4.375	1.888
1:2	1.545	1.400	2.681	1.862	3.563	2.267
2:1	1.182	0.901	1.967	1.151	2.582	1.407
1:3	1.775	1.146	3.025	1.716	3.887	2.052
3:1	1.784	0.775	2.529	0.985	3.148	1.204

Table 5.4: Maximal averaged figure of merits of the given temperature range, with optimal μ values for each individual temperature.

From these tables it can be seen that the interlayering of *Pnma*-SnS and *Pnma*-SnSe can greatly improve the figure of merits of the material. The figure of merits are improved by this layering in all but the pure 750 K case, where the 1:3-*Pm* peak figure of merit is only 0.16 below the *Pnma*-SnSe. The structures showing the clearest benefit from this layering scheme are the 3:3-*Pmn2₁* and the 1:2-*Pm*, where the 3:3-*Pmn2₁* outperforms all others with the largest *n*-type maxima in the 300K:500K, 500K:750K and 300K:750K cases, and the 1:2-*Pm* structure outperforms all others with the largest *p*-type maxima in the 300K:500K, 500K:750K and 300K:750K cases.

5.2 - Summary

5.2.1 - Lattice Thermal Conductivities

The lattice thermal conductivity reduction was less effective in the cross-layer direction for the asymmetric layering species than for the 2:2-*Pm* and 3:3-*Pmn2₁* structures, with the lowest lattice thermal conductivity values corresponding to 1:3-*Pm* with 0.201 W/m/K, whereas the 3:3-*Pm* structure reaches values of 0.1371 W/m/K. This is due to the lower intrinsic and extrinsic benefits brought about by single layers, and so less scattering phonons and the less significant phonon softening. However, all structures showed decreases in lattice thermal conductivities when compared to the *Pnma* base materials, indicating again the strength of this interlayering, particularly in disrupting long-range phonon modes. For the 1:2-*Pm* and 1:3-*Pm* structures the intralayer lattice thermal conductivity was further reduced from the 2:2-*Pm* and brought closer to the 3:3-*Pmn2₁*, indicating that the strain induced within the layers bringing the structure to a more *Cmcm*-like orientation was sufficient enough to reduce the b/c axis heat transport through phonon mode softening.

5.2.2 - Electronic Suitability

The power factors of the asymmetric layering structures showed good values in the *n*-doping region, but the main benefit was found in the *p*-doping regions of the 1:2-*Pm* and 1:3-*Pm* structures, where the power factors were raised to over 3.6 mW/m/K², above the *Pnma*-SnSe peak 3.1 W/m/K². This improvement in power factor indicates that the tailoring of structural thickness for *p*- or *n*-doped application can be used to find the optimal mix of electronic suitability and heat transport interference which is different for the two doping regions.

5.2.3 - Figure of Merit

Whilst the figure of merits do not reach the peak values seen in 3:3-*Pmn2₁*, the strength of 1:2-*Pm* and 1:3-*Pm* in both *p*- and *n*-doping regions opens very interesting and valuable areas of further study, with potential application as a single material thermoelectric device where simple axial arrangement can differentiate the two thermoelectric device legs such that the *p*-type leg involves the transport along the layers, and the *n*-type leg involves transport across the layers, as shown in Fig. 5.16.

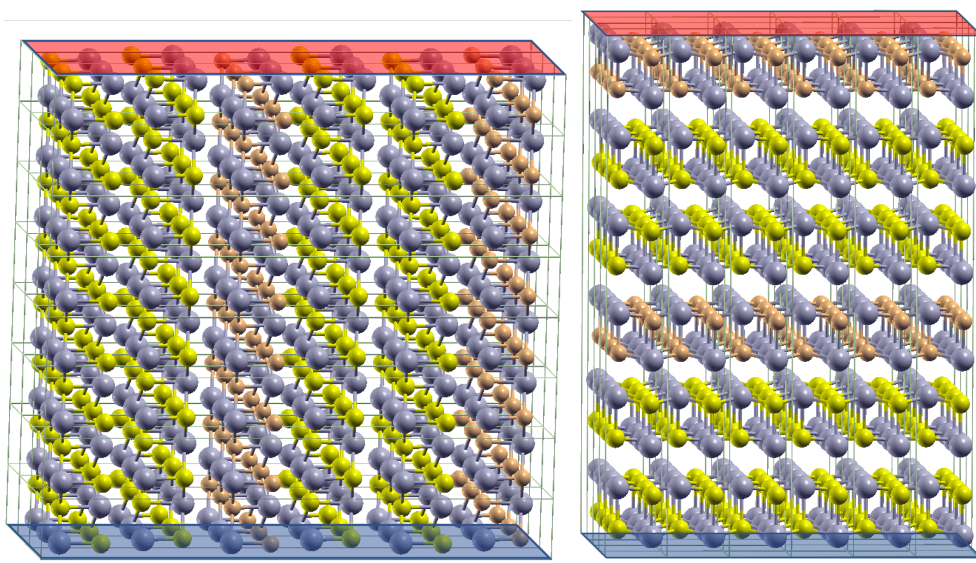


Figure 5.16: The potential arrangement of 1:2- Pm p - and n -type thermoelectric legs, with the hot and cold sides indicated.

As with the uniformly layered structures these materials show the most significant increases at lower temperature, where the lattice component dominates the thermal conductivity term. This is particularly important in the general application of a device using these materials as the low temperature will preferably be $\sim 300\text{K}$, and so efficiency at this temperature will affect the efficiency of the device.

Conclusion and Closing Remarks

SnS and SnSe have been shown through numerous experimental and computational works to hold strong potential in the field of thermoelectrics. Strong Seebeck coefficients, and very low lattice thermal conductivities allow for very high thermoelectric figure of merits. Alongside this, boundary conditions as a method of phonon scattering have often been used to reduce the lattice thermal conductivity of a material through the interruption of phonon pathways and reduction of heat transport closer to that of random walks.

With the 'sandwich layer' structures, new lattice boundaries are introduced to the system at the interfaces between the SnS and SnSe layers. With single layer alternations, these boundaries are seen to be ineffective at reducing the heat transport below the inherent heat resistivity of SnSe, but the introduction of thicker layering motifs showed a significant reduction in the lattice thermal conductivity to values far below those observed in previous explorations of SnS or SnSe, reaching a near 60% reduction along the layered a-axis in the 3:3- $Pmn2_1$ structure, as well as a ~20% reduction in the intralayer b-axis shown in the 2:2- Pm , 3:3- $Pmn2_1$, 1:2- Pm , and 1:3- Pm structures.

These reductions were evaluated through the phonon mean free paths and phonon lifetimes, and shown to be highly effective in reducing the heat transport of long-range phonon modes through the stacking direction of the material, also showing a minor improvement in the in-layer directions for phonon modes with mean free paths over 40 Å.

However, the lattice thermal conductivity was not only reduced by boundary scattering effects, with softening of phonon branches in the Γ -X direction leading to a lowering of the stacking direction phonon mode group velocities. This provided an intrinsic reduction of the lattice thermal conductivity to compliment the extrinsic scattering reduction, allowing the systems to target both the long and short range phonons.

A key component of thermoelectric material design is the trade-offs that are made when improving upon a specific feature of the thermoelectric figure of merit. Increases in electrical conductivity are met with increases in thermal conductivity, larger Seebeck coefficients are tied to a lower carrier concentration, and therefore a lower electrical conductivity, and whilst the lattice thermal conductivity is relatively free of these direct contradictory relationships, it is tied intrinsically to the structure of the material and therefore inevitably affects all other aspects of the thermoelectric properties. A key requirement is therefore applying a lattice

disruption that has minimal effect on the electrical properties, and the use of the very closely related SnS and SnSe structures aimed to achieve this. Whilst the power factors of all the suggested structures showed decreases in maxima compared to the component layers, the drop was not so significant as to remove the benefit brought. This was shown in the full figures of merit, where the strongest *n*-type figure of merits belong to the 3:3-*Pmn*2₁ structure, with a peak figure of merit of 2.82 across the temperature range 300 to 750 K and 2.56 across the range 300 to 500 K, as well as with all presented structures improving upon the SnS figure of merits. This highlights that this method can not only greatly improve the phonon disruption through intrinsic and extrinsic effects, but does so with the electrical properties largely retained.

The figure of merits were also shown to see the greatest improvement in the low temperature region, where application for thermoelectric devices is most useful and therefore sought after. The 300 K figure of merits were improved from 1.212 and 0.696 for *n*- and *p*-type SnSe to 2.106 and 0.817 for *n*- and *p*-type 3:3-*Pmn*2₁, and 0.918 and 1.054 for *n*- and *p*-type 1:2-*Pm*.

With the final device in mind the 1:2-*Pm* and 1:3-*Pm* structures showed very interesting properties. With full figure of merits that showing good improvement on SnS and good competition with the SnSe in the *n*-doping region, they also showed strong improvement in the *p*-doping region, reaching maxima far above the SnSe *p*-type maxima, with peak values of 1.72 and 1.57 for *p*-type 1:2-*Pm* and 1:3-*Pm* respectively, and 1.44 for *p*-type SnSe. This allows for the possibility of a single material thermoelectric device using *n*-doped cross-layer and *p*-doped intralayer orientations as the thermoelectric legs.

Limitations with Relaxation Time (Very Large zTs)

The figure of merits calculated for the *Pnma*-SnS and *Pnma*-SnSe structures showed maxima far greater than have been obtained through experimental methods. Whilst it is possible that the level of doping required to reach these values simply hasn't been reached, it would be naïve to assume that this the only possibility. The relaxation times were obtained by fitting to experimental data, and whilst showed to agree with previous calculations, they are reliant on data that is representative and precise, in particular with the steep nature of the Seebeck coefficient around the Fermi level. But with this caveat should be included a positive, lower relaxation times do not seem to adversely affect the degree to which these layered materials improve upon the figure of merit. With relaxation times of all structures

set to 1 fs the 2:2-*Pm*, 3:3-*Pmn*2₁, 1:3-*Pm* and 3:1-*Pm* schemes all show larger 300 K figure of merits than *Pnma*-SnSe, with 1:2-*Pm* showing a peak in line with SnSe.

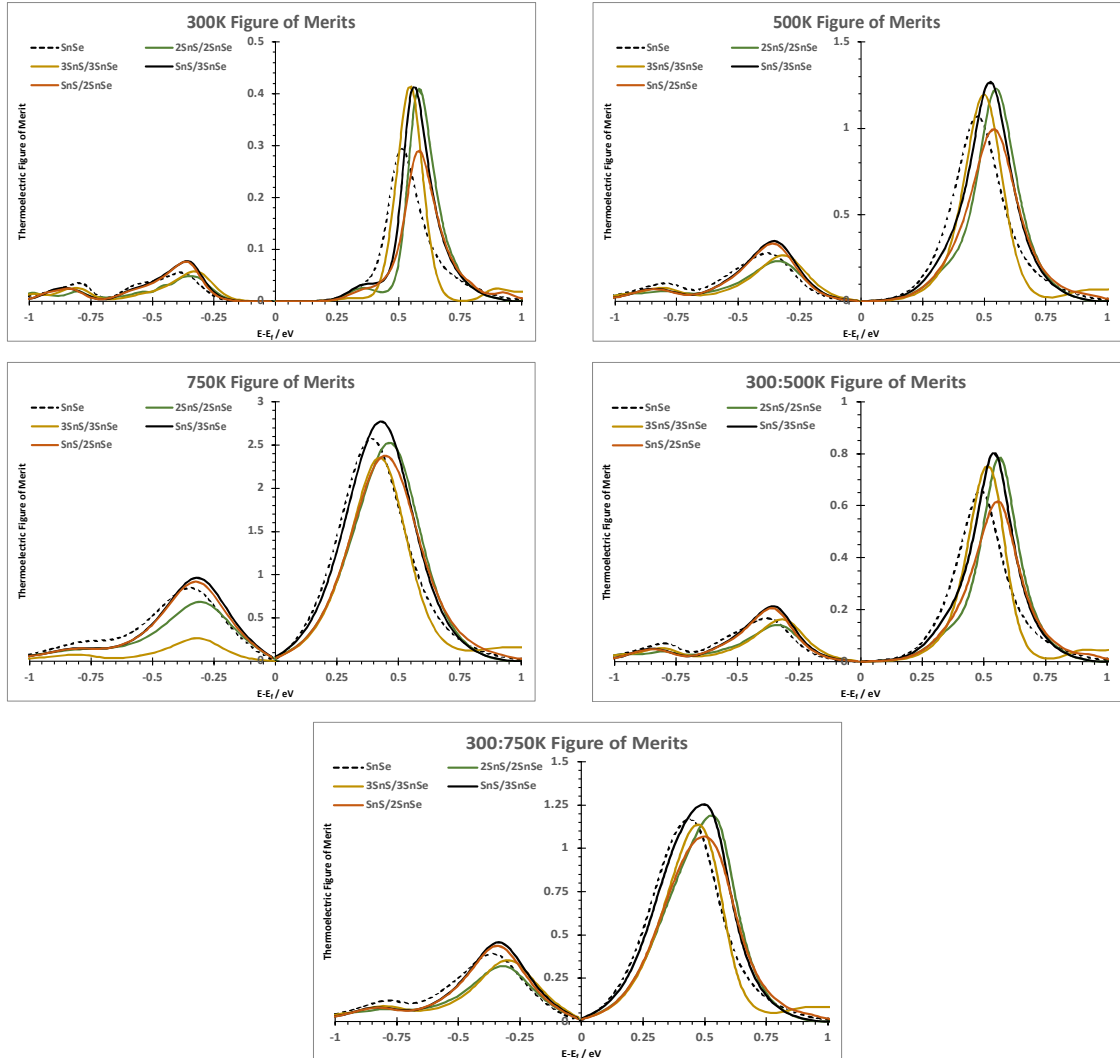


Figure X: The figure of merits using only relaxation times of 1fs for the *Pnma*-SnSe, 2:2-*Pm*, 3:3-*Pmn*2₁, 1:2-*Pm* and 1:3-*Pm* structures for the 300K, 500K, 750K temperatures and the 300:500K and 300K:750K temperature ranges

Outlook

Adjustment of the xTB Interatomic Potential

This work involved the use of a force scaling to account for the tighter bonding predicted by the xTB parameters than would be anticipated in the Phono3py force constant calculations. Whilst this is clearly effective, an alternative route would be the adjustment of the xTB parameters directly so as to clearly capture the properties without secondary adjustments. However previous attempts to parameterise these structures with DFTB have shown this to be difficult.

New Layering Schemes

With the success of the layering schemes shown, the question remains whether there are other systems of even greater figure of merits. The structures in this work were limited to 3 unit cells in length, with the 3:3- $Pmn2_1$ structure showing the most promise in lattice thermal conductivity reduction the expansion to 4 or more unit cell schemes could show further improvements. However, this aim is restricted by the computational cost associated with the increased atom counts, and whilst there is evidence to suggest that the supercell size can be reduced with still applicable results, there will inevitably be a limit.

Inclusion of Dichalcogenide Species

Another family of the tin chalcogenides are the tin dichalcogenides, SnX_2 . Like the monochalcogenides these exhibit a layered structuring and show strong Seebeck coefficients, indicating a potential suitability as thermoelectric materials. Therefore, the inclusion of layers of SnS_2 or SnSe_2 allow for a much larger number of combinations of layering schemes for exploration.

Large-Scale Material Engineering

While the focus of this work was closer to unit cell design but could be expanded to include the material on a much larger scale, with consideration for grain boundaries and lattice macrostructures the transport properties can be evaluated at a level much closer to its practical application. This would require different techniques than used in this work, however, as the computational cost for expanding the calculations to the number of atoms required far exceeds the capabilities of QE or xTB, but could provide greater insight into the interactions of the layering across a much larger system and their implications on the transport properties.

Supplementary Data

List of Publications

J. Rundle, S. Leoni, "Layered Tin Chalcogenides: Lattice Thermal Conductivity Benchmarks and Thermoelectric Figure of Merit", *manuscript submitted*

J. Rundle, S. Leoni, "Ultralow Lattice Thermal Conductivity in $(\text{SnS})_x(\text{SnSe})_y$ Heterostructures", *manuscript in preparation*

Relaxation Time Approximation (RTA) vs. Full Linearised Boltzmann Transport Equations (LBTE)

Pnma-SnS (at cutoff=15, sample mesh = 5x13x13)

		a	b	c
300 K	RTA	0.7353	1.7731	1.5444
	LBTE	0.7407	1.8971	1.7015
500 K	RTA	0.4412	1.0621	0.9254
	LBTE	0.4443	1.1357	1.0188
800 K	RTA	0.2757	0.6635	0.5781
	LBTE	0.2777	0.7093	0.6363

Table A.1: Lattice thermal conductivity values, in $\text{Wm}^{-1}\text{K}^{-1}$, of *Pnma-SnS* calculated with the Relaxation Time Approximation (RTA) and the direct solution to the Linearised Boltzmann Transport Equation (LBTE). Given at three temperature values and across the three primary axes.

1:1-Pmn2₁ (no cutoff [full calculation], sample mesh = 5x13x13)

		a	b	c
300 K	RTA	0.3466	0.9102	0.7630
	LBTE	0.3283	0.9393	0.7892
500 K	RTA	0.2078	0.5455	0.4576
	LBTE	0.1968	0.5629	0.4731
750 K	RTA	0.1385	0.3635	0.3050
	LBTE	0.1312	0.3751	0.3153

Table A.2: Lattice thermal conductivity values, in $\text{Wm}^{-1}\text{K}^{-1}$, of *1:1-Pmn2₁* calculated with RTA and LBTE. Given at three temperature values and across the three primary axes.

Cutoff-Pair Distance

A cutoff-pair distance was used for the 2:2-*Pm*, 3:3-*Pmn*2₁, 1:2-*Pm*, 2:1-*Pm*, 1:3-*Pm* and 3:1-*Pm* systems to further reduce the computational load. As shown in Fig. A.1, the lattice thermal conductivity of both *Pnma*-SnS and *Pnma*-SnSe stabilised at low cutoffs with little to no change at above these values. Fig. A.2 shows the convergence of the uniformly layered materials, whilst Fig. A.3 shows the convergence of the asymmetrically layered materials. The 100% mark is set to the full number of calculations determined by Phono3py to be required with no cutoff-pair distance.

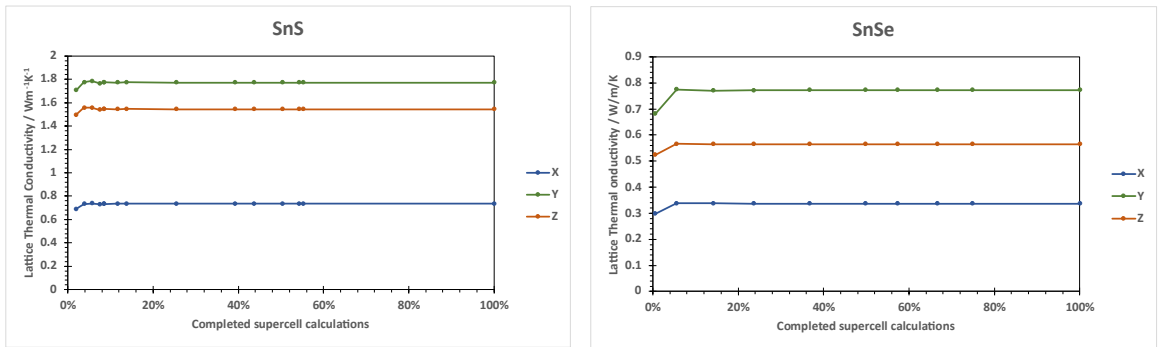


Figure A.1: The lattice thermal conductivities of *Pnma*-SnS (left) and *Pnma*-SnSe (right) at increasing cutoff-pair distances are shown.

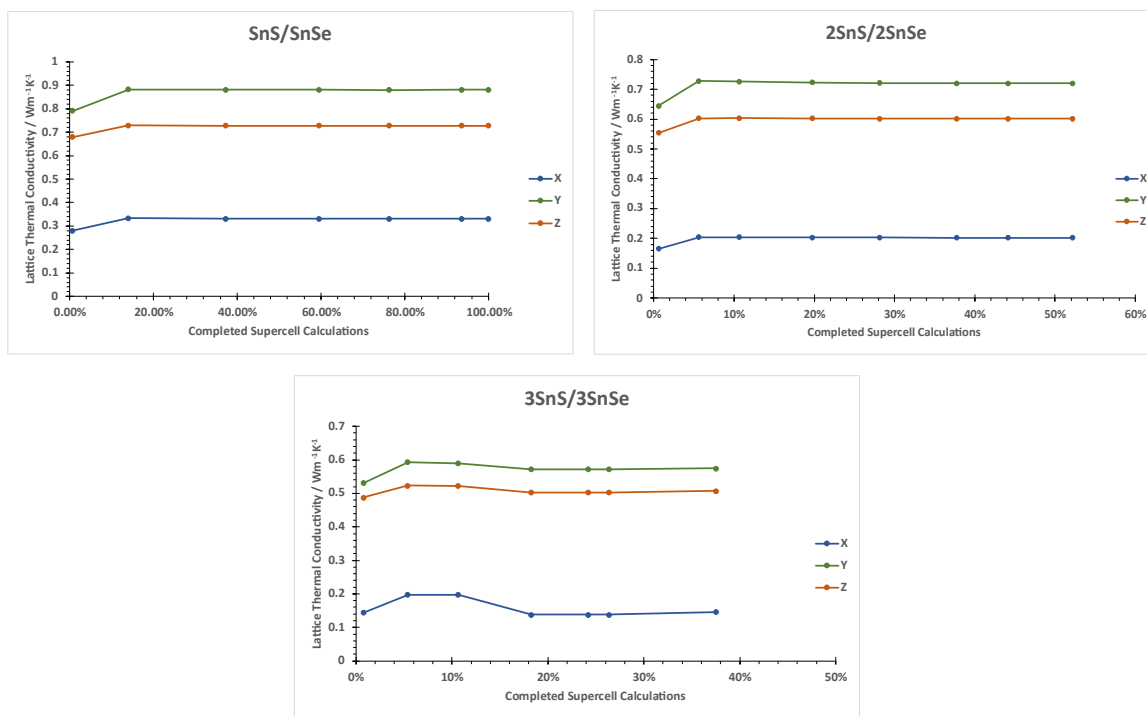


Figure A.2: The lattice thermal conductivity's dependence on cutoff-pair distance for 1:1- $Pmn2_1$ (upper left), 2:2- Pm (upper right) and 3:3- $Pmn2_1$ (lower middle)

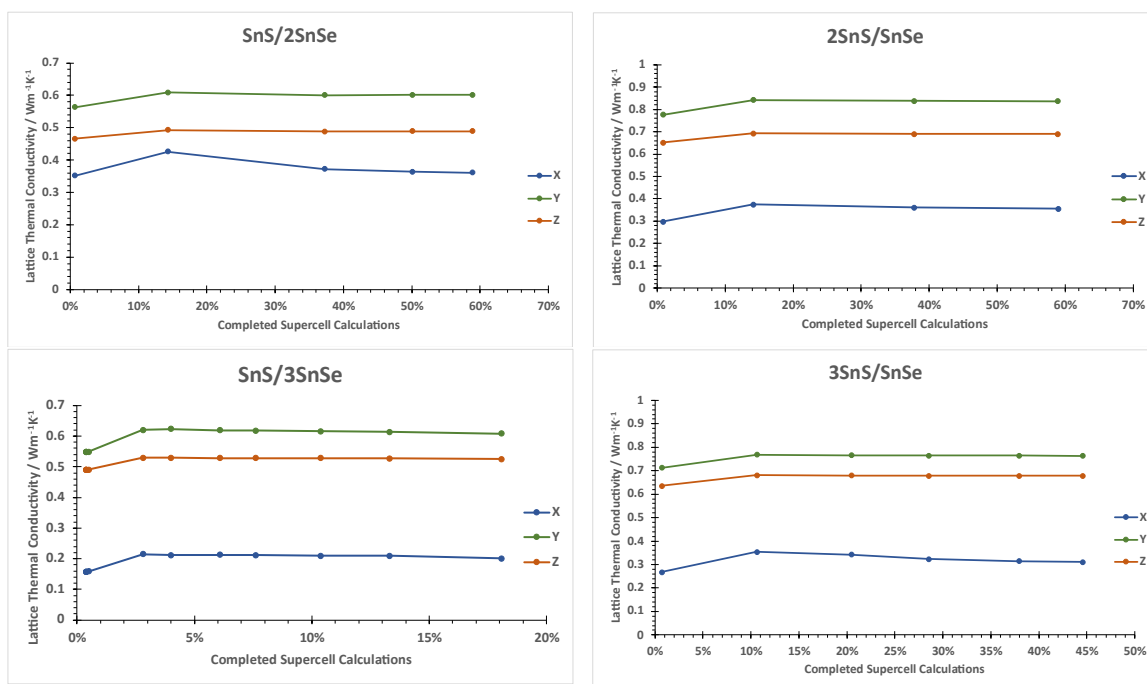


Figure A.3: Lattice thermal conductivity dependence on cutoff-pair distance for the 1:2- Pm (upper right), 2:1- Pm (upper left), 1:3- Pm (lower left) and 3:1- Pm (lower right) structures

Supercell Sizes

The lattice thermal conductivities were calculated on varying supercell sizes for the structures shown in this work, and are given below in the form:

fc3-size/fc2-size K_x K_y K_z

	Supercell Size	a	b	c
SnS	3x3x3/4x8x8	0.7687	1.8093	1.5908
	2x2x2/3x3x3(1)	0.6651	1.6135	1.4996
	2x2x2/3x3x3(2)	0.8794	2.1490	1.9948
	1x1x1/2x2x2	0.8258	1.6094	1.7439
1:1	3x3x3/4x8x8	0.3466	0.9102	0.7630
	2x2x2/3x3x3	0.3336	0.9590	0.8796
2:2	2x3x3/3x6x6	0.2145	0.7281	0.6047
	2x3x3/2x8x8	0.2133	0.7024	0.5961
	1x2x2/2x4x4	0.1785	0.7010	0.5972
1:2	1x3x3/2x4x4	0.2433	0.6257	0.5336
	1x2x2/2x3x3	0.2604	0.6287	0.5850
	1x1x1/2x2x2	0.2539	0.4907	0.6783
3:1	2x3x3/3x6x6	0.2366	0.8618	0.7199
	1x1x1/2x2x2	0.1943	0.5605	0.6313

Table A.3: Lattice thermal conductivity values, in $\text{Wm}^{-1}\text{K}^{-1}$, of various structures calculated with differing supercell sizes.

SnS 2x2x2/3x3x3 (1) and (2) refer to separate sampling mesh sizes, 11x30x29 and 12x35x34 respectively, where smooth convergence was not fully achieved.

Sampling Mesh

The choice of the phono3py sampling mesh was converged with respect to lattice thermal conductivity, with the convergence curves shown below.

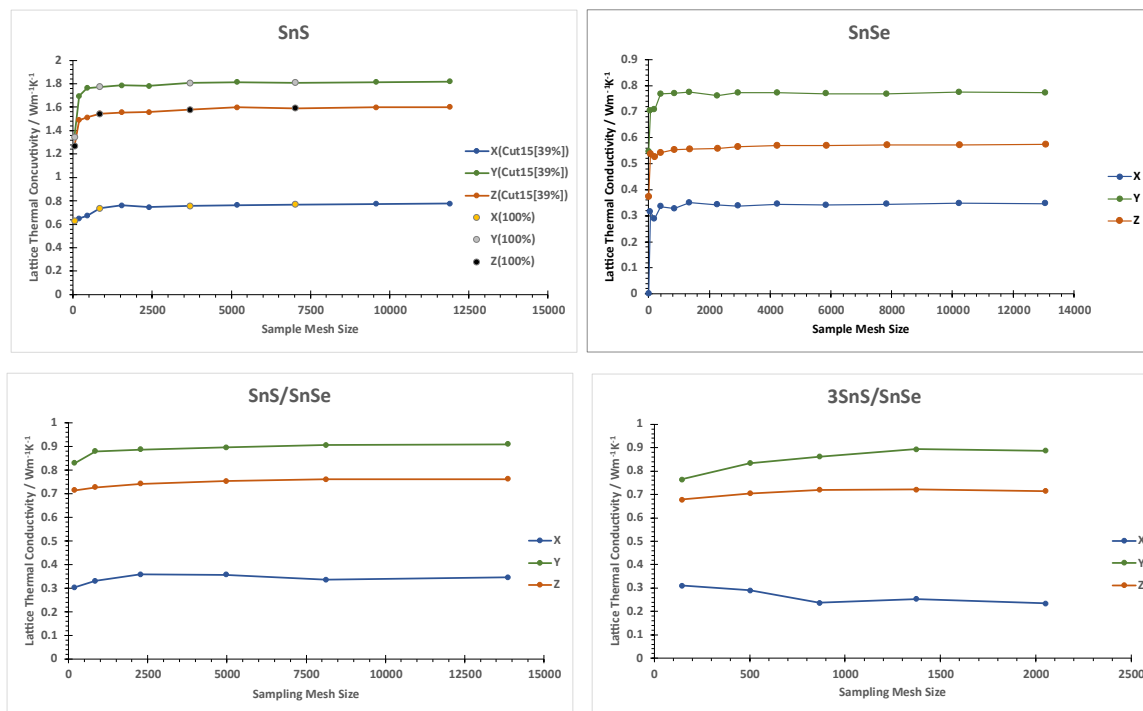


Figure A.4: Lattice thermal conductivity convergence, shown as the total number of grid points generated by the automatic sampling mesh, for $Pnma$ -SnS (above-left), $Pnma$ -SnSe (above-right), 1:1- $Pmn2_1$ (below-left), and 3:1- Pm (below-right). $Pnma$ -SnS is shown both with a cutoff-pair distance of 15 Å and with no cutoff, highlighting that the shape of the convergence is not dependent on the cutoff value.

Some structures did not converge easily with the automatic sampling mesh. These are therefore shown with their convergences relative to the increase in either the x or the y and z direction sampling points. The sampling meshes used in each graph are given, where n is the number of points changed along the graph's x-axis, i.e. the first point in the 3:3- $Pmn2_1$ n-20-20 figure corresponds to a 4x20x20 sampling mesh, and the first point in the 5-n-n corresponds to a 5x6x6 sampling mesh.

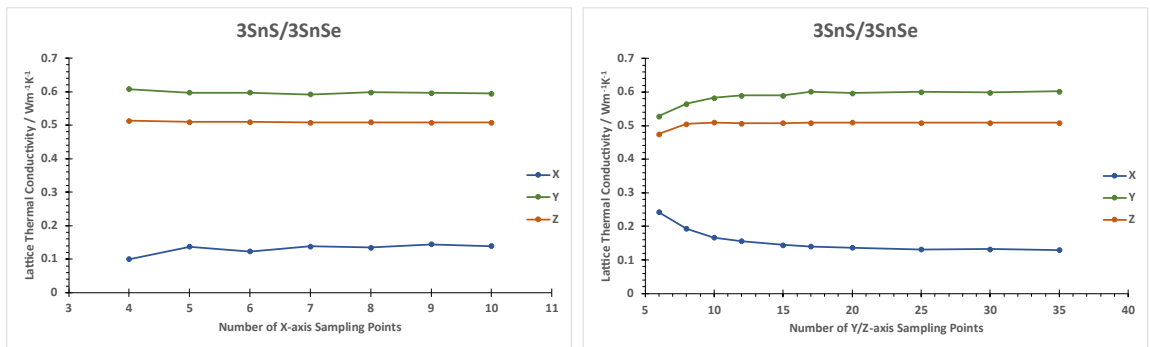


Figure A.5: 3:3- $Pmn2_1$, shown using an n-20-20 sampling mesh (left) and a 5-n-n sampling mesh (right)

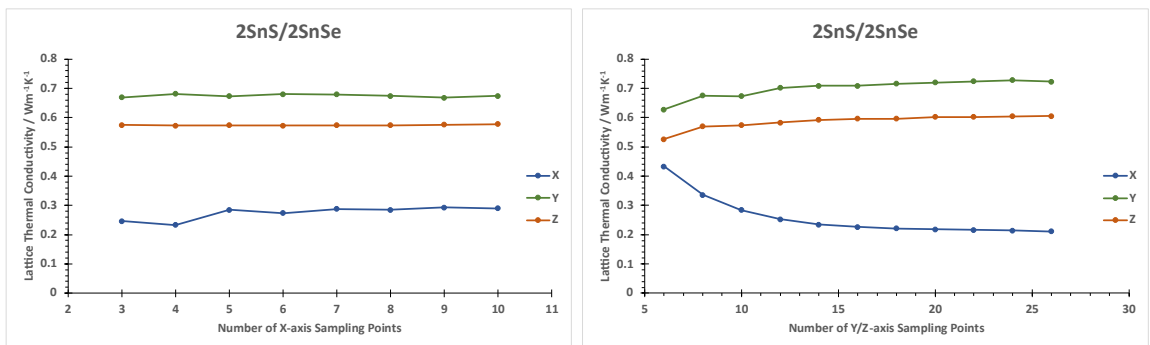


Figure A.6: 2:2- Pm , shown using an n-10-10 sampling mesh (left) and a 5-n-n sampling mesh (right)

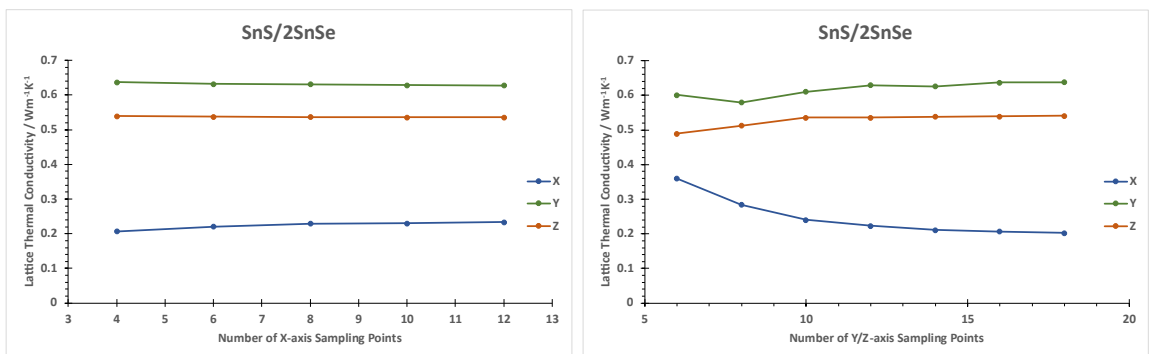


Figure A.7: 1:2- Pm , shown using an n-16-16 sampling mesh (left), and a 4-n-n sampling mesh (right)

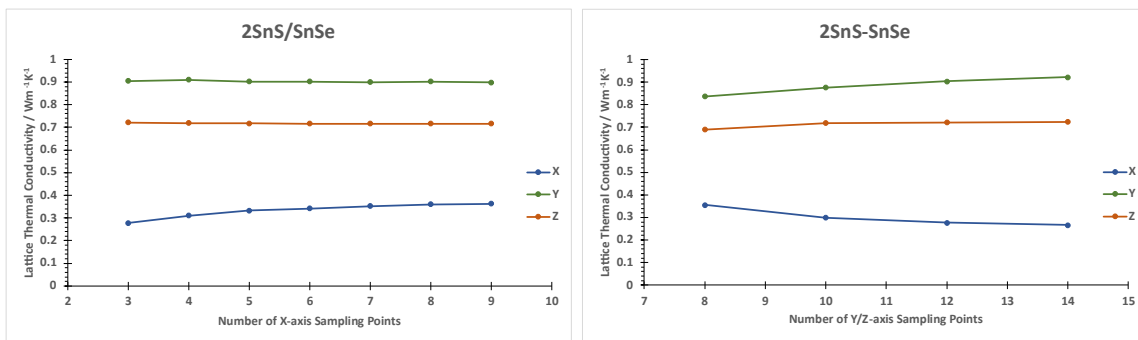


Figure A.8: 2:1-*Pm*, show using an n-12-12 sampling mesh (left), and a 3-n-n sampling mesh (right)

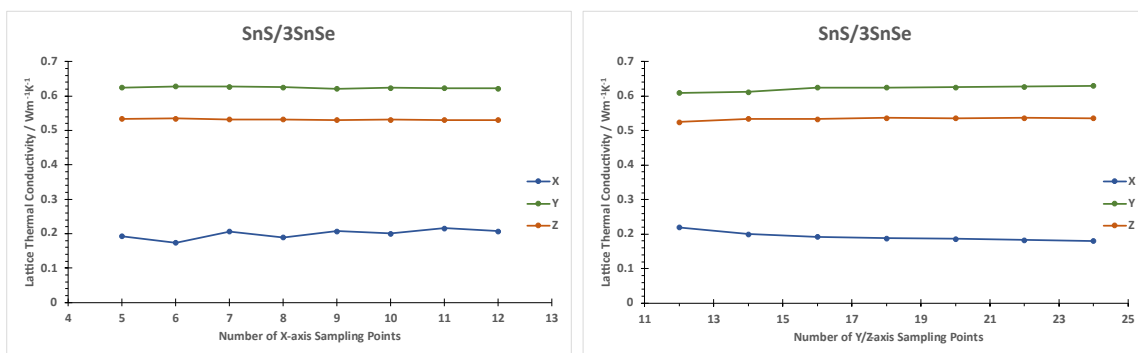


Figure A.9: 1:3-*Pm*, shown using an n-16-16 sampling mesh (left), and a 5-n-n sampling mesh (right)